CUKUROVA UNIVERSITY
INSTITUTE OF NATURAL AND APPLIED SCIENCES

PhD THESIS

Physicochemical Characterization and Determination of Luminescence Properties of Silicon-Rich Tridymite Mineral

Sümeyra BALCI

Physics Department

July, 2023

CUKUROVA UNIVERSITY
INSTITUTE OF NATURAL AND APPLIED SCIENCES

PhD THESIS APPROVAL

Physicochemical Characterization and Determination of Luminescence Properties of Silicon-Rich Tridymite Mineral

---

Sümeyra BALCI

Physics Department

This Doctorate Thesis was evaluated by the following Jury Members on 06/07/2023 and was approved by unanimity / majority of votes.

Jury : Prof. Dr. Mustafa TOPAKSU (Supervisor) ……………………

: Prof. Dr. Cebrail GÜMÜŞ ……………………

: Prof. Dr. Ramazan BİLGİN ……………………

: Prof. Dr. Hüseyin TOKTAMIŞ ……………………

: Prof. Dr. Emir Vural KAFADAR ……………………

This Thesis was written in the Department of Physics Institute of Natural and Applied Sciences.

Thesis Number:

Prof. Dr. Sadık DİNÇER
Director
Institute of Natural and Applied Sciences

This work was supported by the Çukurova University Scientific Research Fund.
Project ID: FDK-2016-6178

DEDICATION

…dedicated to the people who seriously make an effort to be a part of my life.

CONTENTS

CUKUROVA UNIVERSITY
INSTITUTE OF NATURAL AND APPLIED SCIENCES

PhD THESIS

Physicochemical Characterization and Determination of Luminescence Properties of Silicon-Rich Tridymite Mineral

Sümeyra BALCI

Supervisors: Prof. Dr. Mustafa TOPAKSU
: Dr. Virgilio CORRECHER

Department of Physic

ABSTRACT

Tridymite is a unique mineral found in volcanic environments that possesses the ability to withstand high temperatures. Its industrial usage remains limited, indicating untapped potential. Understanding its properties could unlock innovative applications, particularly in ceramics. Tridymite exhibits prospective usability in dosimetry applications, while the existing literature concerning tridymite in the realm of mineralogy remains highly restricted. Tridymite is also found on Mars and provides insights into the formation of celestial bodies. Advancements in this field would enhance our understanding of tridymite both on Earth and beyond. In this study, tridymite sample from Lanzarote, Canary Islands, Spain were analyzed by using Thermal X-ray Diffraction (T-XRD), Environmental Scanning Electron Microscopy with Energy Dispersive Spectroscopy (ESEM-EDS), Electron Probe Microanalysis (EPMA), Raman spectroscopy, Nuclear Magnetic Resonance (NMR) spectroscopy, Electron Paramagnetic Resonance (EPR) spectroscopy, and luminescence techniques (Cathodoluminescence (CL), Photoluminescence (PL), Thermoluminescence (TL)). These techniques collectively enhance our understanding of tridymite mineral by revealing its crystalline structure, elemental composition, chemical composition, molecular dynamics, electronic structure, and luminescent properties.

Keywords: Tridymite, Spectroscopy, Luminescence

ÇUKUROVA ÜNİVERSİTESİ
FEN BİLİMLERİ ENSTİTÜSÜ

DOKTORA TEZİ

Silikonca Zengin Tridimit Mineralinin Fizikokimyasal Karakterizasyonu ve Lüminesans Özelliklerinin Belirlenmesi

---

Sümeyra BALCI

Danışmanlar : Prof. Dr. Mustafa TOPAKSU
: Dr. Virgilio CORRECHER

Fizik Anabilim Dalı

ÖZ

Tridimit, yüksek sıcaklıklara dayanma yeteneğine sahip volkanik ortamlarda bulunan eşsiz bir mineraldir. Endüstriyel kullanımı, kullanılmayan potansiyelin göstergesi olarak sınırlı kalmaktadır. Özelliklerini anlamak, bilhassa seramikte yenilikçi uygulamaların kilidini açabilir. Tridimit, dozimetri uygulamalarında ileriye dönük kullanılabilirlik sergilerken, mineraloji alanında tridimite ilişkin mevcut literatür oldukça sınırlı kalmaktadır. Tridimit ayrıca Mars'ta da bulunur ve gök cisimlerinin oluşumu hakkında fikir verir. Bu alandaki gelişmeler, hem Dünya'da hem de ötesinde tridimit anlayışımızı geliştirecektir. Bu çalışmada, İspanya'nın Kanarya Adaları'ndaki Lanzarote adasından elde edilen tridymit örneği, Termal X-ışını Kırınımı (T-XRD), Çevresel Taramalı Elektron Mikroskopu ve Enerji Dağılımlı Spektroskopi (ESEM-EDS), Elektron Prob Mikroanalizi (EPMA), Raman spektroskopisi, Nükleer Manyetik Rezonans (NMR) spektroskopisi, Elektron Paramanyetik Rezonans (EPR) spektroskopisi ve luminesans teknikleri (Katodoluminesans (CL), Fotolüminesans (PL), Termolüminesans (TL)) kullanılarak analiz edilmiştir. Bu teknikler, tridymit mineralinin kristal yapı, elementel bileşimi, kimyasal bileşimi, moleküler dinamikleri, elektronik yapısı ve luminesans özelliklerini ortaya koyarak tridymit minerali hakkındaki anlayışımızı artırmaktadır.

Anahtar Kelimeler: Tridimit, Spektroskopi, Lüminesans

EXTENDED SUMMARY

Tridymite, as a distinctive mineral discovered in volcanic settings, exhibits exceptional heat resistance capabilities. Although its current industrial utilization is constrained, the limited scope suggests a wealth of untapped possibilities awaiting exploration. A comprehensive understanding of its properties could hold the key to unlocking pioneering applications, particularly in the realm of ceramics. This mineral could have the potential to revolutionize various sectors, including the development of advanced nanotechnological devices, advancements in roof construction techniques, the production of efficient thermal furnaces, and the enhancement of surface coatings for rockets, among other innovative implementations. Moreover, tridymite exhibit promising potential in the field of dosimetry, where it can be utilized for radiation measurement and monitoring.

Due to the scarcity of literature in the field of mineralogy regarding tridymite, further research is necessary to fully comprehend its characteristics and potential applications. Tridymite's unique properties make it a fascinating subject for exploration in the scientific community. Its ability to withstand high temperatures and its association with volcanic environments make it a valuable mineral for various fields of science and industry.

In the field of dosimetry, tridymite's potential usage is particularly notable. Dosimetry involves the measurement and assessment of radiation doses, and tridymite's properties may contribute to the development of more accurate and efficient dosimetry techniques. By understanding how tridymite interacts with radiation, scientists and researchers can harness its properties to improve radiation detection, protection, and dosage measurement in various fields, including medical applications, nuclear energy, and environmental monitoring.

The exploration of tridymite's properties, along with its potential applications in dosimetry and ceramics, could open up new avenues for scientific research and technological advancements. As our understanding of tridymite continues to grow, so too will our ability to harness its unique attributes for the benefit of numerous industries and applications.

Furthermore, the presence of tridymite on Mars offers valuable insights into the planet's volcanic activity, geological evolution, and past environmental conditions. Tridymite's formation at high temperatures and pressures suggests a hot and active environment on Mars in the past, potentially conducive to the existence of liquid water and the development of life. Furthermore, studying tridymite samples provides information about the intensity of volcanic activity, the origins of volcanoes, and the planet's internal structure. These findings could contribute to our understanding of Mars' geological dynamics, climate changes, and potential for habitability. Ultimately, unraveling the properties and origins of tridymite advances our knowledge of Mars and opens avenues for further exploration of its evolution, the presence of water, and potential life forms.

The Timanfaya eruption holds the record for being the longest-lasting eruption recorded in the Canary Islands, Spain, occurring between 1730 and 1736. Intensive research has revealed the high silica content of the erupted lavas during this event. Studies examining the mineralogical and chemical composition of Timanfaya lavas have reported significant silica enrichment. The silica-rich nature of these lavas has attracted scientific interest and led to investigations of various minerals found within them. In this context, tridymite samples were obtained from molten silica-rich deposits from Lanzarote island, one of the Canary Islands in Spain. In this thesis, the tridymite samples were analyzed using various spectroscopic and luminescence techniques.

T-XRD analysis, which stands for Thermal X-ray Diffraction analysis, has emerged as a powerful tool in the study of the crystallographic structure of tridymite. This non-destructive technique utilizes X-ray diffraction to probe the atomic arrangement within the crystal lattice of tridymite under controlled temperature conditions. This technique has allowed to determine the presence of defects, quantify phase abundance, and examine the temperature and pressure effects on tridymite stability. Furthermore, the effects of temperature on tridymite stability can be thoroughly examined using this analysis. This enables researchers to study how the crystallographic structure changes with increasing or decreasing temperatures. By establishing the relationship between temperature and the crystal structure, scientists can gain insights into the material's thermal behavior and potential applications in high-temperature environments. In conclusion, it provides critical information about the crystallographic structure of tridymite under controlled thermal conditions. These findings have broad implications in various scientific and industrial fields, making T-XRD an indispensable tool for studying crystalline materials.

ESEM-EDS has provided a unique imaging capability, allowing the examination of surface features at high magnification and elemental analysis. In this way, particles and surface defects were investigated by examining the microstructure. Composition analysis using EDS has provided valuable information about the distribution and concentration of elements within tridymite, aiding in the identification of impurities and potential geological relationships. In the geological context, it has offered new perspectives on the relationships between tridymite and other minerals. By analyzing the elemental composition of tridymite along with surrounding minerals, researchers can gain insights into the geological processes that have influenced its formation and distribution. This information is essential in understanding the geological history of tridymite-rich regions and can provide valuable clues about past environmental conditions and volcanic activities.

EPMA has complemented EDS analysis by providing quantitative elemental analysis at higher spatial resolution. This technique has enabled the examination of major, minor, and trace elements within tridymite samples. EPMA has facilitated precise chemical composition determination, elucidating compositional changes within tridymite and providing valuable insights into formation processes and geological significance.

Raman spectroscopy has been a powerful tool for studying the vibrational properties and phase identification of tridymite. By analyzing the scattered light's Raman spectrum, the characteristic vibrational modes of tridymite can be identified. This technique has not only confirmed the mineral's identity but also provided information about crystal properties, polymorphic transitions, and structural disorders.

NMR spectroscopy has been used to investigate the molecular structure and dynamics of tridymite. By analyzing the interactions of atomic nuclei with an external magnetic field, NMR has provided valuable information about chemical bonding, coordination, and local environments within the mineral. This technique has shed light on the mobility of atoms and their interactions with neighboring species, revealing the behavior of tridymite under different conditions.

EPR has been focused on studying the unpaired electrons and paramagnetic defects in tridymite. By subjecting the material to a magnetic field and measuring the absorption or emission of electromagnetic radiation, EPR spectroscopy has provided information about the electronic structure, magnetic properties, and defects within tridymite. This technique has been particularly useful for identifying and characterizing the defects.

Luminescence techniques such as CL, PL, and TL have provided valuable information about the luminescent properties and electronic structure of tridymite. CL analysis involves the excitation of tridymite with high-energy electrons and reveals emission patterns, providing information about luminescent centers, defect-related emissions, optical properties, and energy band structure. PL measurements have been used to examine emission spectra and energy band structures through optical excitation of the mineral. TL analysis, on the other hand, measures the release of stored energy as light when tridymite is subjected to controlled heating, providing insights into trapped and released charge carriers and the mineral's thermal history.

The integration of these advanced analytical techniques has let to a comprehensive understanding of the tridymite mineral. These knowledge has contributed to the fundamental understanding of tridymite's structural, chemical, and optical properties, paving the way for advancements in fields such as geology, mineralogy, dosimetry, materials science, and planetary science. Also, the information obtained from these techniques has been crucial for deciphering the formation processes, environmental conditions, and geological significance of tridymite, ultimately enhancing our understanding of Earth's geology and extraterrestrial environments. The presence of tridymite on Mars has offered insights into the planet's past volcanic activity and environmental conditions, which can help infer its climate, the presence of water, and potential habitability. Understanding the properties and behavior of tridymite serves as a valuable clue for exploring the possibility of life on Mars. Detailed analysis of tridymite samples can provide additional information about Mars' geological evolution, volcanic processes, and sources, deepening our understanding of the planet's formation and the potential existence of diverse life forms.

ACKNOWLEDGEMENTS

I would like to thank my PhD supervisor, Dr. Mustafa Topaksu and my PhD Co-Supervisor, Dr. Virgilio Correcher, for supporting me during the thesis period. Dr. Topaksu is one of the most positive, knowledgeable, helpful and understanding academician I know. Dr. Topaksu has been supportive and given me not only the freedom to pursue this work without objection but also scientific advice and knowledge. I am also very grateful to Dr. Correcher for accepting me as a Visiting Research Scholar at Energy, Environmental and Technological Research Center (CIEMAT), in Madrid, Spain, during three months enable me to work with him at TL laboratory in CIEMAT. I learn a lot from him, and he is always very supportive and energy booster mentor for me.

I am very gratefull to Dr. Javier Garcia-Guinea for accepting me as an observer for the measurements of Cathodoluminescence, Esem-EDS, Raman, Photomuminescence experiments at The National Museum of Natural Sciences (NMNS) of the Spanish National Research Council (CSIC), in Madrid, Spain. I would like to thank to Dr. Ülkü Sayın for accepting me as an observer for the measuremets of EPR experiments at Advanced Technology Research and Application Center (ILTEK), in Konya, Turkey. I would like to thank to Cecillia Boronat for her nice friendship during my stay at CIEMAT.

I also have to thank the members of my PhD committee, Dr. Cebrail Gümüş, Dr. Ramazan Bilgin, Dr. Hüseyin Toktamış, and Dr. Emir Vural Kafadar for their helpful career advice and suggestions in general.

A good working group is of great importance during an academic life. I was lucky to be a part of the group under the direction of Dr. Topaksu with the group members who are Dr. Ziyafer Gizem Portakal Uçar, Dr. Sibel Akça Özalp, Dr. Tamer Doğan, Dr. Mehmet Yüksel, Dr. Kenan Bulcar, and Aya Barad. Gizem and Sibel are always excellent, honest and helpfull co-workers and heartfelt friends for me. I would like to thank Dr. Gönül Akça for her excellent roommateness and heartfelt friendship. I would like to extend my heartfelt gratitude to my dearest friend Tuğba Topal for her unwavering support and encouragement.

I would like to thank the Research Funding Projects Unit in Çukurova University for their support to this PhD thesis under the project no. FDK-2016-6178.

Finally yet importantly, I would like to express my deepest thanks to my large family, especially my mother, for their endless love and support. I am forever grateful to my toddler Mercan for helping me get through the times when I had to steal moments to play with her.

LIST OF TABLES

LIST OF FIGURES

SYMBOLS AND ABBREVIATIONS

A	: Amper
ADPs	: Atomic displacement parameters
Al	: Aluminum
b	: Kinetic order
B	: Boron
BSE	: Backscattered electron
C	: Celcius
Ca	: Calcium
ca	: Circa
CIEMAT	: Environmental and technological research center
CGCD	: Computerized glow curve deconvolution
CL	: Cathodoluminescence
Cl	: Chlorine
Co	: Cobalt
Cr	: Chromium
CSIC	: Spanish national research council
CTD	: Continuous trap distribution
Cu	: Cupper
d	: Distance
DR	: Dose response
DTD	: Discrete trap distribution
E_a	: Activation energy level
EDS	: Energy dispersive spectroscopy
EDX	: Energy dispersive x-ray spectroscopy
ENDOR	: Electron-nuclear double resonance
EPMA	: Electron probe microanalysis
EPR	: Electron paramagnetic resonance
ESEM	: Environmental scanning electron microscopy
ESR	: Electron spin resonance
eV	: Electron volt
F	: Fluorine
Fe	: Iron
FOK	: First order kinetics
FOM	: Figure of merit
FWHM	: Full witdh at half maximum

GCF : Glow curve fading

Ge : Germanium

GOK : General order kinetics

Gy : Grey

h : Concentration of trapped holes

H : Hydrogen

Hg : Mercury

HP : Heating rate

HR : Hexagonal packing

ILTEK : Advanced technology research and application center

I_m : Maximum intensity value or peak intensity

IR : Infrared

IR : Initial rise

k : Boltzmann constant

K : Potassium

LHP : Lower-temperature hexagonal phase

Li : Lithium

lro : Long range order

MAS : Magic spinning angle

MC : Monoclinic crystal structure

Mg : Magnesium

Mn : Manganese

Mo : Molybdenum

MSL : Mars science laboratory

MX : Metal-halide crystal structure

n : Concentration of trapped electrons

n : Diffraction order

Na : Sodium

n_c : Concentration of free electrons in conduction band

Ni : Nickel

NMNS : The national museum of natural sciences

NMR : Nuclear magnetic resonance

n_o : Concentration of trapped electrons at t = 0

NTL : Natural TL

O : Oxygen

OC : Orthorombic-centered cubic packing

ODCs : O-deficient centers

OP : Orthorombic-centered packing
OS : Orthorombic-sided packing
OSL : Optically stimulated luminescence
p : Escape probability of an electron from trap
PDF : Pair distribution function
PF : Peak fit
PL : Photoluminescence
PMT : Photomultiplier tube
PO : Pseudo-orthorombic crystal structure
ppm : Parts per million
r : regression coefficient
RT : Room temperature
PTTL : Photo-transferred TL
RU : Reusability
s : Vibration frequency of electrons or frequency factor
sec : Seconds
SEM : Scanning electron microscopy
Si : Silicon
Sr : Strontium
T : Absolute temperature in Kelvin
t : Time in seconds
Ti : Titanium
TL : Thermoluminescence
TLD : Thermoluminescence dosimeter
T_m : Peak temperature
TMS : Tetramethylsilane
T_o : Temperature at t = 0
T-XRD : Thermal X-ray diffraction
Uiso : Isotropic atomic displacement parameters
UV : Ultraviolet
V : Volt
VHR : Various heating rates
W : Watt
Wt : Weight
XRD : X-ray diffraction
Y : Yttrium
Zn : Zinc

Å : Angstrom

λ : Wavelength

θ : The glancing angle

1. INTRODUCTION

1.1. Goal, Approach and Limitations

Tridymite represents a geological enigma with ongoing discussions surrounding the authenticity of its pure crystalline silica form. This mineral is exclusively found in volcanic settings in its natural state and its primary benefit lies in its capacity to withstand high temperatures. Despite the prevalence of volcanic environments worldwide since the formation of Earth's crust, where magmatic rocks, including tridymite, constitute a significant portion of the lithosphere's quartz content (Götze, 2009), the industrial utilization of tridymite remains infrequent, suggesting untapped potential and limited understanding of its practical uses.

To evaluate the effectiveness of tridymite raw materials, particularly in the ceramic industry, it becomes crucial to delve into the limitations of processing techniques and actively explore new deposits. By gaining comprehensive knowledge of tridymite properties, researchers and industries can unlock its full potential and discover innovative ways to harness its unique characteristics.

Tridymite is a mineral that holds significant potential in the field of dosimetry. Dosimetry is a scientific method used to measure and analyze the effects of radiation on biological systems. Tridymite's application in this area could aid in detecting and evaluating high-dose ionizing radiation exposure. This mineral is a naturally occurring polymorph under high temperature and pressure conditions, and certain changes in its crystal structure make it radiation-sensitive. Tridymite-based dosimeters could have potential applications in medicine, industry, and radiation safety, providing a reliable and effective method for accurately determining radiation doses. However, further studies and research on the use of tridymite as a dosimeter are necessary to fully understand its potential and optimize its performance.

Furthermore, the study of tridymite extends beyond Earth's boundaries. The field of Martian mineralogy is rapidly advancing, and with ongoing investigations on Mars, researchers are actively studying the presence and properties of tridymite on the Red Planet. This parallel progress in Martian mineralogy opens up new avenues for scientific discoveries and insights into the formation and geological processes of celestial bodies. Continuous advancements in this field are expected to reveal further connections and enhance our understanding of tridymite, both on Earth and beyond (Yen, et al., 2020; Payré, et al., 2022).

1.2. Theoretical Concept

1.2.1. Chemical and Spectral Characterization

Thermal X-Ray Diffraction (XRD)

In order to analyze the crystal structures of the materials, X-rays are diffracted by crystals, and their wavelengths are in the same range as the lattice parameters of the crystal in the substance.

An XRD equipment, which consists of an X-ray tube, an X-ray detector, and a sample holder, is used to perform these investigations. In an XRD device, electrons produced by heating the filament (such as tungsten) contained in the X-ray tube are accelerated under high voltage and impinged on a target material (such as Cu, Co, and Mo). These high-energy electrons excite the electrons of the target material, causing them to be excited to an upper orbital. The target material emits characteristic X-rays when the electrons return to their original positions. Using various filters, these X-rays are made monochromatic and routed to the sample surface in the holder. The rays that reach the surface of the sample are scattered in numerous directions. As a result of this scattering, the rays attempt to destroy each other through destructive interference, or they can be recognized by the detector by constructive interference by increasing the wave intensities. This interference, measured by detectors, is described as X-ray diffraction. Diffraction is caused by the path difference between rays reflected from two successive crystal planes, which is an exact multiple of the wavelength. This condition is known as Bragg's law.

$\{2\, d \sin\theta = n\lambda\}$

Consequently, XRD patterns of the sample are obtained by scanning the surface of the sample during an XRD measurement and determining the angles at which the Bragg condition is satisfied and the diffraction intensities at these angles. These XRD patterns are unique to each material and provide information on a variety of subjects, including

- the crystal's atomic arrangement,
- unit cell type and size,
- lattice parameters,
- extent of crystallization.

Thermal-XRD (T-XRD), on the other hand, enables the same experiments to be performed with precise temperature control to investigate the structural and thermal properties of materials as they undergo temperature variations. Heating processes are known to cause material expansion, lattice structure modulation, that is, structural or chemical changes that result in the formation of various defects. This method proves particularly valuable for studying

- phase transitions,
- thermal stability,
- alterations in crystal structures across a range of temperatures.

Furthermore, the T-XRD results can be used for a comparative analysis of the changes in grain size, which are most accurately assessed through peak broadening using the Debye-Scherrer equation, and the variations in lattice parameters (which are not within the scope of this study but remain a key point to emphasize).

Environmental Scanning Electron Microscope - Energy Dispersive X-ray Spectroscopy

ESEM is significant in science and industry because it can be used to examine the majority of natural and synthetic materials in their natural or minimally altered state, in various phases of matter, or during phase transitions (Danilatos, 1988).

Basically, the scanning electron microscope (SEM) is a device that observes nanoscale detailed structures based on electron wave and particle interactions using a combination of optical and electronic systems. Electrons produced by heating the filament in the device's electron gun are accelerated at high voltage (under high vacuum). Electrons that have been accelerated are collected using concentrating electromagnetic lenses. Then the objective lens focuses it on the desired surface of the sample. Various kinds of signals are created because of physical interactions between electrons reaching the sample surface and atoms in the sample. The SEM image of the scanned material is obtained by detecting these signals with the detector. ESEM, on the other hand, is a device with a similar working principle to SEM, however it is designed in such a way that it does not require a high vacuum environment (Danilatos, 1988; Danilatos, 1990; Nedela, et al., 2018).

When an electron beam accelerated by a sufficiently high voltage is sent to the material's surface, it can detach the electrons in the inner orbital that are securely bound to the atomic nucleus, causing them to be excited and this excited electron leaves behind a hole. To fill this gap, an electron from a higher energy level descends to a lower energy level. In proportion to the energy difference between these two energy levels, a photon is emitted. This material-specific photon emitted is called characteristic X-rays. In other words, the components of the material emit X-rays at specific wavelengths. EDS (or EDX; Energy Dispersive X-ray Spectroscopy) analyses of the materials are possible due to the peaks obtained by detecting these emitted X-rays with the detectors. As a result, EDS analysis enables the determination of a material's composition.

Electron Probe Micro Analyzer

The primary purpose of X-ray diffraction is to perform qualitative and quantitative analyses of minerals, which is among its most common applications. However, the X-ray does have several drawbacks, the most notable of which are its limited sensitivity and the difficulty it has in identifying minerals with a low percentage of constituents. Additionally, although X-ray diffraction can be used to measure the comprehensive chemical composition of all of the minerals in the sample, the measurement of select minerals or minerals at a certain location requires the assistance of an electron probe in order to achieve a precise analysis and supply X-ray diffraction data. This is because the electron probe is able to determine the exact composition of the mineral being measured.

Electron probe micro analyzer, also known as EPMA, is a common instrument that is used to investigate the elements that are present on the surface of materials. EPMA has the ability to scan any part of a material's surface and promptly analyze its constituent components through the examination of X-rays that are created when electron beams strike the surface of minerals (He & Shi, 2014).

In the fields of geology, metallurgy, mineralogy, chemistry, and biology etc, electron microprobe technology is employed extensively for component analysis (Roman-Lopez, et al., 2014; Lee, et al., 2017; Smaha, et al., 2022).

In order for the samples to be usable for EPMA analysis, they must fulfill the following conditions:

- The size of the samples must be appropriate for the inner diameter of the instrument sample holder, and the samples should not be outside of the range of the inner diameter.
- It is required that the surface of the samples be in a polished state.
- It is important that the surface of the samples have high conductivity. Otherwise, insulating samples have to be coated with carbon film before it is tested.
- Keep samples away from sources of contamination, such as abrasives, hand-touching, and the analysis area.
- Prior to analysis, the sample must be marked at locations where an electron probe can easily detect it (He & Shi, 2014).

Raman Spectroscopy

Raman spectroscopy is a method for analyzing the vibrational and rotational modes of molecules. It provides information regarding a material's molecular composition, chemical bonds, and structural properties. The method is predicated on the inelastic scattering of monochromatic light, typically from a laser source, when it interacts with a sample. Raman spectroscopy is based on the Raman effect, which occurs when particles interact with the molecules of a sample. Most of photons scatter elastically (Rayleigh scattering), but a small fraction scatter inelastically, resulting in energy shifts that correspond to vibrational or rotational transitions in the sample molecules. The scattered light is collected and analyzed for frequency shifts from the incident light in Raman spectroscopy. The energy shifts correspond to the vibrational modes of the sample molecules, which provide information regarding their molecular structure, functional groups, and chemical composition. The energy difference between incident and scattered light is referred to as the Raman shift. It is measured in wavenumbers (cm^{-1}) and represents the sample's vibrational modes. Each unique vibrational mode generates a distinctive Raman peak, enabling the identification and characterization of the sample's molecular components. Raman spectroscopy has numerous applications in various fields, including chemistry, materials science, pharmaceuticals, geology, biology, and forensic science. It is used for

- qualitative and quantitative analysis,
- identifying unknown substances,
- monitoring chemical reactions,
- imaging,
- non-destructive sample characterization (Si, et al., 2022; Görelik & Pyatyshev, 2019).

Nuclear Magnetic Resonance

NMR is a technique used to study the magnetic properties of atomic nuclei. It is based on the principle that atomic nuclei with an odd number of protons or neutrons possess a property referred to as spin, which results in a magnetic moment. Such nuclei absorb and emit energy at distinct frequencies when a sample containing them is exposed to a particular radiofrequency radiation and placed in a strong magnetic field. NMR provides information about

- the chemical structure,
- molecular dynamics,
- and interactions within a sample.

It can reveal details about molecular bonding, molecular conformation, chemical shifts, coupling constants, relaxation times, and diffusion coefficients (Wasson & Salinas, 1980; Shkrob, et al., 2000). NMR is widely used in chemistry, biochemistry, medicine, materials science, and other fields. It is used for structural elucidation of organic and inorganic compounds, determination of molecular concentrations, investigation of protein and nucleic acid structures, drug discovery, metabolic profiling, and more (Keating, et al., 2008; Letertre, et al., 2021).

Electron Paramagnetic Resonance

EPR, also known as Electron Spin Resonance (ESR), is a spectroscopic technique used to study the magnetic properties of materials that contain unpaired electrons. It provides information about the electron spins in a sample and their interaction with an external magnetic field. In fact, EPR is based on the same fundamental principle as NMR but focuses on the spins of unpaired electrons instead of atomic nuclei. Unpaired electrons possess a property called spin, which gives rise to a magnetic moment. When a sample containing such electrons is placed in a magnetic field and subjected to electromagnetic radiation, the electrons absorb and emit energy at specific frequencies (Götze & Plötze, 1997; McQueen, et al., 2001). EPR experiments involve the manipulation of various parameters, such as the magnetic field strength, microwave frequency, and temperature, to obtain specific information about the sample. Furthermore, EPR provides information about the electronic structure, spin states, and magnetic interactions within a sample. It can yield details about g-factors (a measure of electron magnetic moment), hyperfine coupling constants (describing interactions with nearby nuclei), linewidths, relaxation times, and spin dynamics. Different EPR techniques, such as continuous-wave EPR, pulsed EPR, or electron-nuclear double resonance (ENDOR), can provide different types of information (Feher, 1959; Nilges, et al., 2009).

Overall, EPR is a powerful technique for understanding the magnetic properties of materials and has contributed to numerous discoveries and advancements in various scientific disciplines. In other words, EPR is particularly valuable in investigating paramagnetic species and their behavior in different environments. In this manner, it is widely used in various fields, including chemistry, physics, materials science, biology, and medicine. It is applied in the study of

- free radicals,
- transition metal complexes,
- spin traps,
- semiconductors,
- magnetic materials,
- enzyme kinetics, and more (Meier, et al., 2007).

1.2.2. Luminescence

When an insulator or semiconductor crystal material is exposed to any radiation type or an energy source, it may absorb some of the energy it has received. The electrons in the outermost orbit of the atom or molecules in the material can reach a higher energy level with the energy they absorbed. The electron, in the unstable state (conduction band), stays in this upper energy level for a very short time (~10^{-8} s) and then returns to its former stable state (valance band). It loses this absorbed energy as photon (light) emission, which has an energy equal to the difference between the two energy levels. This type of light emission phenomenon is generally called luminescence (McKeever, 1985). In fact, there are two relevant energy bands in an ‘ideal’ insulator: a completely filled valance band and an empty conduction band. A forbidden gap separates these two energy bands, as shown in Figure 1.1. When transitions are allowed between the valance and conduction bands, they produce free electrons in the conduction band and free holes in the valance band.

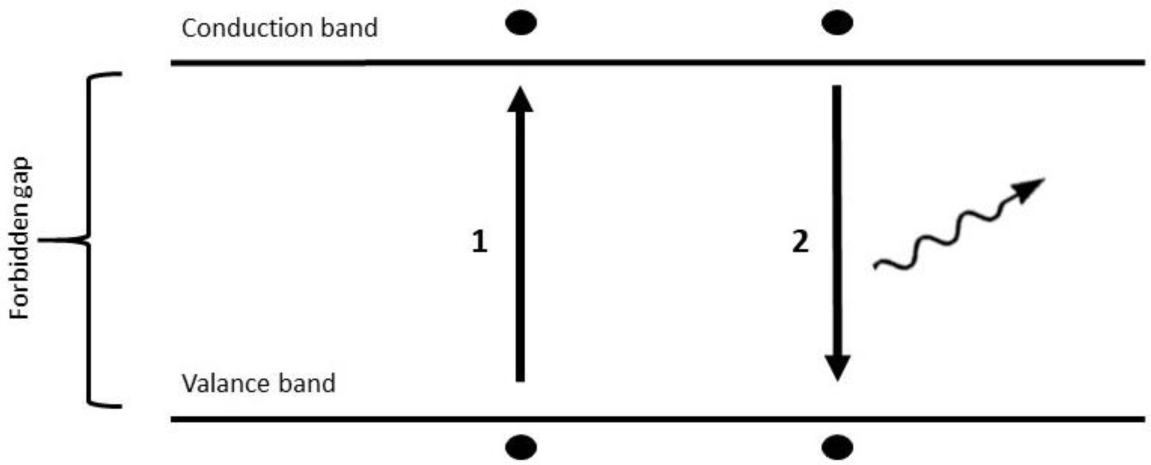

Figure 1.1. Basic energy band diagram.

Depending on the source of excitation, luminescence types can be listed as: bioluminescence, cathodoluminescence, chemiluminescence, electroluminescence, ion beam luminescence, optically stimulated luminescence, piezoluminescence, photoluminescence, radioluminescence, sololuminescence, thermoluminescence, triboluminescence etc… (O'Hara, et al., 2005; Garcia-Guinea, et al., 2007; Forbes, 2018). More information about the types of luminescence studied in scope of thesis is given in the following headings.

Cathodoluminescence

CL is an optical and electromagnetic phenomenon that involves the excitation of a luminescent material, such as phosphorus, by electrons. This excitation results in the emission of photons, which may fall within the visible, UV, IR spectrum of wavelengths. It is caused by the high energy of an electron beam, which promotes electrons from the valence band to the conduction band, leaving a hole (Figure 1.2) (Marshall, 1988; Pagel, et al., 2000).

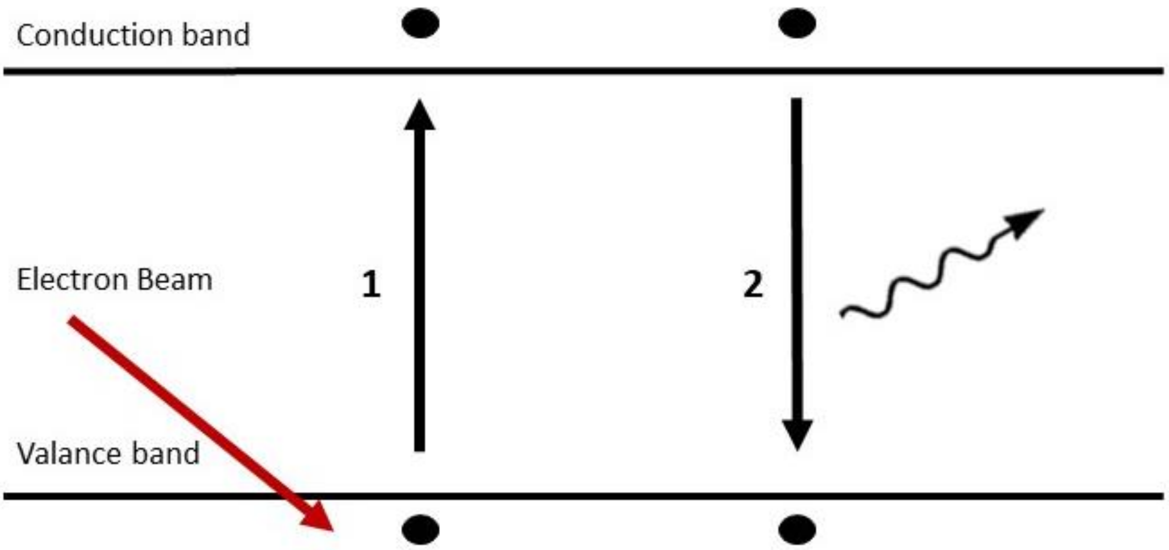

Figure 1.2. Diagram of the electron's excitation state during CL.

CL can be categorized into two distinct groups, namely those that result from intrinsic and extrinsic luminescent centers:

- The luminescence centers that are intrinsic to a material can be classified into two types. The first one is attributed to the direct recombination of electron-hole pairs, which is commonly referred to as band-to-band luminescence. The second type is caused by structural defects that are present in the specific structure of a high-purity crystal material. These defects can include lattice voids, radiation effects, and impurity atom effects.
- The forbidden energy gap region in a host material may contain extrinsic luminescence centers, which are comprised of point defects or clustered defects. These defects are caused by the presence of activator ions, which are impurity atoms with a specific mass or moles and concentration damping value. The most common extrinsic luminescence centers are activators (such as transition metal ions, rare earth ions) (Garlick & Gibson, 1948; Marshall, 1988).

The emission of CL provides valuable data regarding the location of wavebands, which holds significant relevance in determining the appropriate optical parameters for conducting TL measurements (Sarasola-Martin, et al., 2021).

CL is a sensitive technique that can detect impurities acting as point defects, typically associated with bands at wavelengths greater than 500 nm. Furthermore, CL can identify structural defects such as planar, Frenkel, and Schottky defects, dislocations, and vacancies, which are generally linked to higher energy emissions (Sarasola-Martin, et al., 2021).

Photoluminescence

PL refers to the emission of light from a material after it absorbs photons and undergoes a non-radiative transition to a lower energy state. This phenomenon is commonly observed in various materials, including semiconductors, organic molecules, and phosphors. The following is an analysis of the fundamental components of PL in general.

(i) Absorption: Photons from an external light source are absorbed by the material. The energy carried by the photons promotes electrons within the material from a lower energy level (ground state) to a higher energy level (excited state). The energy difference between the ground and excited states corresponds to the energy of the absorbed photons.

(ii) Excitation: Once the electrons are in the excited state, they are temporarily promoted to higher energy levels, typically within the conduction band of the semiconductors.

(iii) Relaxation: After excitation, the electrons in the higher energy levels lose energy through various non-radiative processes such as heat dissipation or interaction with other molecules in the material. These processes cause the electrons to transition to lower energy levels within the material.

(iv) Emission: The final step in PL occurs when the electrons transition from higher energy levels to lower energy levels, often the valence band or the ground state. During this transition, excess energy is released in the form of photons, resulting in the emission of light (Gilliland, 1997; Lee & Kim, 2004).

The classification of PL can be based on the length of the excited state, resulting in two primary types:

Fluorescence: In fluorescence, the emission of light occurs almost immediately after absorption. The excited state typically lasts for a short period, on the order of nanoseconds to microseconds. Fluorescent materials absorb photons of higher energy (shorter wavelengths) and emit photons of lower energy (longer wavelengths), often in the visible range.

Phosphorescence: Phosphorescence is similar to fluorescence but with a key distinction: the excited state persists for a longer duration, ranging from microseconds to hours or even longer. This delayed emission is due to the presence of "triplet states" in the material, which require a change in electron spin for relaxation. Phosphorescent materials are capable of absorbing and emitting light over a wider range of wavelengths, including visible, infrared, and even ultraviolet.

PL phenomena have numerous applications in various fields, including optoelectronics, display technologies, lighting, solar cells, sensors, biomedical imaging, and more (Van Sickle, et al., 2013; Piao, et al., 2013; Costa , et al., 2022).

Overall, PL is a fundamental process that plays a crucial role in various scientific and technological fields. It enables the generation of light in a controlled manner, opening up possibilities for numerous applications and advancing our understanding of materials. By studying the properties of emitted light, researchers can gain valuable insights into the electronic structure, energy transfer processes, and optical properties of materials.

Both PL and CL techniques offer complementary approaches to the study of luminescence in materials. While PL primarily utilizes external light sources to induce luminescence, CL leverages the interaction between electron beams and materials. These techniques enable researchers to explore the electronic structure, carrier dynamics, and luminescent behavior of materials, providing valuable insights for various scientific disciplines.

Thermoluminescence

TL enables to extract valuable insights into the thermal impact on the luminescent emission of insulating or semiconducting materials that have undergone prior irradiation. As the temperature rises, the likelihood of trapped electrons escaping their energy traps increases, resulting in the occurrence of downward transitions to lower energy levels through recombination with a hole, subsequently leading to photon emission. This phenomenon of light emission is commonly referred to as TL.

The TL two-step band theory is a model used to explain the TL phenomenon observed in certain materials. TL refers to the emission of light (luminescence) from a material when it is heated (thermo). In the two-step band theory (Figure 1.3), the process is described as follows:

(i) Absorption and trapping: When a material is exposed to ionizing radiation (such as X-rays or gamma rays), electrons in the valence band absorb the energy and get excited to the conduction band, leaving behind electron vacancies or "holes" in the valence band. Some of these excited electrons get trapped at defect or impurity sites within the material.

(ii) Heating and recombination: When the irradiated material is subsequently heated, the trapped electrons in the defect sites gain sufficient thermal energy to overcome the trapping energy levels and return to the conduction band. As the electrons recombine with the holes in the valence band, they release energy in the form of light (photons).

The emitted light during the heating process is measured and analyzed to obtain information about the radiation dose received by the material and the properties of the traps involved (McKeever, 1985; McKeever, et al., 1995; Furetta, 2003).

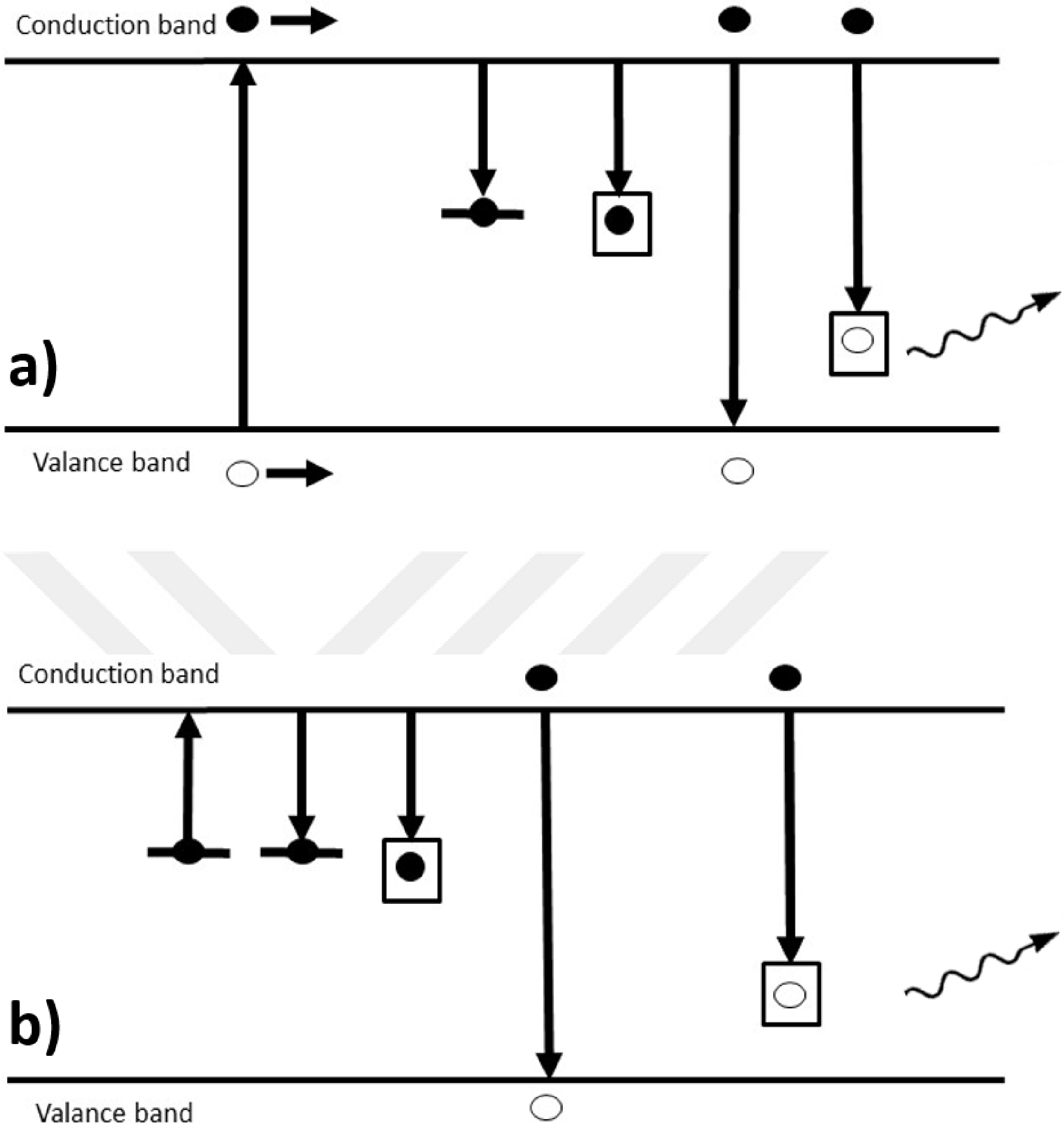

Figure 1.3. Two step TL band diagram: a) The process that occurs within the crystal structure through irradiation. b) The process that occurs within the crystal structure through heating.

If the sample is heated at a constant rate, electrons in the traps are emptied in order from shallow to deep and make a light emission. Each trap group has a different release temperature values. The emission increases or decreases as the temperature approaches or moves away from these values. The curve that shows these increases and decreases in emission as a function of the temperature is called the glow curve (Figure 1.4 (Balci-Yegen, et al., 2018)).

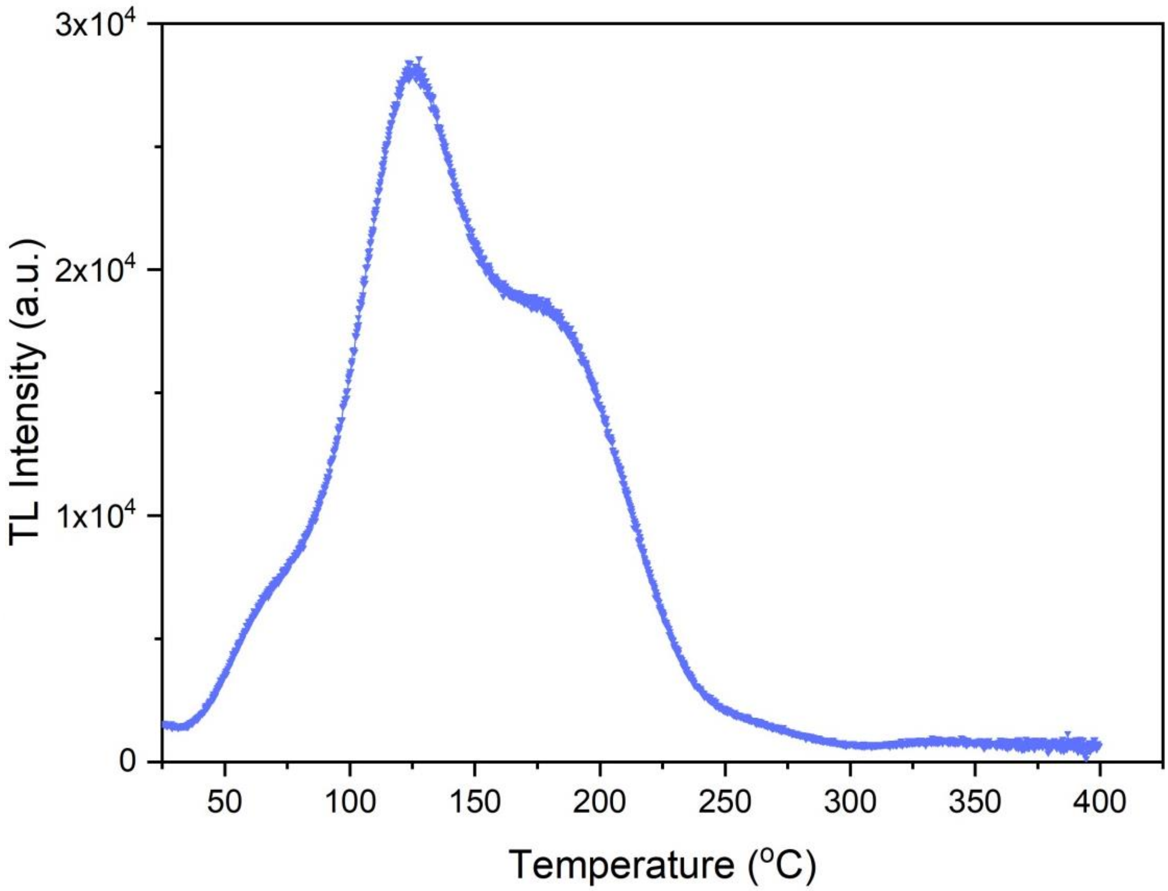

Figure 1.4. Glow curve of ZnB2O4:0.05Dy3+ Phosphor.

The radiation effect on the structural and point defects gives rise to glow curves where the TL intensity is usually proportional to the absorbed dose (Correcher, et al., 2003). Naturally occurred crystal defects in the lattice structure of the silica are responsible for electron traps. Electron-hole pairs that cause atoms, molecules or free radicals to gain mobility are caused by ionizing radiation applied to the material. Point defects are caused by different impurities and vacancies in the lattice structure of the material exposed to ionizing radiation, and these defects can change the optical properties of the material. In other words, the luminescence response of silica to radiation depends on the concentration and type of impurities and vacancies in the crystal lattice. Detailed information and discussions about these responses are in the relevant section as results of the experiments.

TL Kinetics and parameters

TL kinetic parameters are used to characterize the thermoluminescent behavior of a material. These parameters provide insights into the trapping and retrapping processes involved in TL. The following are essential TL kinetic parameters:

- Activation Energy (E_a): Activation energy represents the energy barrier that trapped electrons need to overcome in order to be released from traps during the heating process. It is a measure of the depth of the traps in the material.
- Frequency Factor (s): The frequency factor is a measure of the probability of retrapping events. It represents the frequency of thermally activated transitions of trapped electrons from traps to the conduction band during the heating process.
- Order of Kinetics (b): The order of kinetics describes the order of the TL process, which can be first-order, second-order, or higher. It indicates the dependence of the TL intensity on temperature and provides information about the complexity of the trapping and retrapping processes. Trapping Level Distribution: This parameter describes the distribution of trap energies within the material. It provides information about the diversity and density of trap states involved in the TL process.
- Peak Temperature (T_m): The peak temperature represents the temperature at which the maximum TL intensity is observed. It can provide information about the dominant trap depth or trap distribution in the material.

These kinetic parameters are determined through various experimental techniques, which involves measuring the emitted light intensity as a function of temperature during the heating process. By studying these kinetic parameters, researchers can gain insights into the underlying physics and mechanisms of TL, understand the properties of traps in materials, and optimize the performance of TL materials for dosimetry and dating applications.

TL kinetic orders refer to the order of the TL process, indicating the relationship between the TL intensity and the temperature. The kinetic order provides information about the complexity of the trapping and retrapping processes involved. The kinetic orders commonly observed in TL are as follows:

- First-Order Kinetics (Randall-Wilkins Approach): In first-order kinetics, the TL intensity is directly proportional to the number of trapped electrons or the concentration of traps. The rate of retrapping events is primarily determined by the thermal energy provided during the heating process. Many TL materials exhibit first-order kinetics under certain conditions (Randall & Wilkins, 1945).
- Second-Order Kinetics (Garlick-Gibson Approach): Second-order kinetics occur when the TL intensity is proportional to the square of the trapped electron concentration or the concentration of traps. This suggests that multiple trapped electrons or multiple traps are involved in the TL process. Second-order kinetics are less common but can occur in certain TL materials (Garlick & Gibson, 1948).

- General Order Kinetics (May-Partridge Approach): Some TL materials may exhibit a combination of first- and second-order kinetics. This indicates the presence of multiple types of traps with different energies or different retrapping mechanisms contributing to the overall TL process (May & Partridge, 1964). Furthermore, the general order kinetics equation has undergone modifications by various researchers . (Kitis, et al., 1998; Gomez-Ros & Kitis, 2002)

Determining the kinetic order is important for understanding the nature of the trapping and retrapping processes, as well as optimizing the performance of TL materials for specific applications. By analyzing the geometry of the TL intensity-temperature curves, the kinetic order can be determined. Moreover, it is important to note that the kinetic order can vary depending on the specific characteristics of the material, such as its composition, defect structure, and thermal history. Therefore, the determination of the kinetic order in TL is often determined experimentally for each material.

Numerous techniques exist for conducting glow curve analysis with the aim of determining kinetic parameters. The methods used in this thesis are described in detail under the respective section.

2. LITERATURE REVIEW

This chapter provides an overview of the literature sources that were researched and used within the scope of the thesis.

Tridymite, a polymorph of quartz, has attracted considerable scientific interest due to its unique crystallographic structure and potential applications in various fields. In recent years, several analytical techniques have been employed to investigate the properties and characteristics of tridymite, yet are insufficient. This literature review aims to provide an overview of the studies conducted on tridymite analysis related to this thesis.

A dedicated study by Aparicio et al., investigating metamorphic xenoliths (including tridymite studied in this thesis) discovered within the basaltic Timanfaya lavas elucidates the impact of sedimentary and metamorphic rocks on the original basanitic magma. This research underscores how the contamination and influence from these geological sources shape the composition and characteristics of the magma (Aparicio, et al., 2006). Also another report by Bustillo et al., highlights that the positioning of Lanzarote on the oceanic slope of the Tarfaya-Aiun basin, in conjunction with the topographical characteristics resulting from submarine volcanism, plays a crucial role in shaping the potential formation of artesian wells. These conditions provide a plausible framework for understanding the occurrence of rapid cooling processes observed within the area (Bustillo, et al., 1994).

The scarcity of crystallographic data on orthorhombic tridymite in space group C2221 can be attributed to the intricate nature arising from impurity presence and diverse polymorphic structures. Typically, orthorhombic tridymite exhibits stability within the temperature range of 190°C to 380°C, which corresponds to the transition from a hexagonal to an orthorhombic structure during the cooling process. The crystal structure of orthorhombic tridymite obtained from the Steinbach meteorite was initially characterized by Dollase, while Kihara et al. conducted a comprehensive investigation of synthetic orthorhombic tridymite utilizing single-crystal XRD techniques (Dollase, 1967; Kihara, et al., 1986; Takada, et al., 2018; Lee & Xu, 2019).

The structure of orthorhombic tridymite with C2221 symmetry including its anisotropic atomic displacement parameters (ADPs), was investigated by Lee and Xu using synchrotron XRD, pair distribution function (PDF), and transmission electron microscopy. Rietveld refinement was employed to determine the unit-cell parameters, fractional coordinates, and isotropic atomic displacement parameters (Uiso) of tridymite (Lee & Xu, 2019).

Numerous meta-stable varieties of tridymite have been documented, categorized into two main groups: MC (monoclinic) and PO (pseudo-orthorhombic). The majority of naturally occurring tridymite samples fall into the PO group, exhibiting various unit cells. In contrast, MC tridymite is commonly found in meteoritic and synthetic samples. However, an exceptional occurrence of MC tridymite has been reported in fired silica bricks and dacitic rocks from the Tugawara area in Japan, making it a unique case among tridymite samples found on Earth (Hirose, et al., 2005).

In a reported study, The SEM micrographs displayed uniformly distributed and even polymeric surfaces in the geopolymers produced using devitrified glass waste containing the highest amount of tridymite. Conversely, geopolymers made with raw glass waste exhibited numerous unreacted particles due to its lower reactivity during the alkalination process. Furthermore, the EDS analysis verified the effectiveness of the mixture designing procedure in achieving the desired molar ratio of SiO_2/Al_2O_3 and the successful formation of the geopolymers (Dadsetan, et al., 2021).

According to Zamiatina et al., the Raman bands of tridymite, specifically the α-tridymite (orthorhombic modification), were found to have average positions at 193–195 cm^{-1}, 261 cm^{-1}, 405–408 cm^{-1}, and 460–464 cm^{-1}. In some cases, a single band at 405–408 cm^{-1} was observed instead of the expected doublet near 402 cm^{-1} and 418 cm^{-1}. They suggested that this discrepancy may be attributed to band broadening or crystal structure orientation effects, where impurities, defects, or crystal orientation can influence the Raman spectrum (Zamiatina, et al., 2023).

Also it was reported that unpolarized micro-Raman spectra of tridymite modifications were collected and compiled in Figure 2.1 (Kanzaki, 2019). Each spectrum presented in the figure is considered representative of the corresponding sample which are MC (Steinbach meteorite), MC (synthetic), MX-1 (synthetic), PO-10 (Vechec, Slovakia), PO-10 (Mt. Arci, Italy).

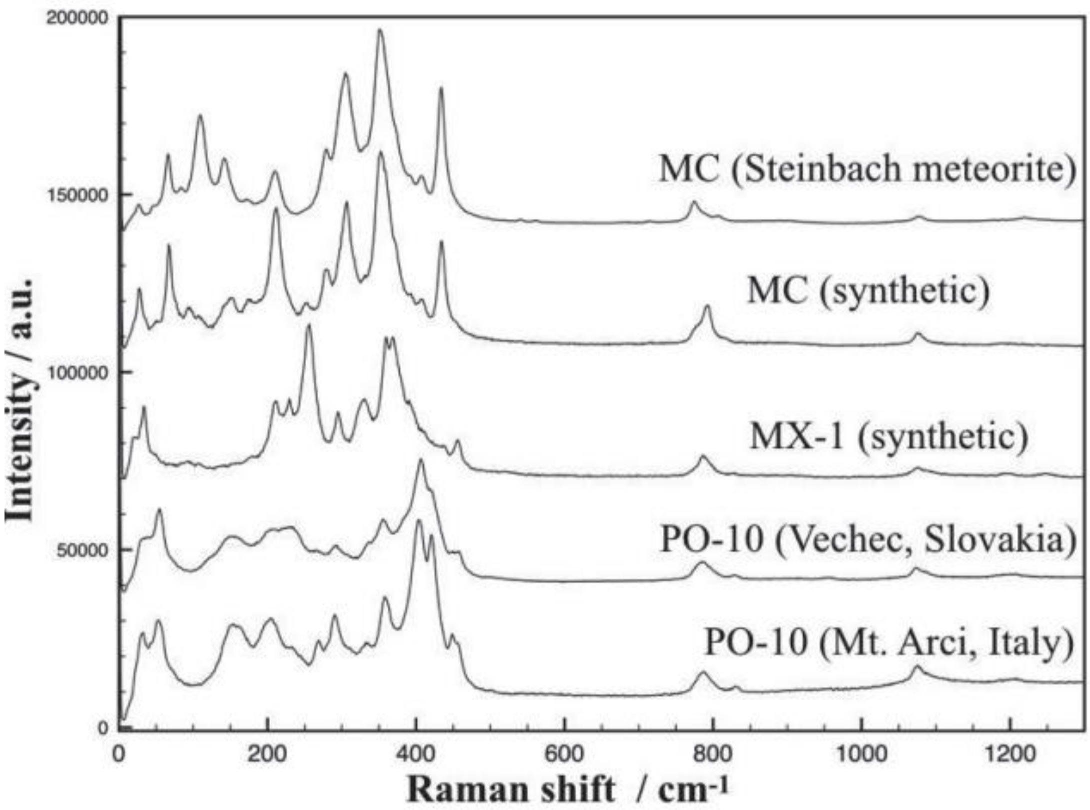

Figure 2.1. Unpolarized micro-Raman spectra of tridymite modifications from different origins.

Furthermore, Kanzaki conducted in-situ high-temperature Raman spectroscopy on tridymite, specifically focusing on the MC modification, and measured spectra up to 500 °C and cooling down to 60 °C. Notably, he reported the low-frequency Raman spectra (ν = 15–100 cm^-1) of the high-temperature modifications (OP, OS, OC, and HP) for the first time. He thoroughly discussed the discrepancy in the transition temperature and provided insights into this matter as follows: Transition sequence starting from MC to OP (at about 110 °C), OP to OS (150 °C), OS to OC (190 °C), OC to HP (380 °C), and same for the reverse direction (Kanzaki, 2020).

A systematic investigation was conducted to analyze the Raman spectra of MC and PO-10 under varying pressure conditions, including compression and decompression. The study aimed to elucidate the origins of these modifications by examining the pressure-dependent changes in Raman peak positions. This study has unveiled a novel pathway for the formation of PO-10 from MC, shedding light on its significance in the context of shocked meteorites. While PO-10 is commonly found in volcanic rocks on Earth without the need for high pressure, its formation in shocked meteorites presents a different scenario. Tridymite MC is the predominant silica polymorph observed in meteorites, and when a meteorite containing MC experiences a mild impact ($p \geq 0.35$ GPa), PO-10 can form and persist. Recent discoveries have confirmed the presence of PO-10 in meteorites, indicating its formation through shock events. However, it should be noted that this study is based on static high-pressure experiments conducted at room temperature, with significantly longer pressure loading times compared to actual shock events. Therefore, the direct applicability of these findings to impacted meteorites remains uncertain. Further investigations considering transition kinetics are necessary to explore this intriguing transition phenomenon. Nevertheless, comprehending the modifications of tridymite and establishing the conditions under which they form will provide valuable insights into the thermal and impact history of tridymite-bearing meteorites (Kanzaki, 2021).

As it was reported, the ^{29}Si MAS NMR spectrum of the 3rd RT modification of tridymite (L3-To(MX-1)) reveals ten signals that are partially resolved, and these signals can be attributed to 24 symmetrically independent silicon atoms. The incommensurate superstructure was examined through single crystal X-ray diffraction data, indicating that the modulation comprises a sophisticated arrangement of tilted tetrahedra. This arrangement can be characterized as a combination of transverse and longitudinal wave like shifts of the atoms, while the tetrahedral units themselves remain relatively undistorted (Graetsch & Topalovic-Dierdorf, 1996).

Another ^{29}Si MAS NMR spectrum of tridymite were recorded at five different temperatures which are 21, 142, 202, 249, and 401 ^{o}C (Figure 2.2) (Kitchin, et al., 1996). It was reported intriguing variations in the spectra as the temperature changed. At RT, the tridymite spectrum exhibited 8 maxima with MC symmetry (Figure 2.2.a). As the temperature increased to 142 ^{o}C, the spectrum transformed, showing only 3 maxima centered around 113-114 ppm with OP symmetry (Figure 2.2.b). As the temperature surpassed 160 ^{o}C, the spectrum underwent significant changes. First, it evolved into a narrower, slightly asymmetric line (Figure 2.2.c). Then, above 210°C, it transitioned into a narrow symmetrical line (Figure 2.2.d). Finally, with further temperature increase up to 450°C, only a small and gradual shift to lower frequencies was observed (Figure 2.2.e).

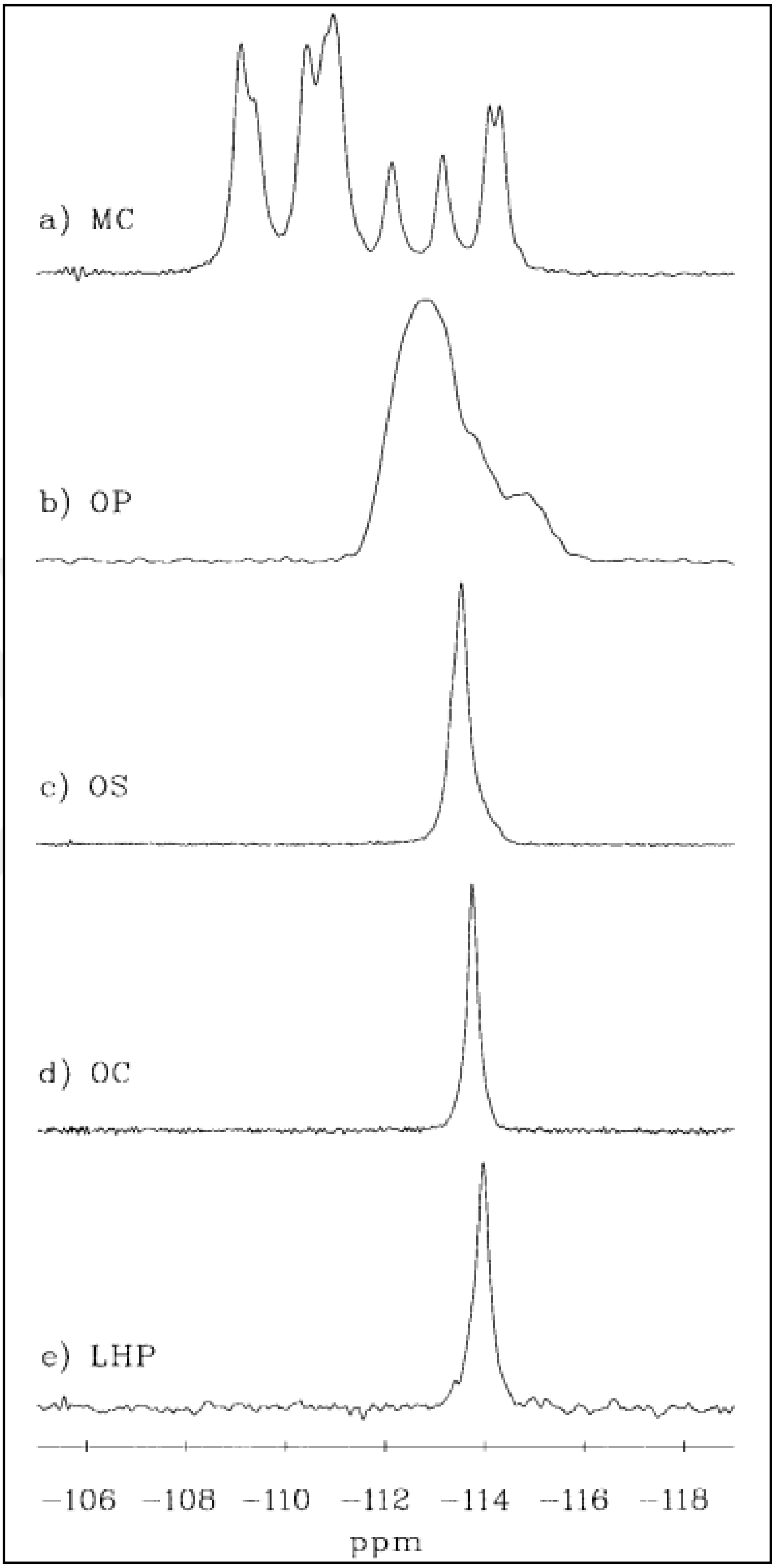

Figure 2.2. The ^{29}Si MAS NMR spectra of tridymite were recorded at five different remperatures: a) 21, b) 142, c) 202, d) 249, and e) 401 ^{o}C.

In a study, it was reported that tridymite in andesite and obsidian exhibits bright blue emissions in color CL images. The CL spectra of tridymite reveal emission band at 430 nm. The CL intensity of tridymite decreases as the electron irradiation time increases, similar to the short-lived blue luminescence observed in hydrothermal quartz. However, the reduction rate of the CL intensity in hydrothermal quartz is relatively small compared to tridymite. Notably, the initial CL intensity of the mineral immediately after electron irradiation shows a positive correlation with the Al_2O_3 content, indicating that the blue emissions of tridymite may be attributed to the $[AlO_4/M^+]^0$ defect center (where M stands for H^+, Li^+, Na^+, and K^+). The electron irradiation of tridymite results in the diffusion of monovalent cations like H^+, Li^+, and Na^+ and leads to the disruption of their crystal structure, causing the short-lived blue luminescence. On the other hand, the CL intensity after 600 seconds of electron irradiation depends on the K_2O impurity content, where the large ionic radius of K^+ prevents its diffusion. Therefore, the CL emissions of tridymite after 600 seconds of electron irradiation can be attributed to the $[AlO_4/M^+]^0$ defect (where M: K^+) (Kayama, et al., 2009).

A packed tridymite called $BaAl_2O_4$ is utilized as a long-lasting phosphor. It is reported that $BaAl_2O_4$ produced through solution combustion exhibits TL. Following annealing at 1200 °C, analysis of the sample using X-ray diffraction reveals that it developed as a single phase compound with a hexagonal shape. Due to stimulation at 248 nm, a wide PL emission band between 300 and 650 nm was found. The phosphor displayed a natural TL peak for measurement at 1 $^oCs^{-1}$ at 102 °C and, after being exposed to 100 Gy of beta radiation, two broad peaks for heating at 1 $^oCs^{-1}$ at 123 and 318 °C. The examination of the primary glow peak at 123 °C indicates that it is made up of a number of collocated peaks, or peaks that are embedded within one another (Pandey & Chithambo, 2018).

3. MATERIALS AND METHODS

This chapter presents comprehensive information regarding the utilized materials and experimental techniques.

3.1. Mineral: Tridymite

Tridymite is a high-temperature polymorph of silica (SiO_2) and is commonly found in volcanic rocks. It has been identified on Mars, specifically in sedimentary rocks within the Gale Crater, by the Mars Science Laboratory (MSL) mission's Curiosity rover. Its presence on Mars provides valuable insights into the geological history and environmental conditions of the planet. Studying tridymite on Mars can also help scientists make comparisons between Martian geological processes and those observed on Earth, enhancing our understanding of both planetary bodies (Morris, et al., 2016; Kayama, et al., 2018; Yen, et al., 2021; Payre, et al., 2022). It is essential to attempt to comprehend the physical and chemical properties of the tridymite mineral in order to draw inferences about Mars' habitability.

Since silicon and oxygen are the two most abundant elements in the earth's crust, the presence of these elements in many minerals is not surprising. In Figure 3.1, the weight ratios of the common elements in the earth crush (Figure 3.1 left) and the ratios according to the atomic number (Figure 3.1 right) are given approximately (Miller & Spoolman, 2012; Monroe & Wicander, 2001). Silica is the result of the chemical bonding of silicon and oxygen, while minerals that contain silica are classified as silicates.

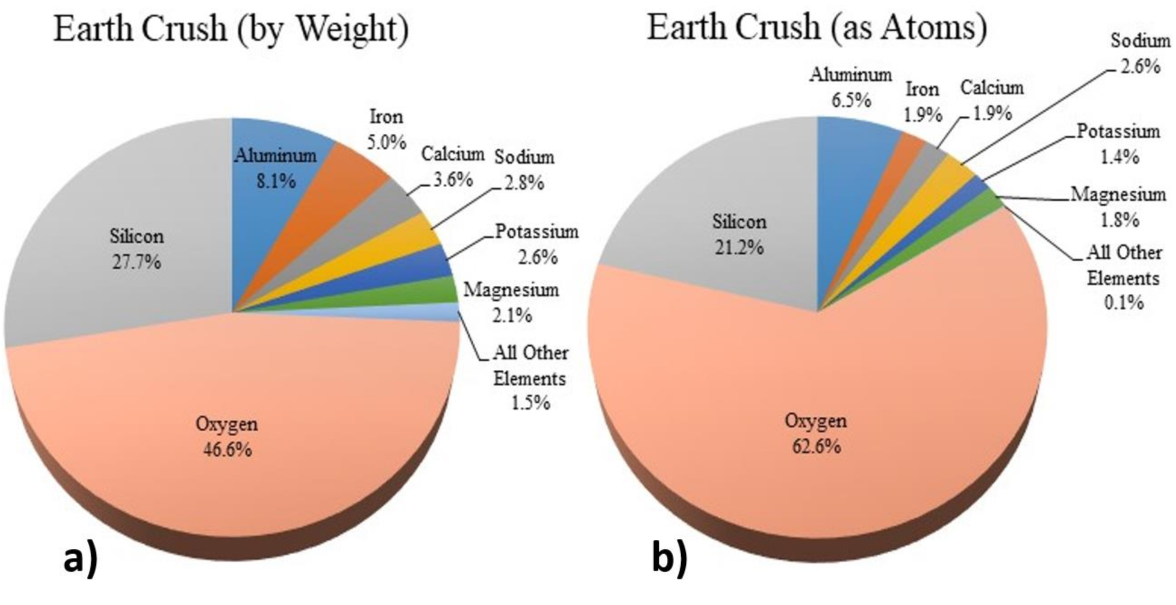

Figure 3.1. a) The weight ratios of the common elements in the earth crust, b) the ratios according to the atomic number.

Silicates with the general composition SiO_2 contain many polymorphs. α- and β-quartz, α- and β-tridymite, α- and β-cristobalite, coesite, stishovite and opal are the main important silica polymorphs.

In these polymorphs, four oxygen atoms, composing a tetrahedral SiO_4^{4-} group, surround silicon and it is shown in the representational Figure 3.2.a (this is not valid for stishovite). The circles in the corners of the tetrahedron simulate oxygen atoms and a dot symbolizes the silicon atom in the center. In Figure 3.2.b the lines represent O--O bonds and in order to easy illustration; only the corners of the tetrahedron are shown and the atoms are omitted in the representation. A tetrahedron looks like a trigonal pyramid from the top can be seen in Figure 3.2.c (Wenk & Bulakh, 2004).

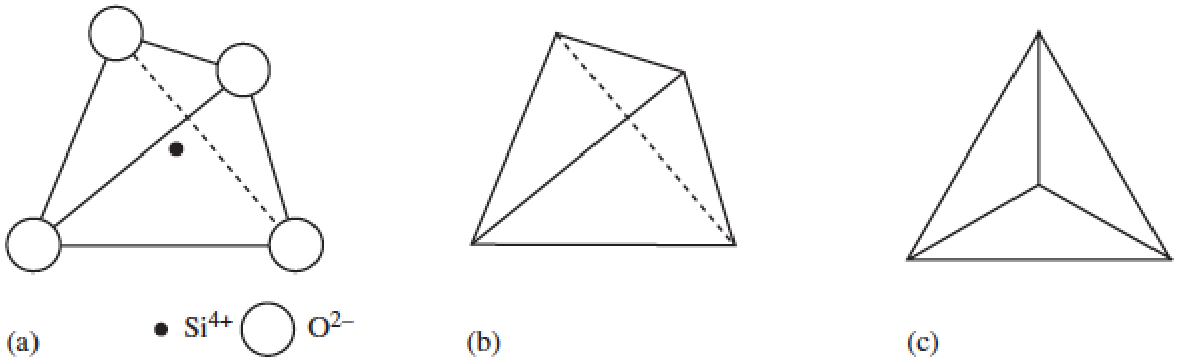

Figure 3.2. SiO_4^{4-} tetrahedron. The O atoms are at the apices and Si atom is in the center. (a) Representation with ions shown. (b) Representation without ions. (c) View from above an apex (Wenk & Bulakh, 2004).

There are complex ionic-covalent bonds between silicon and oxygen atoms. The tetrahedral share each oxygen vertex with another tetrahedron, forming an infinite 3-dimensional frame. There are several ways in which such linkages can occur, and the way of the link determines the appearance of representations of the various polymorphs as well as their crystal structure. The tetrahedron, the most fundamental unit of silicates, seems to be very simple, but have very complex structures because the ways of combining tetrahedral shape in a crystalline structure are so diverse and entangled. These various structures can have cubic, hexagonal, tetragonal, trigonal, orthorhombic or monoclinic symmetry (Götze, et al., 2001).

Research has demonstrated that quartz contains a significant number of displaced atoms and diverse ions, which are located in both regular lattice and interstitial positions (Götze & Plötze, 1997). Quartz and tridymite exhibit shared defects due to their common origin. The schematic representation of the quartz structure shown in Figure 3.3 (directly taken from the article (Götze, et al., 2001)) illustrates the prevalent intrinsic and extrinsic lattice defects.

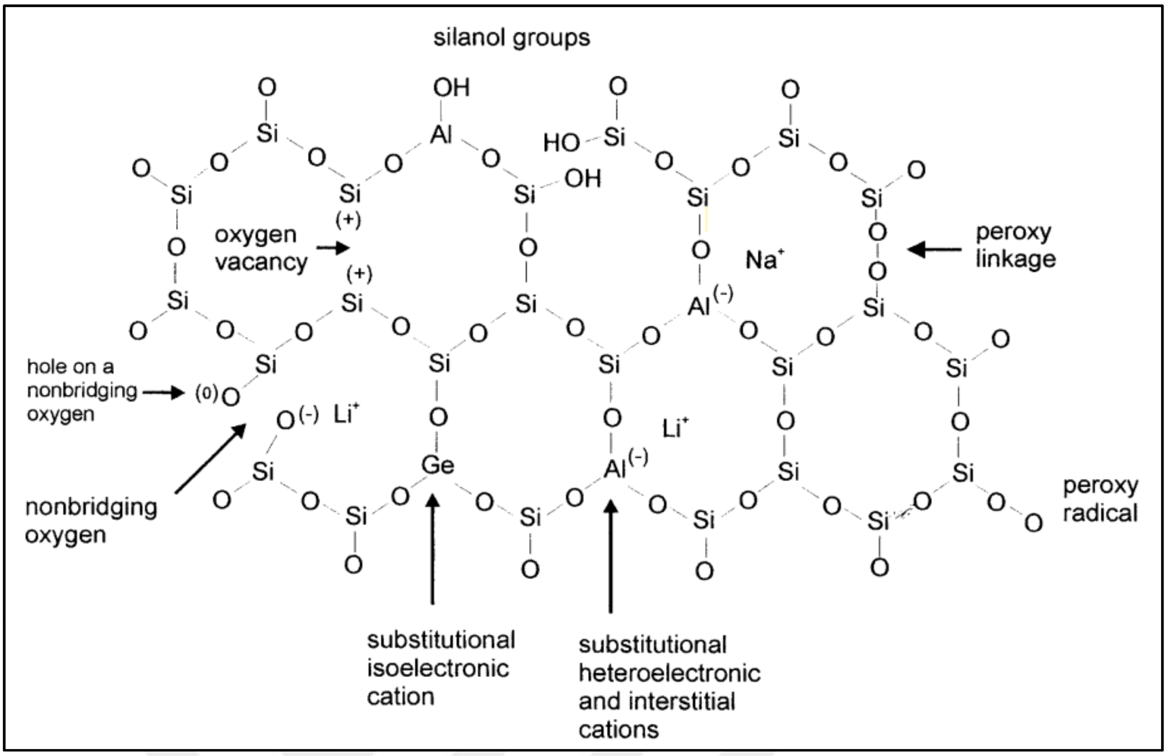

Figure 3.3. The diagram of the quartz structure illustrates the prevalent intrinsic and extrinsic lattice defects (Götze, et al., 2001).

The stability field of tridymite can be briefly summarized:

- Category: oxide mineral (tectosilicate)
- Crystal system: Orthorombic (alpha-tridymite), and monoclinic (beta-tridymite) (generally at RT)
- Formula mass: 60.08 g/mol
- Mass scale: 7
- Non-radioactive, non-magnetic, fluorescent

3.1.1. Tridymite Forming

Paramorphic transition between the different polymorphs may occur as a result of physically breaking bonds to form new structural configurations due to changes in temperature and/or pressure because of the fact that the polymorphs of silicates have the same chemical composition but different crystal structure (Nie & Byrn, 2018; Zamiatina, et al., 2023). Figure 3.4 shows different silica polymorphs under various conditions of temperature and pressure (Swamy, et al., 1994; Zamiatina, et al., 2023).

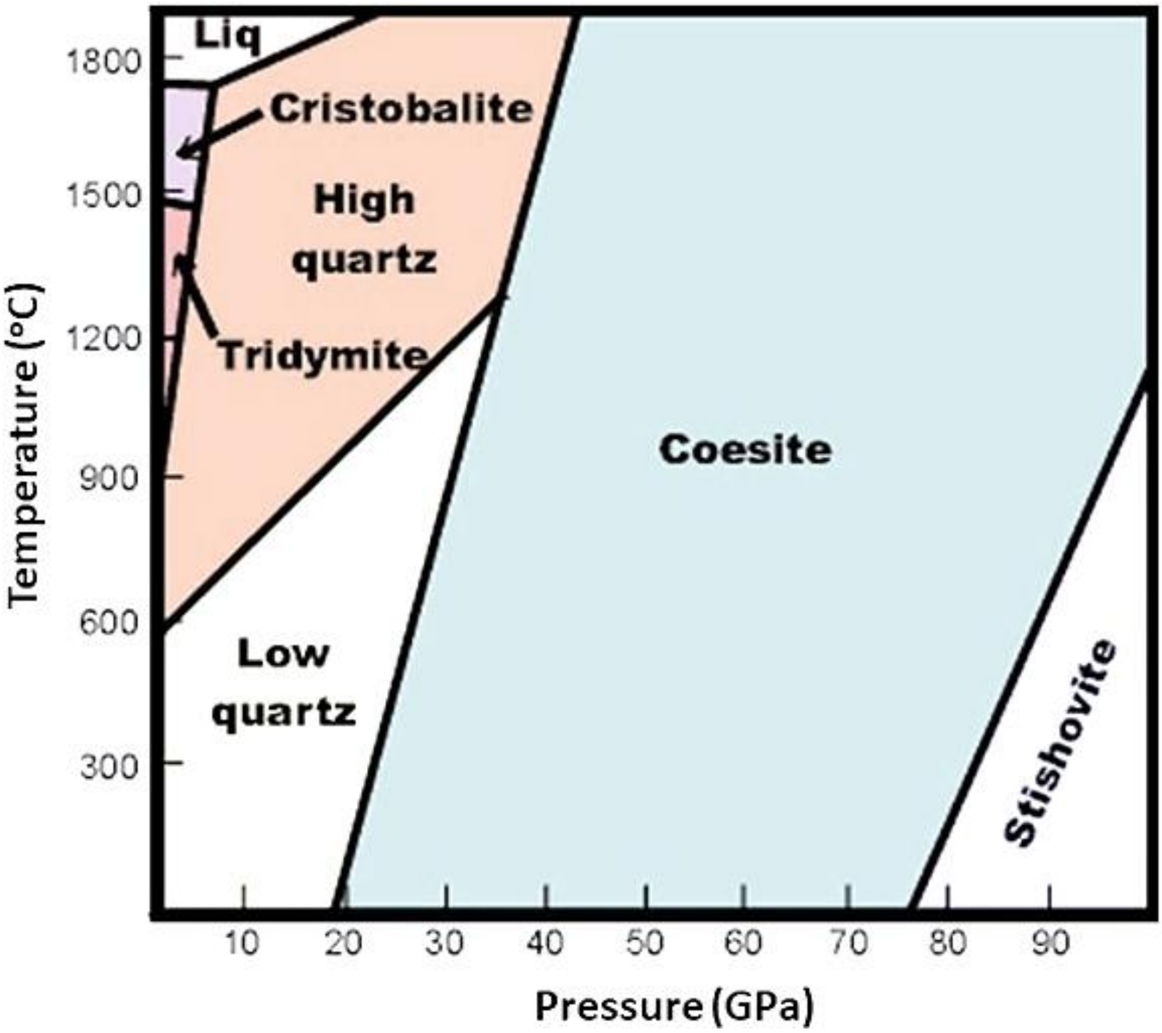

Figure 3.4. Silica forms polymorphs under varying circumstances of temperature and pressure (The diagram was created by Dr. Javier Garcia-Guinea).

It is assumed that the tridymite mineral employed in this thesis was created when the lava explosion encountered the cold water. The lava bomb, which found an appropriate way out of the planet's magma layer by seismic activity and was spread on the surface, contains liquid silica and also trace amounts of all other elements compared to silica. Also, in numerous geological instances demonstrating the development of low-tridymite suggest the presence of hydrothermal solutions as the medium of deposition (Lee & Xu, 2019).

The following inferences and diagram (Figure 3.5) have been generated based on published numerical data (Kahraman, et al., 2005).

Opal(CT) (defined as poorly crystalized) was formed when liquid silica slow progressively cools to RT. More amorphous structures such as opal and obsidian were formed when liquid silica met with cold water between 2000 and 1713 ^{o}C and rapidly cooled down to RT. (It is predicted that the lava bombs fall into the ocean where around the volcanic mountain, depending on environmental conditions in Lanzarote, Canary Island). β-Cristobalite was formed when liquid silica, at the temperatures between 1713 and 1470 ^{o}C, met with cold water and rapidly decreased to

RT. However, β-cristobalite reversibly turns into α-cristobalite if heated from RT to temperatures between 220 and 274 ^{o}C. β-Tridymite was formed when liquid silica, between the temperatures of 1470 and 847 ^{o}C, met with cold water and rapidly cooled down to RT. Also, β-tridymite reversibly transforms into α-tridymite when heated from RT to temperatures of between 116 and 163 °C. β-quartz was formed when liquid silica, at the temperature below 847 °C, met with cold water and rapidly decreased to RT. Additionally, β-quartz transforms reversibly into α-quartz if it is heated from RT to about 573 ^{o}C (Figure 3.5).

According to the report, the geographical location of Lanzarote on the oceanic slope of the Tarfaya-Aiun basin, coupled with the topographical features resulting from submarine volcanism, have been identified as significant factors that can potentially influence the formation of artesian wells. These conditions offer a plausible explanation for the occurrence of rapid cooling processes observed in the area (Bustillo, et al., 1994).

Furthermore, a study focused on metamorphic xenoliths found within the basaltic Timanfaya lavas. It demonstrates how the original basanitic magma was influenced and contaminated by sedimentary and metamorphic rocks (Aparicio, et al., 2006).

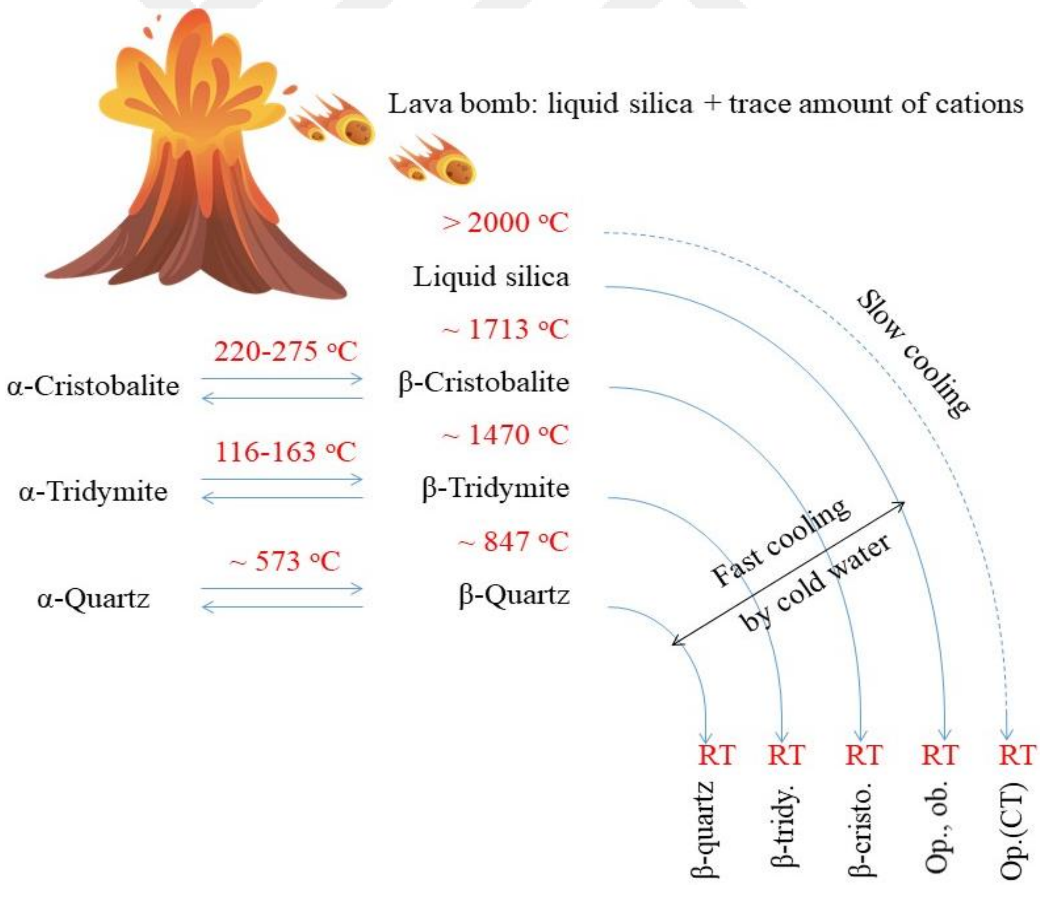

Figure 3.5. Hydrothermal transitions between different polymorphs of silica from the lava bomb. Temperature values could be changed by different impurity, pressure, and heating-cooling rate parameters. The figure was created using the data obtained from the reference (Kahraman, et al., 2005).

3.1.2. Geographical Location of the Sample

The Timanfaya eruption, spanning from 1730 to 1736, holds the distinction of being the longest recorded eruption in the Canary Archipelago, Spain (Figure 3.6). Numerous mineralogical and chemical studies have reported the abundance of silica in the lavas of Timanfaya. In line with these findings, tridymite samples utilized in this thesis were extracted from melted silica-rich sedimentary rocks sourced from Lanzarote, one of the Canary Islands. The selection of these tridymite samples allows for an examination of their properties and contributes to a deeper understanding of the volcanic processes associated with the Timanfaya eruption (Aparicio, et al., 2006).

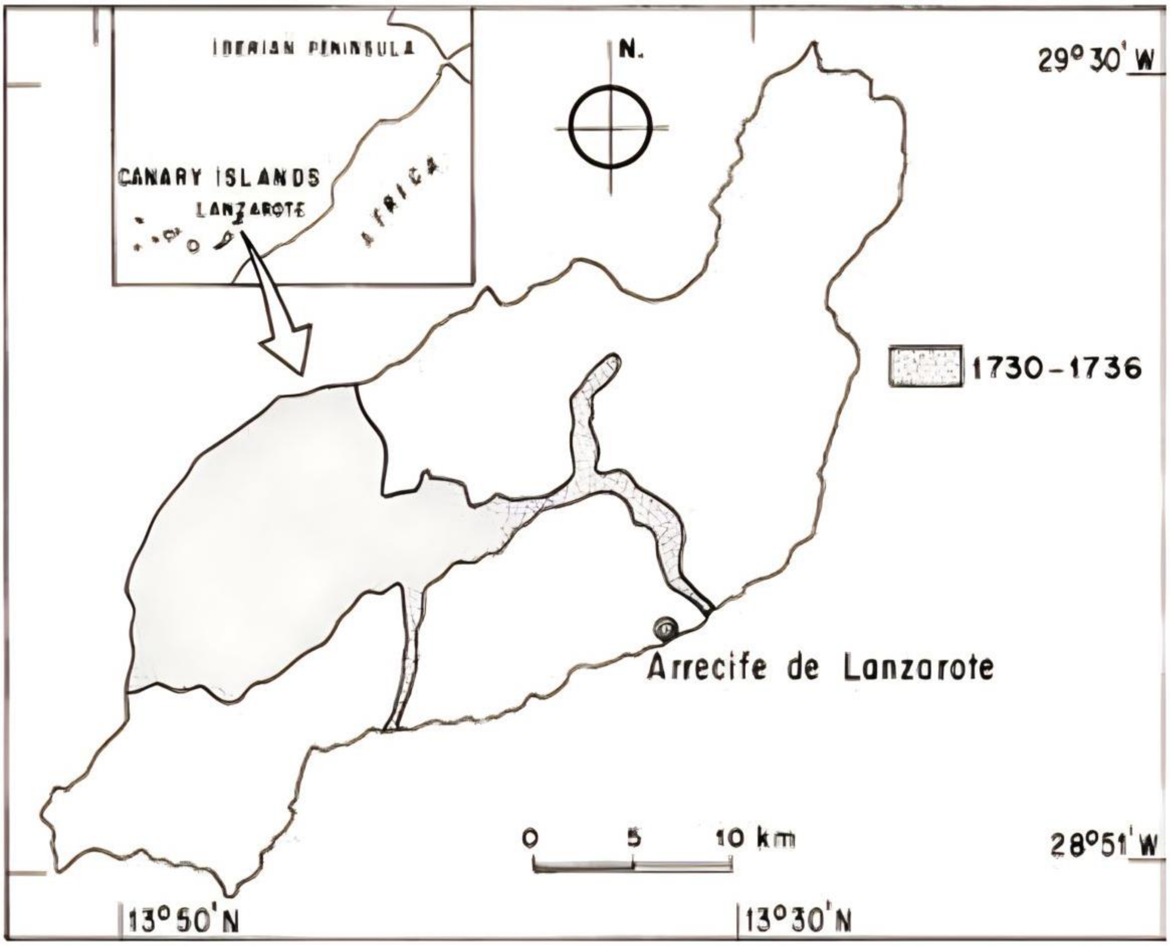

Figure 3.6. Schematic view of Lanzarote Island showing the location of 1730-1736 Timanfaya lava eruptions (Aparicio, et al., 2006).

The xenolits obtained from the region effected by Timanfaya eruption are marked in blue on the ternary diagram, and tridymite is also highlighted (Figure 3.7).

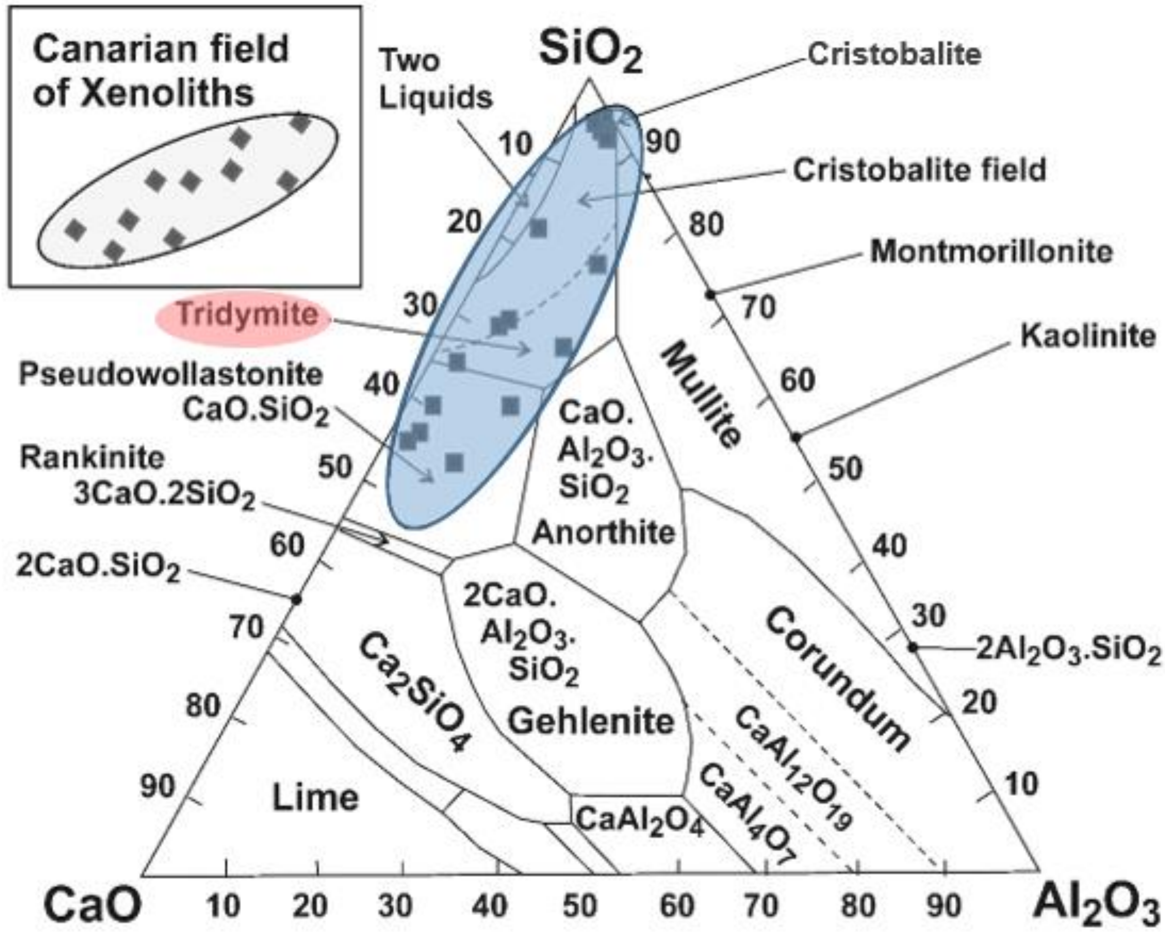

Figure 3.7. Representation of composites of the Xenoliths samples in Canary Island (diagram was created by Dr. Javier Garcia-Guinea).

3.1.3. Powder Sample Preparation

The impurities present in the lattice structure of a phosphor can either be caused to active (creating new traps that produce TL signal) or absorb (causing quantum tunneling) the TL intensity that generates the glow curve. For this reason, it is best to keep natural samples isolated from other elemental substances when conserving and preparing them to be used in research. Furthermore, it should be ensured that samples are kept in an environment that is free from potential sources of contamination, such as abrasives, hand-touching, and the area where analyses are performed.

Powder sample preparation of tridymite, a polymorph of quartz, follows similar principles to general powder sample preparation techniques. Tridymite is commonly analyzed in materials science, geology, and other related fields to understand its crystallographic structure, composition, and properties. The first step in tridymite sample preparation involves obtaining a representative and homogeneous sample. It is essential to ensure the sample represents the desired tridymite phase without significant contamination from other minerals or impurities. Once the tridymite sample is obtained (Figure 3.8.a for bulk and Figure 3.8.b for cross-sectional area of tridymite sample), it needs to be reduced to a fine powder form. Various methods, such as mechanical grinding (preferably employed for luminescence analysis), milling, or crushing (which are not conducive to luminescence analysis), are utilized to achieve the comminution of the bulk tridymite material into finer particles. The goal is to achieve a consistent particle size distribution while preserving the chemical and structural integrity of tridymite. Controlling contamination is crucial during the grinding and milling processes. Clean and dedicated equipment, such as agate (Figure 3.8.c) or tungsten carbide mortars and pestles, should be used to minimize contamination from grinding surfaces. It is also important to conduct the grinding process in a controlled environment, such as a clean room or a glove box, to minimize contamination from environmental sources.

Proper powder sample preparation ensures accurate and reliable analysis of tridymite. By obtaining a fine powder (Figure 3.8.d) with controlled particle size distribution and minimizing contamination, it can be studied the crystallographic structure, phase abundance, thermal properties, and other characteristics of tridymite using techniques such as XRD, spectroscopy, microscopy, and elemental analysis. These analyses contribute to a deeper understanding of tridymite's behavior and its applications in various scientific and industrial fields.

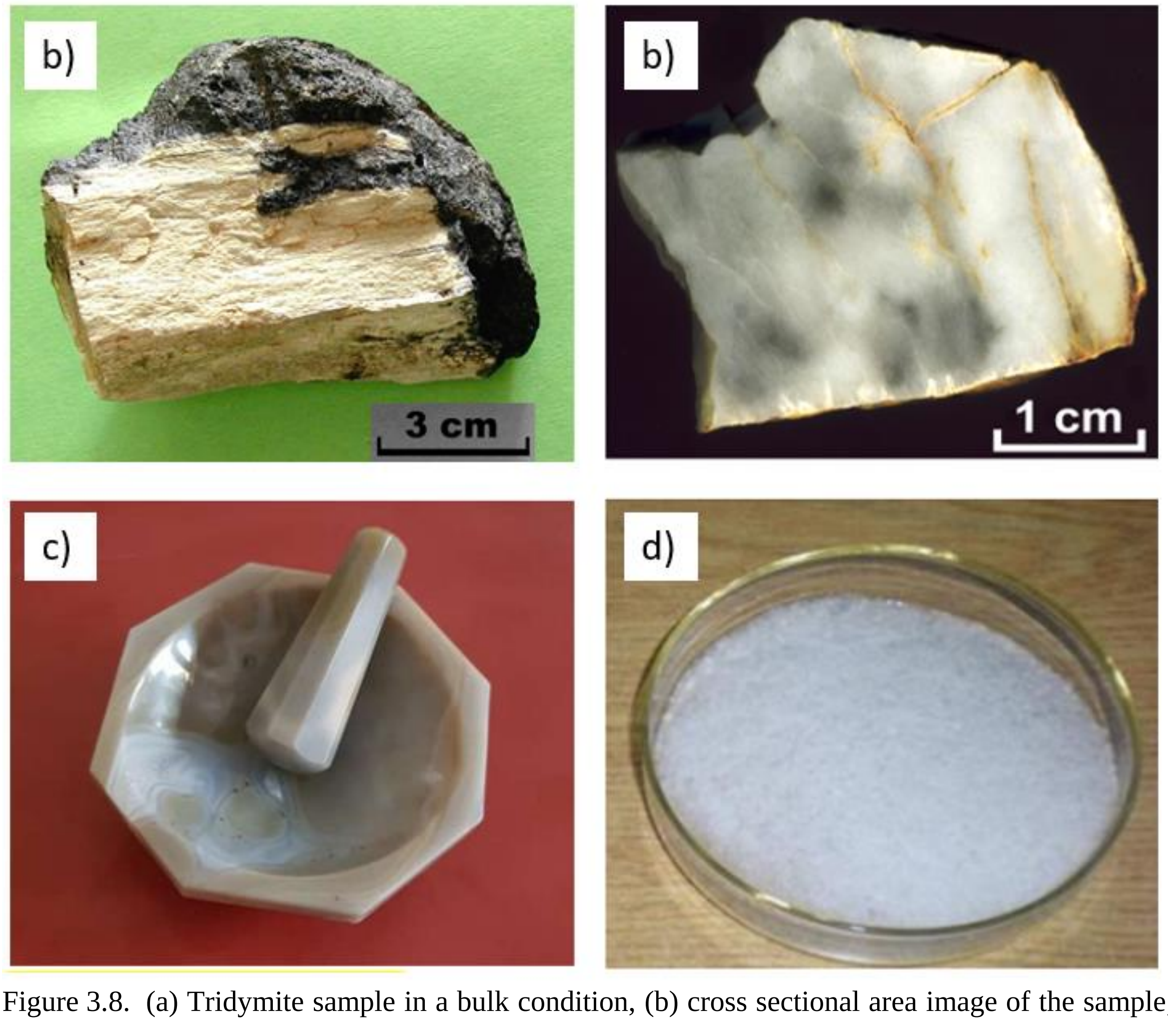

Figure 3.8. (a) Tridymite sample in a bulk condition, (b) cross sectional area image of the sample, (c) an agate mortar, (d) powder sample.

3.2. Equipment and Methods

The tools and devices used in this study are listed below and the basic features of them are explained in detail under relative headings.

- X-ray powder diffractometer reader system (Philips PW1710/00) (T-XRD)
- ESEM model XLS30 from FEI Company (CL and ESEM-EDS)
- JEOL Superprobe JXA-8900M (EPMA)
- Thermo Fisher DXR Raman microscope (Raman-PL)
- ^{29}Si MAS NMR spectrometer (NMR)
- JEOL Jes-FA300 X-band EPR spectrometer (EPR)
- Riso TL/OSL reader system model DA-12 (TL)
- Agate mortar
- Sieve
- Pure water device

3.2.1. Thermal X-Ray Diffraction

In this thesis, T-XRD measurements of powder tridymite samples (under 90 μm) were performed, and the diffraction patterns at various temperatures (starting from RT to 200 ^{o}C and vice versa) were compared graphically. Utilizing a Philips PW1710/00 diffractometer with a Ni filtered CuKα (1.54 Å) radiation source and configurations of 40 kV and 40 mA, a graphite monochromator was employed to perform T-XRD characterization. Step scanning from 2^{o} to 64^{o} (2θ in steps of 0.020^{o}; 4 s per step) resulted the patterns.

3.2.2. Environmental Scanning Electron Microscope - Energy Dispersive X-ray Spectroscopy

In this thesis, ESEM analyzes were carried out to obtain information about the characteristic features of the tridymite sample such as morphological properties, chemical composition and crystallography. Within the framework of this thesis, tridymite samples underwent examination on polished surfaces in an environment of low vacuum. The measurement process employed an FEI Company ESEM model XLS30 (Figure 3.9), without the application of any coating to preserve the emission pathways of the samples. For chemical elemental spot-analysis and the recording of backscattered electron (BSE) mode images, EDS was utilized. These techniques and instruments provided valuable insights and data for the analysis of the tridymite samples in this study. Furthermore, the Inspect ESEM (FEI Company) was employed in conjunction with a Gatan MonoCL3 detector and a PA-3 photomultiplier tube to detect the spectral CL emission which was in section 3.2.7 (Garcia-Guinea, et al., 2011).

Figure 3.9. SEM-EDS model XLS30 located at National Museum of Natural Sciences in Madrid, Spain.

3.2.3. Electron Probe Micro Analyser

In order to perform nondestructive chemical analyses of major and minor elements to determine the chemical homogeneity, the sample was bound together with a polymer and carefully polished to offer the EMPA beam a planar surface. The probe's spot size was approximately 5 µm, and the operating conditions were 15 kV and 20 nA. On a basis of data series of electron microprobe analyses (JEOL Superprobe JXA-8900M), bulk and channel selected (TAP, PETJ, LIF, PETH) X-ray spectra search, and identification routines, the crystal-chemical characteristics of sample were determined. Natural and synthetic crystals from the collection of the "Servicio de Microsco p'a Electro'nica Lluis Bru" at the Universidad Complutense de Madrid were used as standards (Sanchez-Munoz, et al., 2006).

3.2.4. Raman Spectroscopy

Raman spectroscopy and PL measurements could be performed on a sample using the same device, such as a spectrofluorometer or spectroscopic system. A typical spectrofluorometer typically included a light source, a sample holder, a monochromator or filters for wavelength selection, and detectors to measure the intensity of the emitted or scattered light. The scattered light is typically collected at different angles (e.g., 90 degrees or backscattered) to maximize the Raman signal.

For Raman spectroscopy of tridymite, a laser was used to excite the sample, and the scattered light was collected and analyzed for wavelength shifts resulting from the Raman effect. The resulting Raman spectrum provided information about the vibrational modes and molecular structure of tridymite.

In this study, the Raman spectroscopy was conducted utilizing a Thermo Fisher DXR Raman microscope (West Palm Beach, FL 33407, USA) as seen in Figure 3.10. The confocal microscope's 20X objective was employed, which possesses a point-and-shot Raman capability of 1 μm spatial resolution. The laser source utilized was at 532 nm with a laser power mode of 100% and 10 mW (Garcia-Guinea, et al., 2017).

Figure 3.10. Thermo Fisher DXR Raman microscope used for Raman spectroscopy, located at National Museum of Natural Sciences in Madrid, Spain.

3.2.5. Nuclear Magnetic Resonance

In this thesis, tridymite samples were subjected to NMR measurements at RT using a high-resolution ^{29}Si MAS NMR spectrometer operating at 79.49 MHz. The sample was spun at the magic angle of 54°44" in an MSL-400 (Bruker) spectrometer equipped with a Fourier transform unit in ICMM, Madrid, Spain. The spinning frequency range for the sample was set between 4000 and 5000 cps. In order to capture the Si signal ($I=1/2$), $\pi/2$ (4μs) pulses were employed. To prevent saturation effects, the recycle delay time for the ^{29}Si signal was optimized to 1800s. Chemical shifts for the Si spectrum were recorded in parts per million (ppm) relative to external tetramethylsilane (TMS). For each component, the mean measured chemical shift error was 0.2 ppm. The most useful metric gained from NMR investigations is the chemical shift or shielding, which describes how much the Si nucleus is protected from the surrounding magnetic field by neighboring electrons. Si atoms are insulated differently and absorb radiation at various frequencies in various crystallochemical sites. Approximately 50 accumulations were performed for the ^{29}Si signals. The NMR spectra obtained were subjected to fitting using the Bruker WINFIT software. Various Gaussian components with varying linewidths were used for the ^{29}Si signal (I=1/2) (Sanchez-Munoz, et al., 2006).

3.2.6. Electron Paramagnetic Resonance

In this study, the JEOL Jes-FA300 X-band EPR spectrometer located at Selçuk University Advanced Technology and Research Center (İLTEK) was utilized for EPR analysis. EPR spectra of a 100 mg powder sample were recorded using a sample diamagnetic quartz EPR tube with different magnetic field scan widths (500 mT, 80 mT, 10 mT), varying microwave power values (0.001 mW, 0.01 mW, 1 mW, and 5 mW), different temperatures (-150°C to +150°C temperature range and RT), and a modulation width of 0.1 mT. The spectroscopic splitting factor, g-value, of paramagnetic centers was calculated using $MnO(Mn_2^+)$, which is commonly used as a standard on JEOL EPR spectrometers (Figure 3.11).

Figure 3.11. Picture of the EPR spectrometer used for the experiments in this thesis, at ILTEK Laboratory in Konya, Turkey.

3.2.7. Cathodoluminescence

Using a Gatan MonoCL3 detector with a PA-3 photomultiplier tube (PMT) attached to an ESEM model XLS30 from FEI Company (Figure 3.12), the CL spectra of the samples were measured on polished slabs at low vacuum conditions without coating to maintain open paths to the emission. The PMT tube has a spectral range of 250-850 nm, with the blue regions of the spectrum being the most sensitive. Furthermore, EDS was used for chemical elemental spot-analysis and image recording in BSE mode, and 25 kV electron beams were used for CL measurements. Using a retractable parabolic diamond mirror and the PMT, the luminescence signal was obtained and amplified. The sample was placed 15 mm beneath the base of the CL mirror assembly (Correcher & Garcia-Guinea, 2020). The present study reports on the CL analysis conducted in partnership with the National Museum of Natural Sciences of the CSIC (Spanish National Research Council).

Figure 3.12. A picture of Gatan MonoCL3 detector used for the experiments located at National Museum of Natural Sciences in Madrid, Spain.

3.2.8. Photoluminescence

By appropriately configuring the laser sources, filters, and detectors, a spectrofluorometer could be used to perform both Raman spectroscopy and PL measurements on the sample. This allowed to obtain complementary information about the material using a single device. For PL measurements, the laser was used to excite the tridymite sample, and the emitted light (fluorescence or phosphorescence) was collected and measured. The PL spectrum has provided information about the electronic transitions and luminescent properties of tridymite.

The necessary information about the experiment and the figure of the device has been given in section (3.2.4).

3.2.9. Thermoluminescence

The RisØ TL/OSL system model TL DA-12 reader (Figure 3.13 (Correcher, et al., 2019)) is a device used TL measurements. TL is a technique used in dosimetry and dating applications to measure the accumulated radiation dose in materials. The TL DA-12 reader, manufactured by RisØ National Laboratory for Sustainable Energy in Denmark, is specifically designed to read TL and OSL signals from various materials. It consists of several key components, including an EMI 9635 QA PMT, which is an essential part of the detection system. The EMI 9635 QA PMT is a high-sensitivity photomultiplier tube designed to convert light signals into electrical signals with amplification. The TL measurement technique involves heating a sample and measuring the light emitted as a result of the release of trapped electrons. Detailed experimental set up procedures about TL will be given in the following headings.

Figure 3.13. RisØ TL/OSL system model TL DA-12 reader supplied with an EMI 9635 QA photomultiplier

Furthermore, within the scope of this thesis, two distinct types of radiation sources were employed for conducting TL experiments:

- Beta ray as an ionizing radiation (included in the reader) (Figure 3.13),
- UVC as a non-ionizing radiation (Figure 3.14).

Figure 3.14. UVC irradiator

Experimental Setup

All TL measurements were accomplished by using an automated RisØ TL/OSL system model TL DA-12 reader supplied with an EMI 9635 QA photo-multiplier. The TL emission glow curves were observed by using a Melles-Griot blue filter (FIB002) where the wavelength was peaked at 320-480 nm, the FWHM was 80 (16) nm, and the minimum peak transmittance was 60%. Due to material characterization results and CL results, it was decided to perform TL experiments with a blue filter. The system is provided with a $^{90}Sr/^{90}Y$ beta source with a dose rate of 0.010 Gy/s calibrated against a ^{137}Cs gamma source in a secondary standard laboratory (Sarasola-Martin, et al., 2021).

The samples were carefully powdered under 90 μm with an agate pestle and mortar to avoid triboluminescence (Correcher, et al., 2016). TL measurements of the samples were performed with a linear HR from RT to 500 ^{o}C in a N_2 atmosphere. Prior to TL experiments, the energy stored in the traps over time is often emptied by a pre-heating treatment in the furniture upon natural samples. However, in this thesis, an extra furnace annealing process was not considered required since TL background measurements (from RT to 500 ^{o}C) were evaluated prior to each TL measurement (except natural TL experiment). Furthermore, the incandescent background was subtracted from each TL data belonging to each measurement.

The UV exposures were performed with an automated irradiation system developed at CIEMAT (Delgado, et al., 1996). UV illumination was carried out with a TUV-6 W Hg lamp (253.7 nm; UV irradiance at 10 cm was 0.03 W/m^2) and controlled thermal treatments.

The additional parameters related to each experiment are presented below in the underlined headings.

<u>*Natural TL experiment:*</u>

- 3 precisely weighed 5.0(1) mg aliquots of tridymite powder samples were prepared for natural TL emission experiment.
- TL reading with a linear HR of 5 ^{o}C was performed without being subjected to any ionizing or non-ionizing radiation source.

Prior to TL measurements (except NTL experiment), natural samples are typically subjected to a pre-heating treatment in the furnace, which empties the traps of the energy they have accumulated over time. In this investigation, however, it was deemed unnecessary to perform an extra furnace annealing step because TL background data (from RT to 500 ^{o}C) were evaluated prior to each TL measurement.

<u>*Reusability Experiment:*</u>

- 3 precisely weighed 5.0(1) mg aliquots of tridymite powder samples were prepared for reusability experiment.
- 5 consecutive 1.2 Gy beta irradiation to the samples followed by 5 consecutive TL measurements with a linear HR of 5 ^{o}C were performed.

<u>*Dose Response Experiment:*</u>

- 3 precisely weighed 5.0(1) mg aliquots of tridymite powder samples were prepared to be used for TL dose response experiments.
- The exposure doses of the samples to beta irradiation at RT were 0.6, 1.2, 2.4, 3.6, 6, and 9.6 Gy, with TL measurements performed with a linear HR of 5 ^{o}C after each dose.
- The exposure times of the samples to UVC at RT were 0.5, 1, 2, 3, and 4 hours, with TL measurements performed with a linear HR of 5 ^{o}C after each dose.

<u>*T_{max}-T_{stop} Experiment (Trap Distribution Estimation Method) :*</u>

- 5 precisely weighed 5.0(1) mg aliquots of tridymite powder samples were prepared for T_{max}-T_{stop} experiment.
- 1.2 Gy beta irradiation to the samples followed by
    - preheat treatment in the range of 150-270 ^{o}C (in steps of 20 ^{o}C),

- cooling back to RT,
- TL measurement with a linear HR of 5 ^{o}C

were performed, respectively.

Various Hearing Rate Experiment:

- 5 precisely weighed 5.0(1) mg aliquots of tridymite powder samples were prepared for VHR experiment.
- 1.2 Gy beta irradiation to the samples followed by TL measurements at a range of HR temperature values consisting of 3, 4, 5, 6 ^{o}C were performed.

Methods of Analysis

The test of RU is the initial step in investigating the TL characteristics of a material. The aim of this experiment is to validate whether the sample can consistently provide the same results with each usage, in other words, to determine the stability of the crystal defects that act as traps in the lattice structure of the material.

Exceptionally, unlike synthetic materials, a single TL measurement is performed in natural samples prior to any irradiation or excitation (here pre-heating or annealing) process. In this manner, information is obtained regarding the trapped energy over the years since the formation of the sample, and it is called NTL.

Subsequently, the DR experiment is performed;

- to determine the kinetic order,
- to detect the linear range, and
- to determine what the sample could be utilized for environmental, personal, dating, etc.

T_{max}-T_{stop} Method

Prior to investigating the characteristics of the TL glow curve, a thermal stability test (T_{max}-T_{stop}) is performed, assuming the existence of the progressive traps, some of which can be eliminated by preheating treatment. The main purpose of this experiment is to discover whether the traps that determine the alignment of the glow curve have a continuous or discrete distribution. Furthermore, this test provides the number of components involved in the emission process.

T_{max}-T_{stop} test is carried out in accordance with the following procedures:

- Heating treatment to remove the residual signal,
- A fixed amount of dose given,
- A linear heating up to a temperature value of T_{stop} (with a fixed HR value),
- A rapid cooling treatment to RT,

- TL readout (with a fixed HR value),
- Repeat the above list by only changing the T_{stop} value until achieved the desired maximum T_{stop} value.

Accordingly, a specific dose amount is chosen (based on purpose) from the linear region resulting by the DR experiment, and then the methods for separating the peaks are implemented. There are various peak separation techniques, including initial rise (IR), various heating rate (VHR), peak fit (PF), computerized glow curve deconvolution (CGCD), etc.

The following underlined sub-headings provide specific information on the methods employed in this thesis:

Initial Rise Method

The IR approach is predicated on a hypothesis, such as the assumption that the amount of trapped electrons in the low-temperature tail of a peak is stable (i.e., linear) and temperature dependency is minimal. This method is only applicable to the initial 10% of the TL signal`s maximum peak value (Bailiff, et al., 2005). Equation (1) demonstrates that this side of the peak exhibits an exponential dependence (independent of the kinetic order) and the applicability of the pseudo-equilibrium approximation.

$$I_{\mathrm{TL}} \propto \exp\left(\frac{-E}{\mathrm{k}T}\right) \tag{1}$$

It is assumed that the s value will remain constant and that there will be no overlap of glow peaks. The Arrhenius plot of ln(I) versus 1/T should produce a straight line (Topaksu & Yazıcı, 2007; Chen & McKeever, 1997; Correcher, et al., 2008); from its slope (i.e. $-E_a/k$), E_a can be calculated. However, due to the existence of the complex maximum at 225 ^{o}C, it is not possible to establish the frequency factor (s) using the IR approach in this study.

Various Heating Rate Method

Another well-known method to determine the kinetic parameters (both E_a and s) is VHR method which relies on varying the HR (β) for each successive measurement. According to the equation 2; a plot based on T_m (maximum temperature value that TL intensity reached) with corresponding to HR is used to estimate the trap depth and frequency factor:

$$\ln\left(\frac{T_{\mathrm{m}}^{2}}{\beta}\right) = \ln\left(\frac{E}{s\mathrm{k}}\right) + \frac{E}{\mathrm{k}T_{\mathrm{m}}} \tag{2}$$

The Arrhenius plot of $\ln\left(\frac{T_m^2}{\beta}\right)$ against $\left(\frac{1}{kT_m}\right)$ results in a straight line with the slope is equal to E and the intercept is equal to $\ln\left(\frac{E}{sk}\right)$ (Joseph Daniel, et al., 2017).

<u>CGCD Method</u>

TL glow curves were examined using the CGCD analysis (Benavente, et al., 2019) based on Equation 3, assuming first-order kinetics with respect to the continuous trap distribution approach (considering results from T_{max}-T_{stop} experiment) using a Gaussian function, in accordance with previous work by Balci-Yegen (Balci-Yegen, et al., 2018).

$$n_{\mathrm{Gauss}}(E) = \frac{n_0}{\sqrt{2\pi\sigma^2}} \cdot \mathrm{e}^{-(E_0-E)^2 / 2\cdot\sigma^2} \tag{3}$$

Using a linear combination of peaks and a Levenberg-Marquardt (Horowitz & Yossian, 1995) to minimize the X^2 function (Equation 4), this software permits the optimal fitting of the TL glow curve.

$$\chi^2 = \sum_{\mathrm{i}} \left(I_{\mathrm{Exp}}(T_{\mathrm{i}}) - \sum_{\mathrm{j}=1}^{N_{\mathrm{peaks}}} \mathrm{I}_{\mathrm{Max}} \cdot {}^{\mathrm{Gaus}}F(E_0, T_{\mathrm{Max}}, \sigma; T_{\mathrm{i}}) \right)^2 \tag{4}$$

4. RESULTS AND DISCUSSION

4.1. Results of Chemical and Spectral Analysis and Discussion

Tridymite, a polymorph of quartz, has been extensively investigated using various scientific techniques to uncover its properties and characteristics. XRD analysis has provided valuable insights into tridymite's crystallographic structure, including lattice parameters, unit cell symmetry, and crystal orientation. Additionally, it has allowed for the identification of defects, quantification of phase abundance, and examination of the influence of temperature and pressure on tridymite's stability. ESEM-EDS imaging has provided a unique capability to study tridymite's surface features at high magnification and perform elemental analysis, aiding in the understanding of microstructure, grain boundaries, surface defects, and potential relationships with other minerals. Compositional analysis using EDS has further contributed by revealing the distribution and concentration of elements within tridymite, facilitating the identification of impurities and offering insights into geological connections. EPMA has complemented EDS analysis by providing higher spatial resolution quantitative elemental analysis, enabling the examination of major, minor, and trace elements within tridymite samples. This technique has allowed for precise determination of tridymite's chemical composition, revealing compositional changes and providing valuable information on formation processes and geological significance. Raman spectroscopy has served as a powerful tool for studying the vibrational properties and phase identification of tridymite, with the scattered light's Raman spectrum uncovering characteristic vibrational modes, confirming the mineral's identity, and providing information on crystal properties, polymorphic transitions, and structural disorders. NMR spectroscopy, on the other hand, has delved into tridymite's molecular structure and dynamics, offering insights into chemical bonding, coordination, and local environments by analyzing the interactions of atomic nuclei with an external magnetic field. This technique has shed light on atom mobility and their interactions with neighboring species, thus revealing tridymite's behavior under different conditions. EPR spectroscopy has been employed to investigate the presence of unpaired electrons and paramagnetic defects in tridymite. By subjecting the mineral to a magnetic field and measuring the absorption or emission of electromagnetic radiation, EPR spectroscopy has provided valuable information on the electronic structure, magnetic properties, and defects within tridymite. It has proven particularly useful for identifying and characterizing both external and internal defects, as well as radiation-induced effects. Luminescence techniques, including CL, PL, and TL, have offered significant insights into the luminescent properties and electronic structure of tridymite. CL analysis involves exciting tridymite with high-energy electrons and studying emission patterns, thus revealing luminescent centers, defect-related emissions, and energy band structure. PL measurements, on the other hand, have focused on optical excitation of the mineral to examine emission spectra and energy band structures. TL analysis, utilizing controlled heating, measures the release of stored energy as light, providing insights into trapped and released charge carriers and the thermal history of tridymite. Collectively, these scientific techniques have played a pivotal role in advancing our understanding of tridymite, providing comprehensive insights into its structure, composition, properties, and behavior under diverse conditions.

4.1.1. Thermal X-Ray Diffraction

The obtained T-XRD patterns, depicted in Figure 4.1, exhibit a monoclinic symmetry at RT according to the RRUFF ID: R090042.9. Comparative analysis with the XRD card files of the Joint Committee on Powder Diffraction Standards confirms the concordance of the observed patterns with the sample employed in the present study. The transition between the supergroup-subgroup phases mentioned in the introduction is found to be nearly structurally unchanged and reversible, as evident from the first and last diffractograms corresponding to the initial RT and final RT, respectively.

The diffractograms also reveal two distinct variations: (i) a slight shift towards higher degrees (21.5-22° 2θ) with increasing temperature and (ii) a noteworthy change at 27.5° 2θ, characterized by the disappearance of peaks associated with the (204) and (321) planes, which are observed between temperatures approximately ranging from 125 to 200°C. These observed variations in the diffractograms can be linked to the transitions from a hexagonal to orthorhombic and finally to monoclinic metrics as the temperature decreases from 220 to 150°C. These transitions are classified as incommensurately modulated phase changes, consistent with the findings reported by literature (Graetsch, 2001; Balci, et al., 2022).

Furthermore, aforementioned slight shifts and absence of the signal in the diffraction pattern with the temperature change could be due to changes in grain size and variations in lattice parameters.

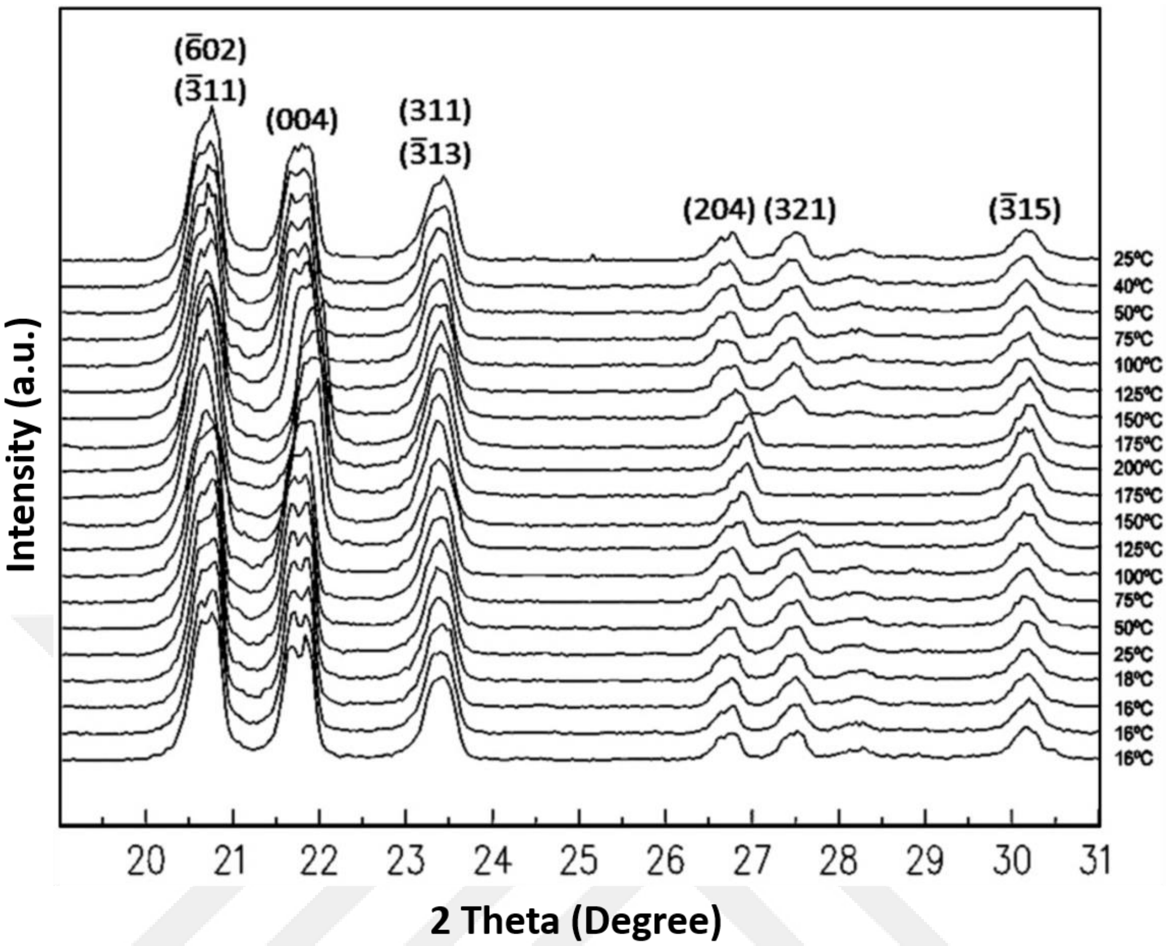

Figure 4.1. XRD profile performed at different temperatures for Tridymite (from RT to 200 ^{o}C and vice versa.)

4.1.2. Environmental Scanning Electron Microscope - Energy Dispersive X-ray Spectroscopy

In order to examine the surface morphology of the natural tridymite mineral and to determine the particle sizes, high resolution ESEM images were obtained at 25-27 kV acceleration voltage. Images of the ESEM results obtained from different regions of the samples and obtained at different magnifications are given in Figure 4.2.a-d.

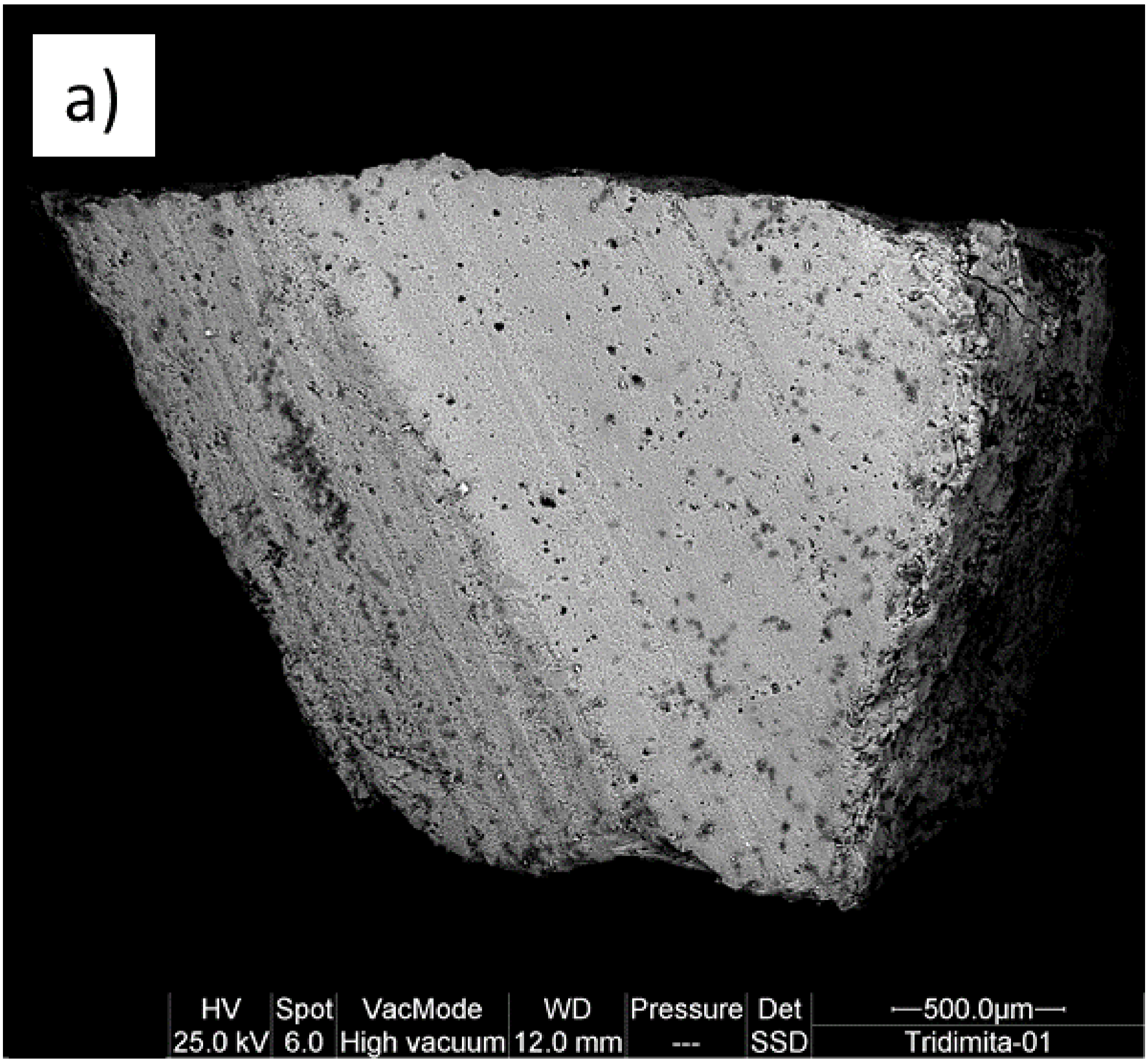
a)
HV
25.0 kV
Spot
6.0
VacMode
High vacuum
WD
12.0 mm
Pressure

Det
SSD
500.0µm
Tridimita-01

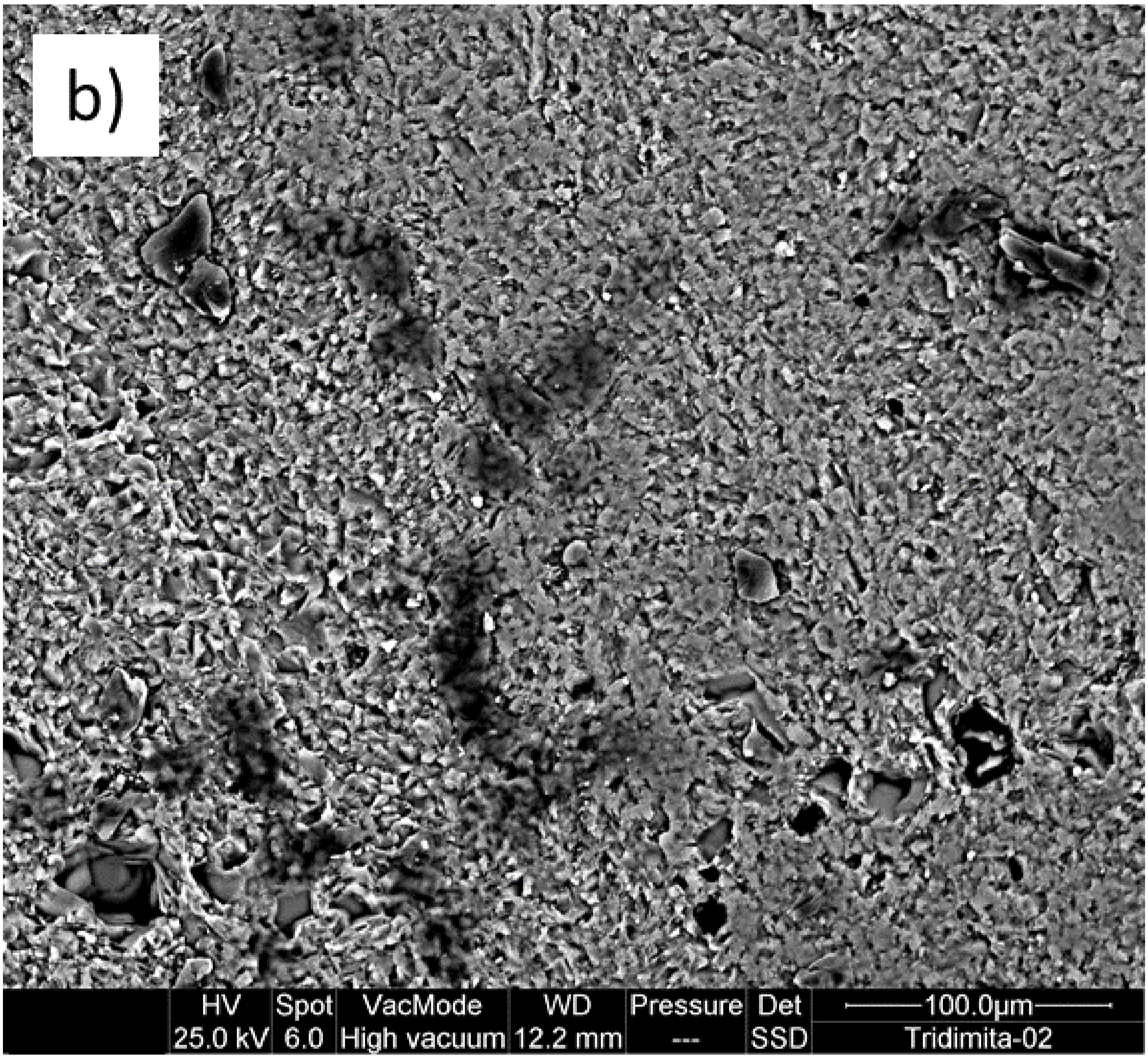
b)
HV
Spot
VacMode
WD
Pressure
Det
100.0µm
25.0 kV
6.0
High vacuum
12.2 mm

SSD
Tridimita-02

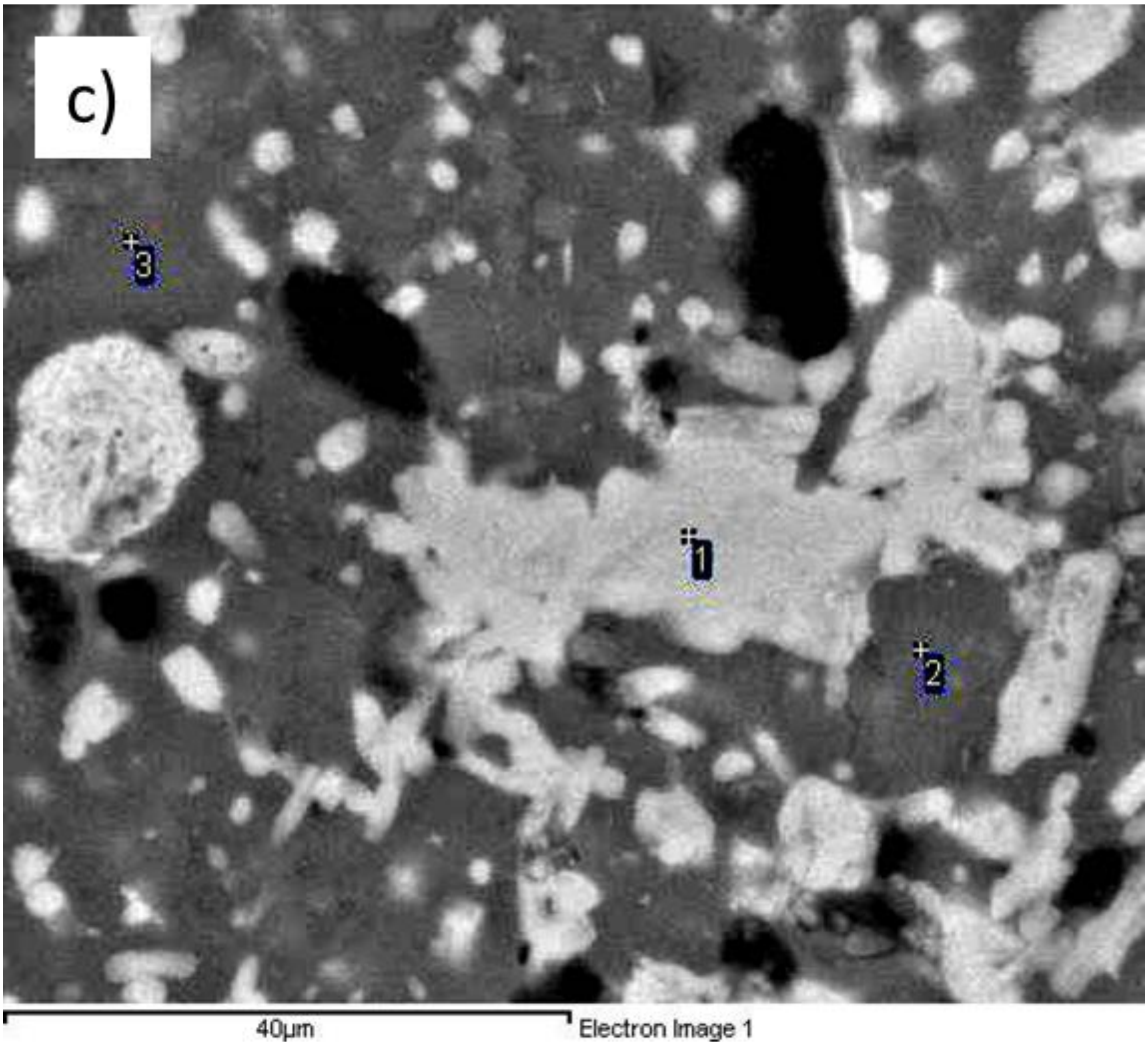
c)
3
1
2
40µm
Electron Image 1

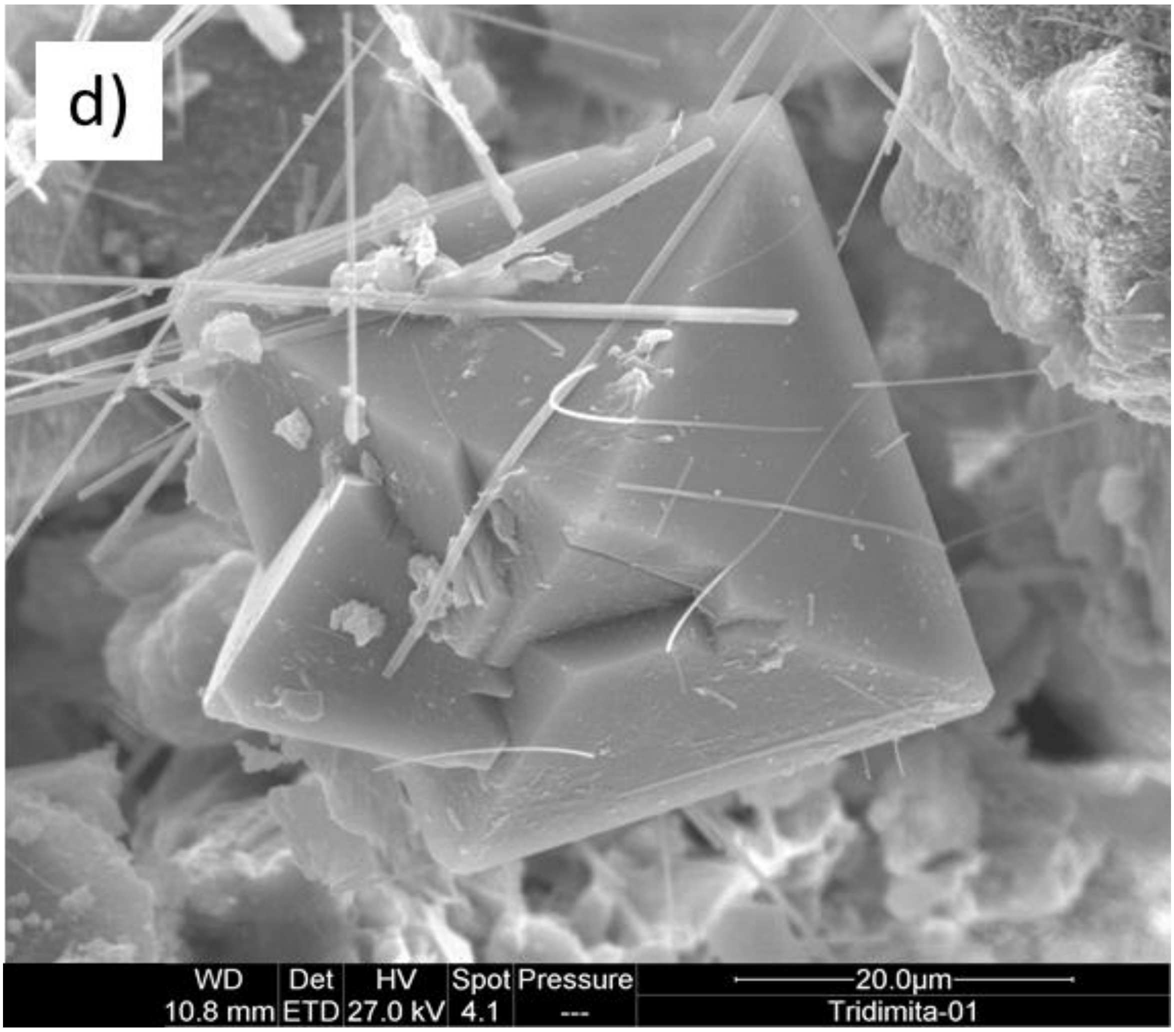

Figure 4.2. a-d ESEM images of the samples.

Examining the ESEM photograph of the sample shown in Figure 4.2.a demonstrates that the particles of different sizes are distributed in the form of clusters and that, as a result of this clustering, the particles exhibit an inhomogeneous particle distribution.

Analyzing the ESEM photograph of the example in Figure 4.2.b and Figure 4.2.c reveals that there are significant gaps between the particles. Additionally, it is observed that some regions contain both small and large particles.

The ESEM image of the sample in the range of 20 µm in Figure 4.2.d clearly displays crystalline structure as triangular prisms and slim-long sticks oriented in all directions, and exhibits aforementioned disparate particle distribution.

The EDS analysis that correspond to the 3 spots in Figure 4.2.c were presented in the graphs in Figure 4.3. As it was expected that the samples do not consist of pure crystalline silica, i.e., spot-1 indicate that “this spot of the sample is para-wollastonike-like tridymite” due to consisting of Ca as well as Si by means of weight (O: shared by Ca and Si). This spot also includes components such as Al, Fe, O. Spots 2 and 3 (Figure 4.2.c) exhibit notable Ca concentrations, but not as much as Spot 1. In addition, these spots contain Al and O, but no Fe. Also, spot 2 has minimal sodium content, unlike others. All these contents are given in Table 4.1 in proportion of weight.

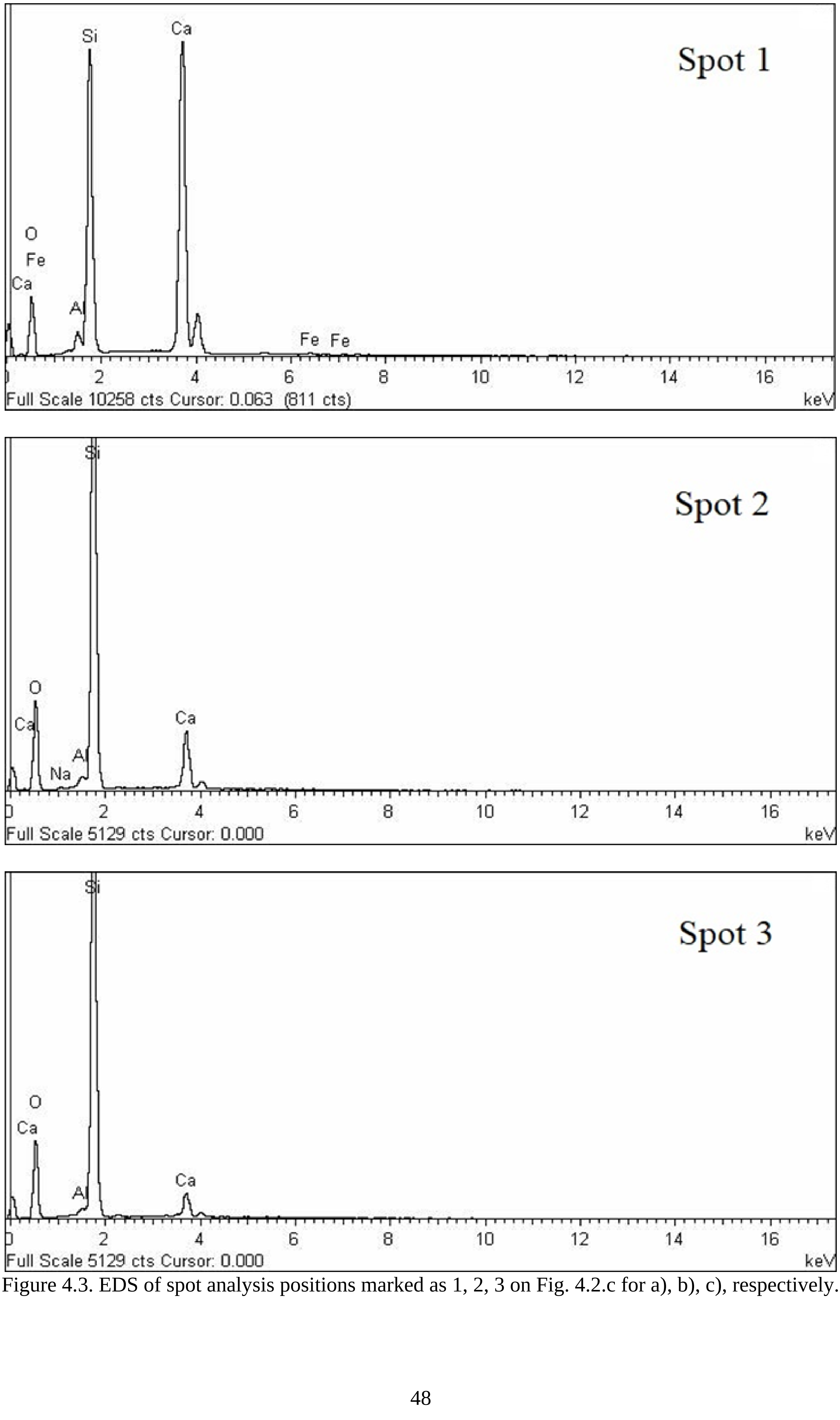

Figure 4.3. EDS of spot analysis positions marked as 1, 2, 3 on Fig. 4.2.c for a), b), c), respectively.

Table 4.1. Chemical composition by weight percentage of tridymite spot analysis positions marked as 1, 2, and 3 on Fig. 4.2.c.

Spot	Na	Al	Si	Ca	Fe	O	Total
1	-	1.83	25.99	28.96	0.33	42.89	100
2	0.43	0.89	41.49	6.42	-	50.77	100
3	-	0.63	44.06	3.25	-	52.06	100

4.1.3. Electron Probe Micro Analysis

The bulk chemical composition of the samples carried out by means of EMPA is shown in Table 4.2 as weight percent. The results of the examination conducted on nine distinct locations of tridymite indicate that the weight proportion of SiO_2 exhibits a range of 86.36 - 98.99 %. Certain regions have been found to contain trace amounts of cations such as Al, Fe, Mn, Mg, Ca, Na, K, Ti, Ni, Cr, and P, in addition to the elements F and Cl, while other cations remain below the minimum detectable threshold.

Table 4.2. Chemical composition of tridymite performed by EPMA.

Spot No	1	2	3	4	5	6	7	8	9
SiO_2	98.99	96.27	97.49	97.10	95.46	95.855	94.24	88.46	86.36
Al_2O_3	0.52	2.13	0.805	1.129	0.779	0.522	1.16	1.581	1.11
FeO	0.006	0.05	0.03	0	0.046	0	0	0.04	1.08
MnO	0	0.06	0.007	0	0.014	0.011	0	0	0
MgO	0.001	0.01	0.013	0.014	0.023	0.122	0	0	4.82
CaO	0.045	0.448	0.397	0.592	0.264	0.404	4.52	8.982	5.41
Na_2O	0.203	0.497	0.641	0.601	0.225	0.192	0	0.586	0.49
K_2O	0.106	0.420	0.293	0.425	0.126	0.071	0	0	0
TiO_2	0.014	0.007	0.012	0	0.050	0.052	0	0	0.27
NiO	0	0	0	0	0.015	0.024	0	0	0
Cr_2O_3	0	0	0.016	0	0.018	0	0	0	0.43
P_2O_5	0	0.074	0	0.038	0.101	0.170	0	0	0
F	0	0	0.004	0	0	0.039	0	0	0
Cl	0	0	0	0	0.006	0	0	0	0
Total	99.885	99.966	99.708	99.899	97.130	97.446	99.92	99.649	99.97

4.1.4. Raman Spectroscopy

The Raman spectrum of the sample exhibits distinct bands at specific wavenumbers, indicating the vibrational modes of the molecules present. Based on the experimental results shown in Figure 4.4, the spectrum can be analyzed as follows:

- The Raman bands appear at ca. 155 cm^{-1}, 220 cm^{-1}, 320 cm^{-1}, 370 cm^{-1}, 410 cm^{-1}, 445 cm^{-1}, 800 cm^{-1}, and 1100 cm^{-1}. These values represent the wavenumbers at which the Raman scattering occurs.
- The highest peak is observed at around 370 cm^{-1}. This peak signifies the strongest Raman scattering intensity and is likely associated with a prominent molecular vibration.
- Following the highest peak, there is a peak at around 320 cm^{-1}. Based on theoretical calculations, it has been suggested that within the frequency range of 300-350 cm^{-1}, the predominant normal modes primarily involve the bending vibrations of Si-O-Si in the ring atoms (Ostrooumov, 2007).
- The peaks around 410 cm^{-1} and 445 $cm^{-1}$are close to each other. This indicates the presence of multiple molecular vibrations that are closely spaced.
- The peak at approximately 220 cm^{-1} is distinct and sharp, similar to the other peaks. It appears to have a left shoulder at 155 cm^{-1}. This suggests that the molecular vibration associated with the 220 cm^{-1} peak may have additional vibrational modes or coupling with vibrations occurring around 155 cm^{-1}.
- The peaks at ca. 800 cm^{-1} and 1100 cm^{-1} have quite small intensity relative to others, yet still a characterization sign for tridymite.

These findings exhibit a strong resemblance to the Raman spectroscopic results previously reported in the literature for the MC and, to a lesser extent, the MX-1 polycrystalline fragments (Kanzaki, 2020). Tridymite is commonly found in nature, primarily within the PO group, exhibiting a diverse range of unit cells. However, MC tridymite is typically associated with meteoritic and synthetic samples (Hirose, et al., 2005). Notably, tridymite originating from Lanzarote, Canary Island, might represent an exceptional case, deviating from the typical modification patterns observed in tridymite from other sources (for comparison, see Figure 2.1).

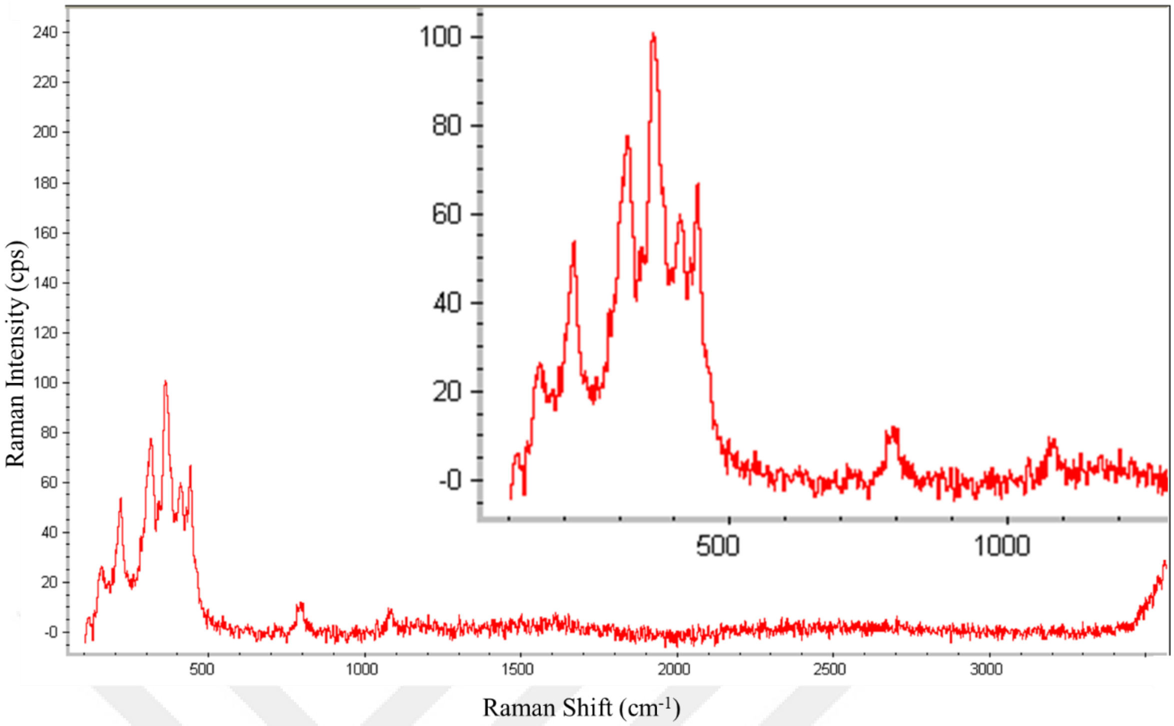

Figure 4.4. Raman Spectroscopy of tridymite.

The spectral analysis conducted, spanning the range of up to 3600 cm^{-1}, serves as empirical evidence to distinguish the studied sample from opal. This broader spectral scale enables the identification of distinct vibrational modes and characteristic features, thereby establishing the discernible differences between the two materials (Ostrooumov, 2007).

4.1.5. Nuclear Magnetic Resonance

The presence of a broad peak in the 29Si MAS NMR spectra of tridymite at around 110 ppm (start arising from at around 75 ppm to 150 ppm) suggests that there is some heterogeneity in the local environments of silicon atoms within the tridymite crystal lattice. These results resemble the peaks previously observed in different phases of tridymite (at various temperature values) (Xiao, et al., 1993; Xiao, et al., 1995). In NMR spectroscopy, a broadening of the peak indicates that the silicon nuclei are experiencing a range of different chemical environments, likely due to variations in neighboring atoms or functional groups surrounding the silicon sites. This can arise from defects, impurities, or structural disorder within the crystal lattice. The broadening of the peak might also be an indication of different polymorphic forms of tridymite present in the sample, each with its own distinct arrangement of silicon atoms (Kitchin, et al., 1996). This idea is well correlated to the T-XRD results, which suggest existence of different phases of tridymite, discussed in section 4.1.1 (Balci, et al., 2022).

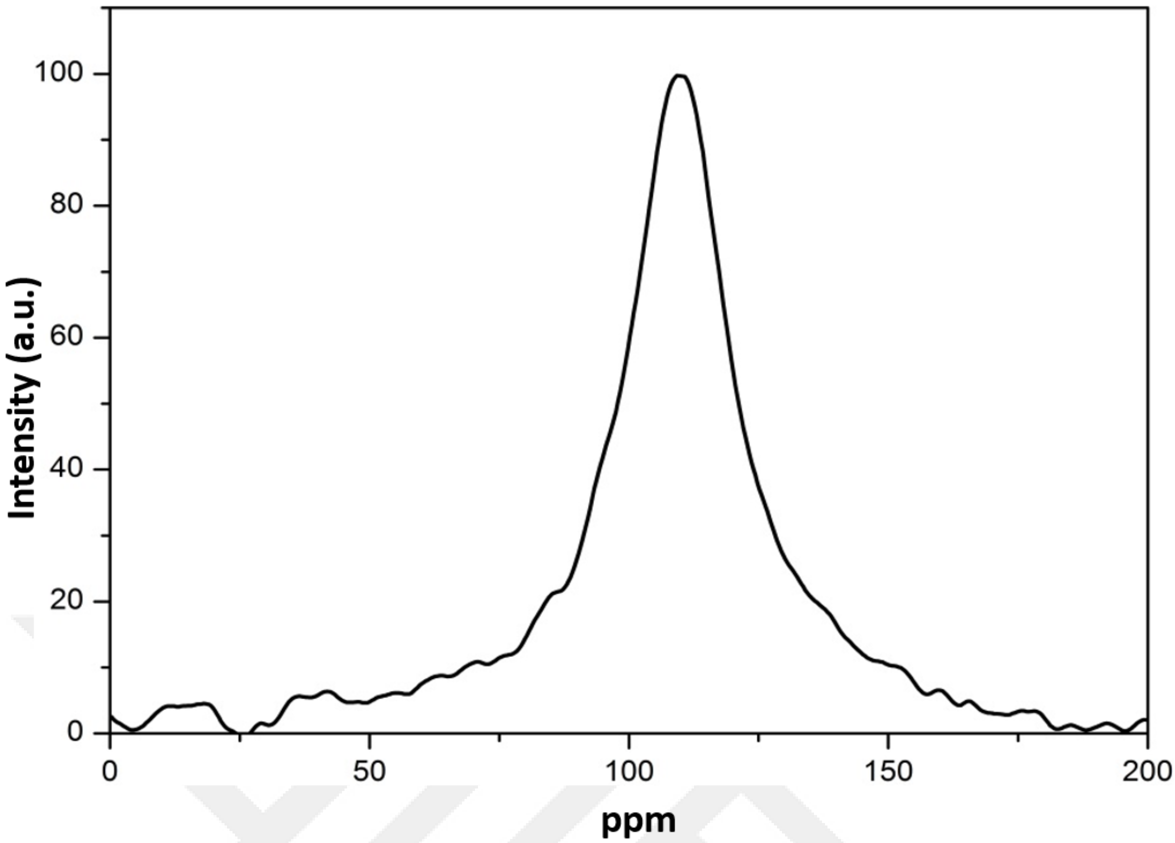

Figure 4.5. ^{29}Si MAS NMR spectra of tridymite at RT.

4.1.6. Electron Paramagnetic Resonance

The presence of Fe and Mn impurities in the structure is unequivocal, as evidenced by the observations depicted in Figure 4.6 and 4.7 (Ikeya, 1993).

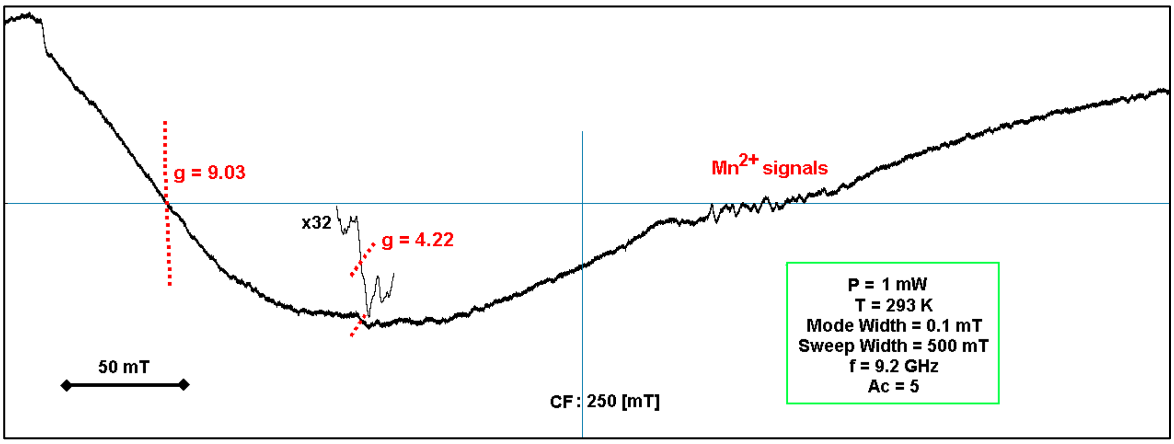

Figure 4.6. ESR spectra of Tridymite at 293 K with 500 mT sweep width.

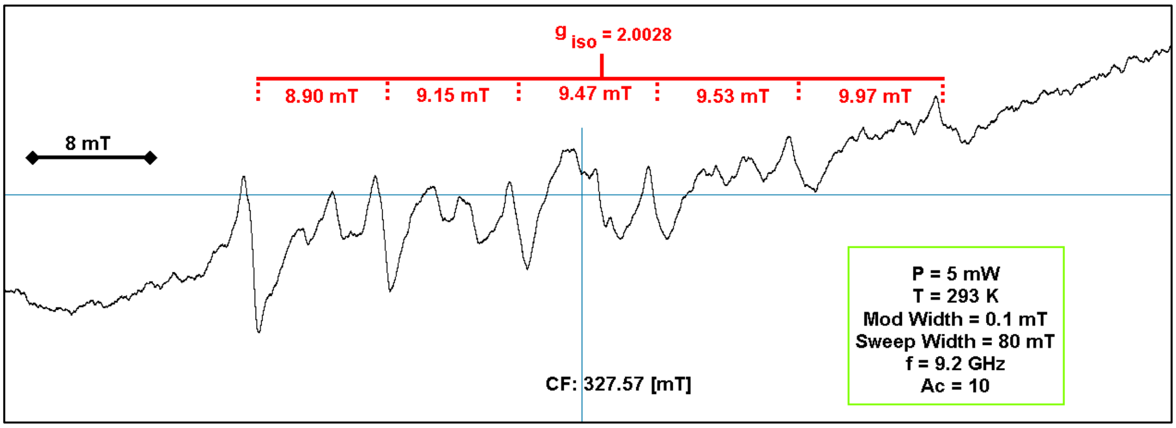

Figure 4.7. Mn^{2+} signals at ESR spectra of Tridymite powder recorded at 293 K.

Notably, Figure 4.8 and 4.9 (zoom of Figure 4.8 in order to see E' center clearly) reveal the presence of the E' center within the structure. The identification of this center is of utmost significance, as it suggests the potential applicability of this mineral in dosimetry and dating studies (Ikeya, 1993).

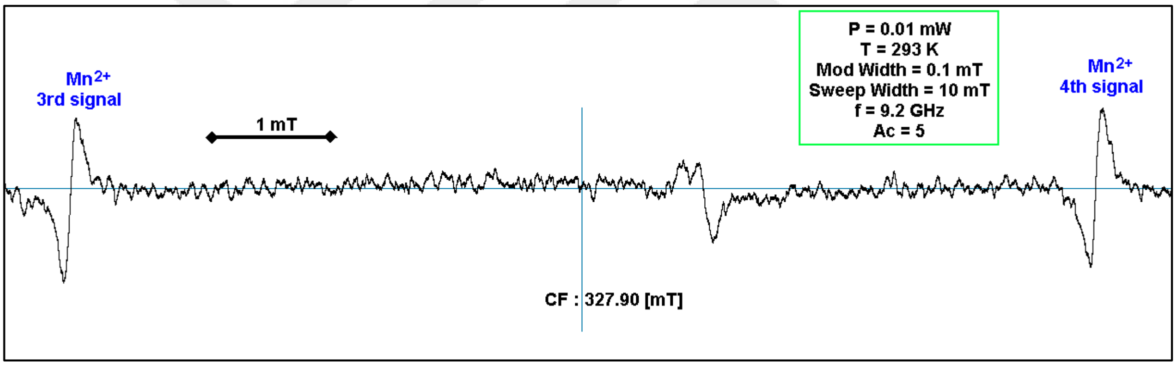

Figure 4.8. E' center

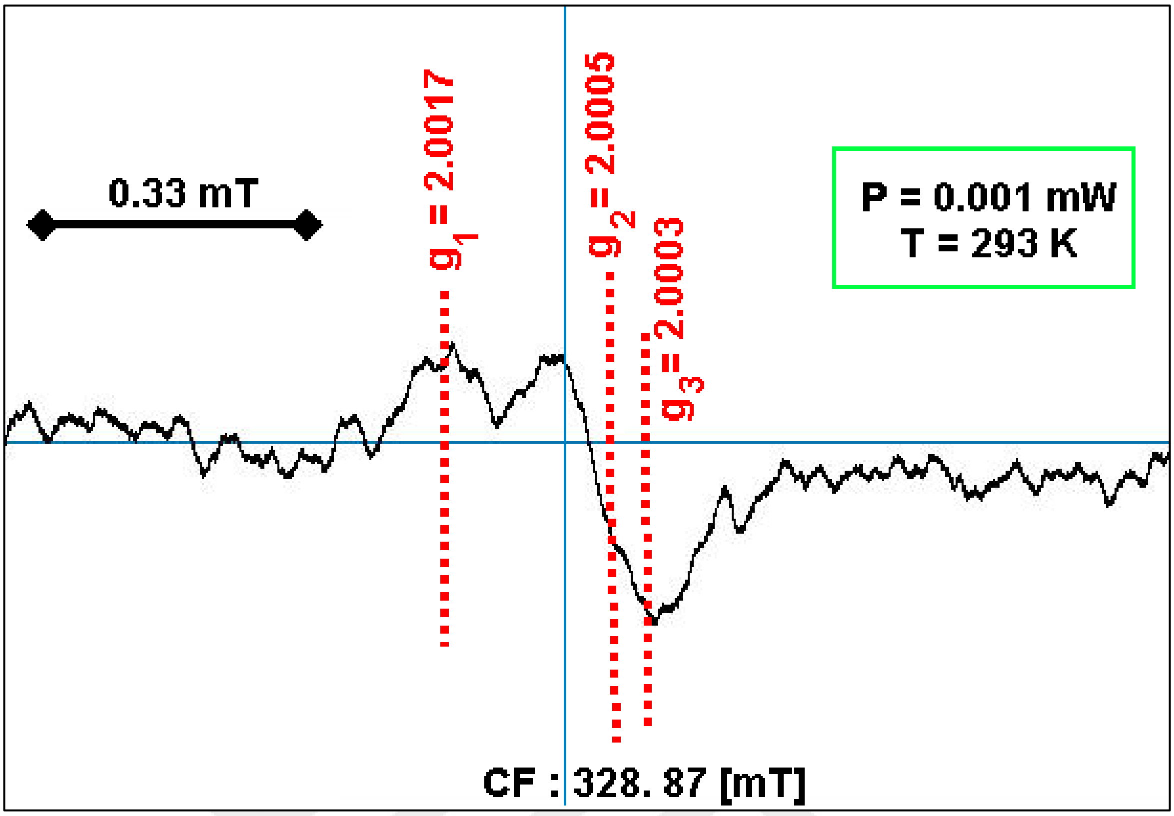

Figure 4.9. E' center (zoom)

Low Temperature Study: Low-temperature studies were conducted in the temperature range from room temperature (RT) down to -150 °C and subsequently back to RT in increments of 20-30 °C, encompassing a total of 43 measurements. The objective was to investigate the effects of temperature and power variations. However, due to the lack of meaningful trends, it was deemed unnecessary to create comparative graphs for different temperatures or powers. In the presence of Al impurities within the structure, their signals, if present, would correspond to the forbidden transition zone of Standard-Mn impurity signals. Consequently, determining the existence of Al signals at low temperatures proved challenging. Notably, in the spectrum pattern obtained at a microwave power of 10 mW and low temperature, an increase in the intensity of the broad signal within the magnetic field range associated with Al and Mn impurity signals was observed. The behavior of Standard-Mn signals at low temperatures was investigated to discern whether this effect was attributed to Mn or Al impurities. It was observed that the Standard-Mn signals appeared weaker at low temperatures. Consequently, the amplified magnitude of the broad signal between the two Standard-Mn signals could potentially be attributed to the presence of Al impurity; however, further evidence is required to substantiate this claim. The clarification of this matter, which is not addressed in this thesis, can potentially be achieved through irradiation experiments. Furthermore, a signal at g = 2.0027 was observed, which exhibited an increase at high powers. This signal potentially belongs to the forbidden transition of the Standard-Mn, distinguishing it from other radicals commonly found in quartz samples.

High Temperature Study: A high-temperature study was conducted, ranging from room temperature (RT) to 150 °C (and back to RT) in increments of 20-30 °C at various power levels. A total of 57 measurements were performed as part of the high-temperature study, and it was determined that no meaningful graph could be constructed to compare the variations in temperature or power. The signal observed at g = 2.0027, which was initially observed at low temperatures, was also observed at a temperature of +150 °C. Furthermore, it was found that the intensity of this signal increased at high power levels. This signal exhibits characteristics that are distinct from other radicals commonly found in quartz, suggesting that it may be associated with the forbidden transition of the Standard-Mn.

Performing a kinetic study involving varying temperature and power conditions can pose risks and may yield limited information. However, conducting an investigation on the irradiated sample provides a definitive means to assess the presence of the Al impurity center and the Ge impurity center within the structure (Figure 4.10). Notably, the absence of an increase in Mn signals upon radiation exposure facilitates the observation of radiation-sensitive signals with greater ease (Figure 4.11).

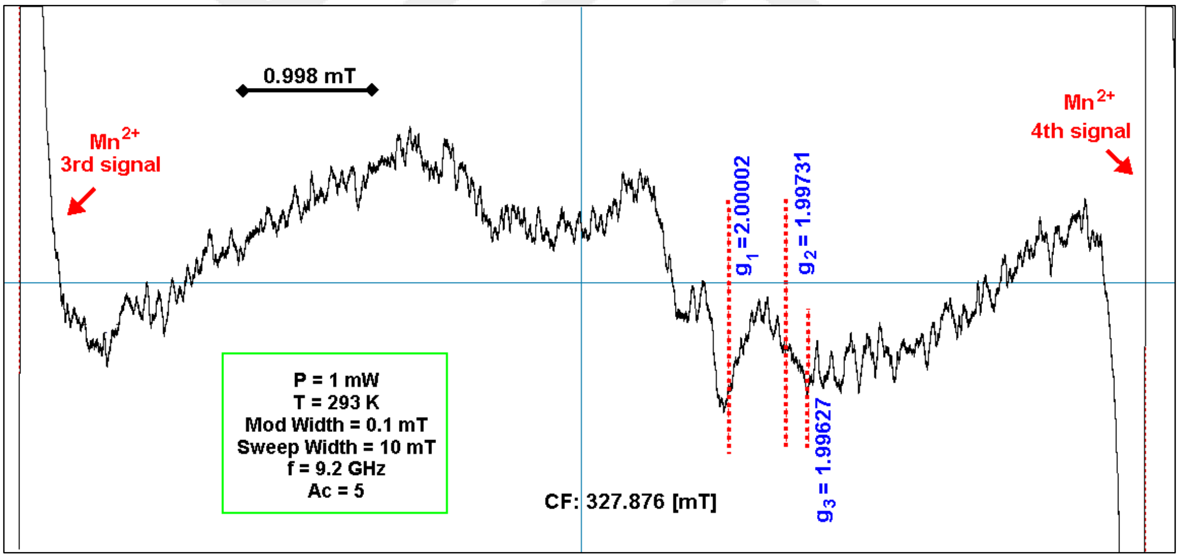

Figure 4.10. Could be Ge center, it needs to be irradiated to find out.

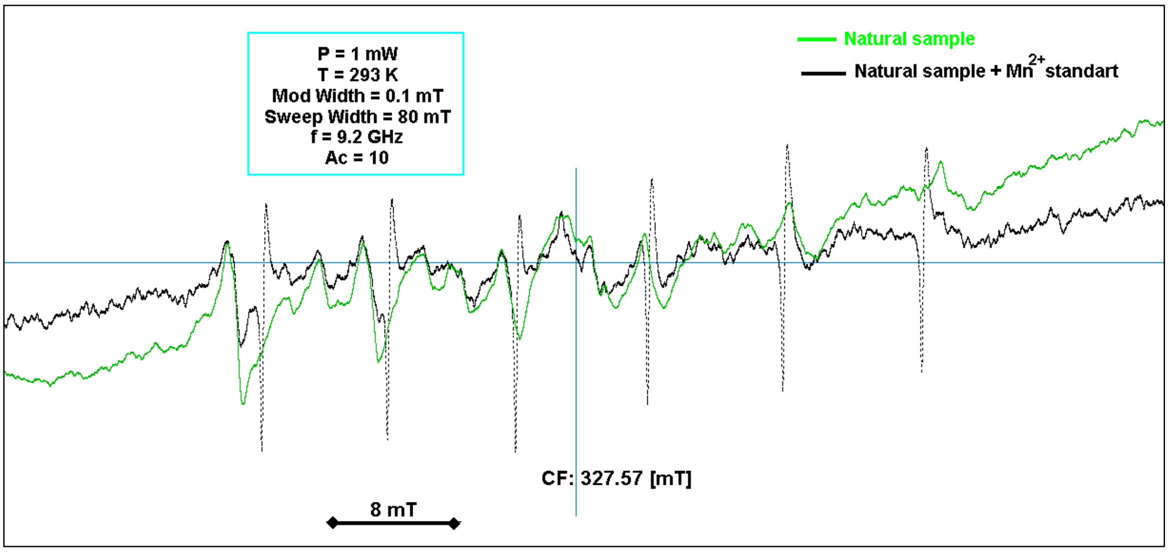

Figure 4.11. Comparison between Mn impurity signals and standard-Mn.

4.2. Results of Luminescence Analysis and Discussion

4.2.1. Cathodoluminescence

By combining CL analysis with EPR measurements, it can be identified and investigated both extrinsic (trace elements) and intrinsic (lattice defects) point defects in minerals, facilitating their detection and comprehensive study (Götze, et al., 2001). Tridymite samples used in this study demonstrate CL in the blue wavelength range of visible light, and commonly exhibit pronounced zoning, which serves as evidence for the sequential crystallization processes occurring during rock formation (Paralı, et al., 2011). In Figure 4.12 demonstrates that the CL spectra of the sample has maxima at about 452.5 nm with a left shoulder at ca. 400 nm. Additionally, an observed peak at 480 nm, in close proximity to 452.5 nm, exhibits a notable sharpness that allows for its clear differentiation from 452.5 nm. The blue luminescence band is typically very broad and consists of component bands that overlap and are associated with various types of centers. One of these could be associated with O-deficient centers (ODCs) (Zamiatina, et al., 2023).

It has been postulated that the observed peak at approximately 450 nm may arise from the recombination events of self-trapped excitons, which are formed through the interaction of irradiation-induced oxygen Frenkel pairs. These pairs are composed of an oxygen vacancy and a peroxy linkage (Si–O–O–Si), representing an intrinsic defect within the material (Paralı, et al., 2011). Furthermore, multiple researchers have proposed that the luminescence observed in blue/green silica stems from the recombination of electron-hole pairs associated with self-trapped excitons occurring at an intrinsic defect, resulting in light emission within the range of approximately 450 to 480 nm. However, altering the defect site through the incorporation of elements such as Ge or O_2 induces a shift in the emission wavelength to around 400 nm (Götze, et al., 2001; Kibar, et al., 2007). Additionally, the peaks observed between 470-500 nm are attributed to impurity defects, specifically GeO_4^{3-}+e and AlO_4^{4-}+e, as suggested by (Gorobets & Rogojine, 2002). This finding aligns with the results obtained from the chemical characterization of the sample discussed in Chapter 4.1, providing further support for the identified impurity defects.

In conclusion, the tridymite samples used in this study showed CL in the blue wavelength range of visible light, which helped the decision to use the Melles-Griot blue filter (FIB002) with the wavelength peaking at 320-480 nm for TL experiments.

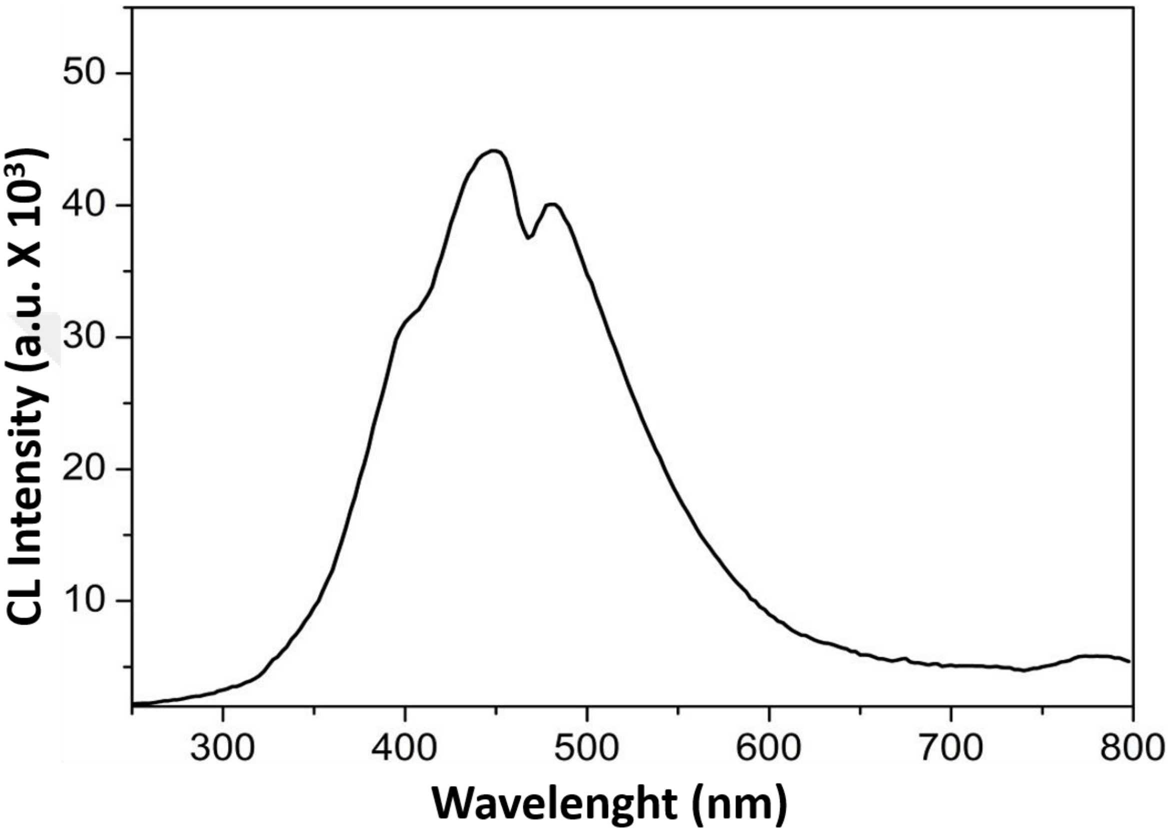

Figure 4.12. CL emission of tridymite samples.

4.2.2. Photoluminescence

The provided impurity composition data and the observed PL peaks at 693 and 694.5 nm in tridymite (Figure 4.13) can be connected in the following ways:

Impurity-Induced Energy Levels: The impurity composition, specifically the presence of different elements such as Na, Al, Ca, Fe, and Si, can introduce energy levels or defect states within the tridymite structure. These energy levels can influence the electronic transitions and result in the observed PL peaks. The specific impurity elements and their concentrations may contribute to the formation of localized states that affect the emission wavelength (Pandey & Chithambo, 2018).

Crystal Structure and Defects: The impurity content and distribution can affect the crystal structure of tridymite, leading to the formation of grain boundaries, strain, or structural defects. These structural features can impact the electronic (energy levels, band structure, and transport properties) and optical properties (interaction of light with the material, including absorption, emission, and scattering processes) of the material, including the emission wavelength observed in the PL spectrum (Yuan, et al., 2023).

Charge transfer and luminescence centers are significant in influencing the emission properties of tridymite. Impurity elements, particularly transition metals such as Fe, Cr, Mn, and Ni, can act as luminescence centers by facilitating charge transfer processes and inducing energy transfer between different states. These transition metal impurities introduce localized energy levels, thereby serving as luminescence centers and impacting the emission peaks observed in the PL spectrum of tridymite. Also non-metal impurities such as F (in which the sample has a very low concentration of it as a result of EPMA analysis) can affect the electronic structure of tridymite and introduce localized states that influence the PL properties. Furthermore, the analysis of CL results enables a comprehensive investigation into the influence of impurity defects, such as GeO_4^{3-}+e and AlO_4^{4-}+e (stated in section results and discussion of CL), on the efficiency of radiative recombination processes responsible for the PL emission of tridymite.

It has been postulated that one of the luminescence peaks at approximately 452.5 nm could be associated with O-deficient centers (ODCs) (in section results and discussion of CL). These ODCs may result from oxygen vacancies or other types of defects in the tridymite lattice, and their recombination events could contribute to the observed PL emission.

On the other hand, certain impurities, specifically transition metal ions like Fe, Mn, Cr, as well as certain rare earth elements, have the ability to introduce non-radiative recombination pathways within tridymite. These impurities can negatively impact the radiative recombination efficiency, leading to a reduction in the intensity of the PL emission. The presence of these impurities disrupts the normal emission processes, causing a quenching effect on the PL properties of tridymite (Yuan, et al., 2023).

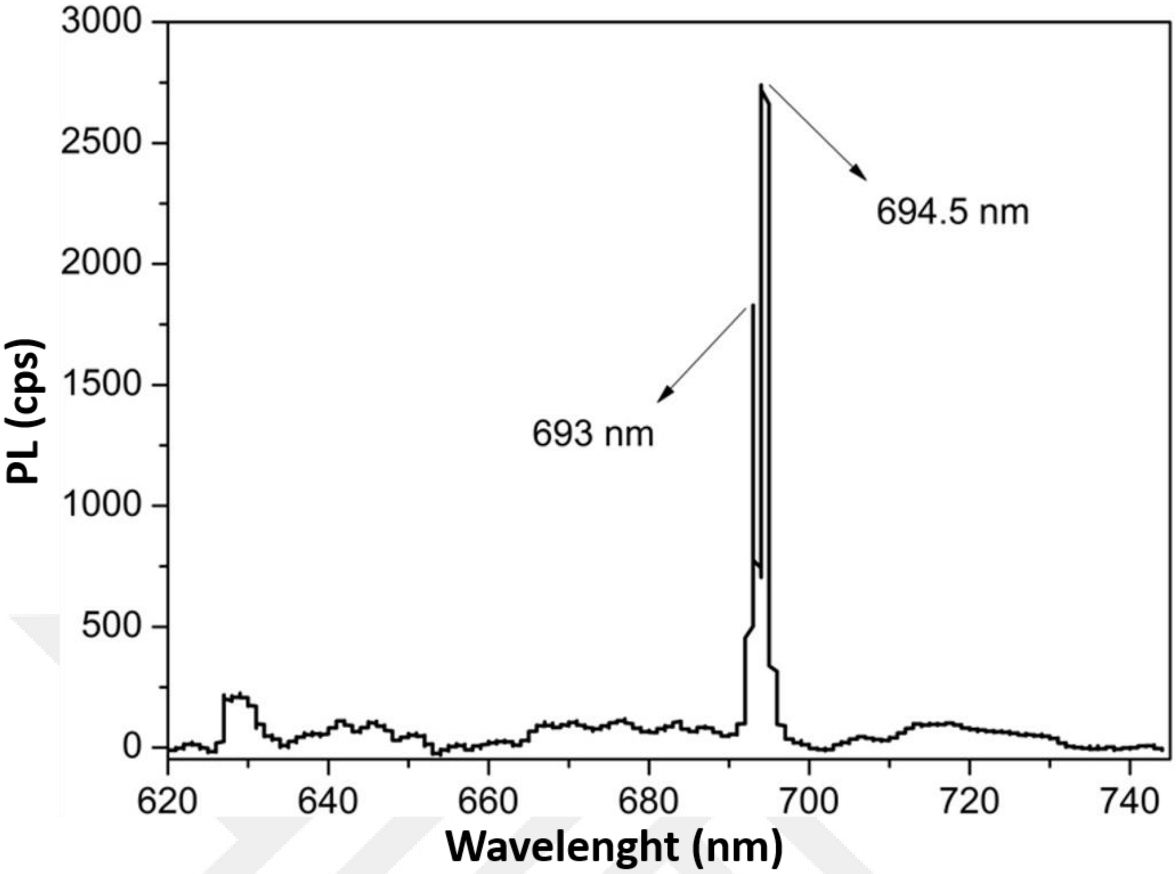

Figure 4.13. PL results of tridymite. 1.782eV for 693nm and 1.775 eV for 694.5nm by using the equation E=h*c/λ

4.2.3. Thermoluminescence

In this section, the results of all TL experiments used to investigate the TL characterization of tridymite were listed and discussed under separate sub-sections.

Natural TL (NTL)

It is assumed that the source of NTL emission is the radiation that tridymite mineral (absorbed from natural radionuclides and cosmic radiation) stored for approximately 300 years as a result of the most recent volcanic eruption, which occurred in Lanzarote, Canary Island, in 1730-1736 (Aparicio, et al., 2006).

Figure 4.14 represents the NTL response of tridymite aliquots, which exhibit two major groups of peak components at about 240 and 310 ^{o}C and two shoulder groups of components at relatively lower intensities at about 180 and 430 ^{o}C. These four maxima could be associated with structural and point defects, and they could be common with quartz. Generally, in NTL emission, as in tridymite samples, the low temperature peaks (below 100 ^{o}C, and in this case, below 150 ^{o}C) are undetectable since they are unstable and fade over a short time.

a) Although tridymite is in different phases for two temperature values, both maxima, which peaked at around 180 and 310 ^oC, respectively, could be due to $[GeO_4]^-$ centers act as electron trapping centers (accepting monovalent cations like H^+, Li^+, and Na^+) (McKeever, 1985).

b) The maximum peaked at about 240 ^oC could be both associated to (i) electron traps caused by $[GeO_4/Li]^o$ centers (Guzzo, et al., 2017), and (ii) the phase transition from H3-T (OS) to H2-T (OC) with the space groups from $P2_1$ ($\alpha\beta0$) to $C222_1$, respectively (Dove, et al., 2000).

(Here H2-T and H3-T represent high temperature phase of tridymite, OC represents C-centered orthorhombic phase, and OS is defined as the modulated form of OC.)

c) The maximum peaked at about 430 ^oC, could be related the oxygen vacancies (act as hole traps) close to Al ions (McKeever, 1985; Correcher, et al., 2009). Furthermore, starting from around that temperature, tridymite is in H1-T (HP) phase with the space group $P6_3/mmc$, until it is in liquid silica form (in which at ca. 1450-1470 ^oC) (Graetsch, 2001).

(Here HP represents high-temperature hexagonal phase of tridymite.)

In addition, it could be concluded that the NTL measurement agrees with the T-XRD results, as both could have common signatures at around 150-200 ^oC.

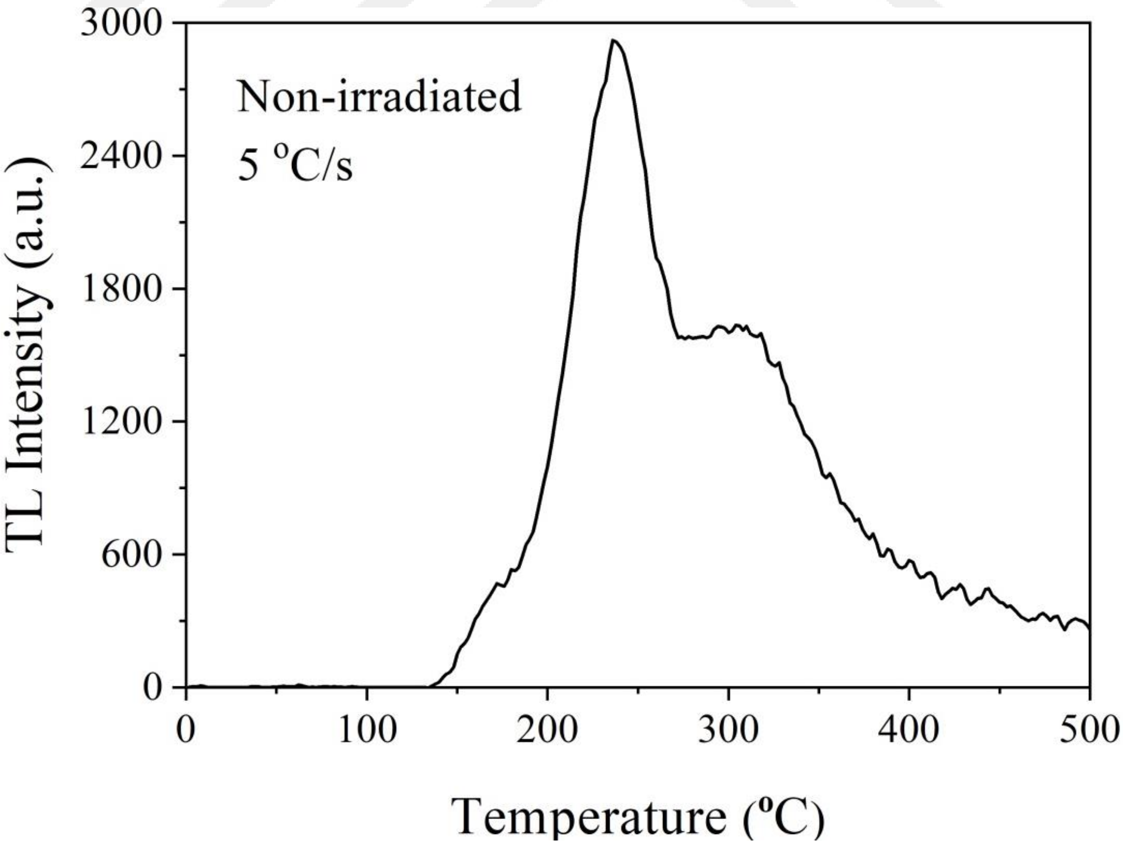

Figure 4.14. TL intensity for non-irradiated natural samples.

Trap distribution characteristics of natural materials are typically complicated and cannot be explained in terms of isolated trapping states. For this reason, the deconvolution process was performed via the CGCD method in order to evaluate the kinetic parameters. Also, comparison between NTL, beta-induced, and UVC-induced TL results will be discussed under the heading of CGCD Analysis.

Reusability

As a result of repeated material use, the structure and distribution of traps could change over time, hence affecting the TL sensitivity. In order to determine whether the glow signal stable, the sample was subjected to multiple cycles of irradiation (1.2 Gy of test dose), and each irradiation followed by a readout up to 500 ^{o}C with a heating rate of 5 Gy/s. Figure 4.15 shows graph of TL intensity versus temperature for 5 cycle, and it is clearly apparent that there is no difference between each measurement in terms of the shape of the whole curve and the intensity, with the exception of a minor variation in the first maximum, which peaks at approximately 93 ^{o}C. This slight variation would be associated with the pre-dose effect that Bailiff developed (Bailiff, 1994). Other researchers have also discussed (and agree with Bailiff) the TL emission peak of quartz at 100 ^{o}C (Oniya, et al., 2015), and it has been found that once quartz-like minerals are heated to around 500–600 ^{o}C (termed the activation temperature), their sensitivity could rise due to the given pre-dose following further thermal treatments.

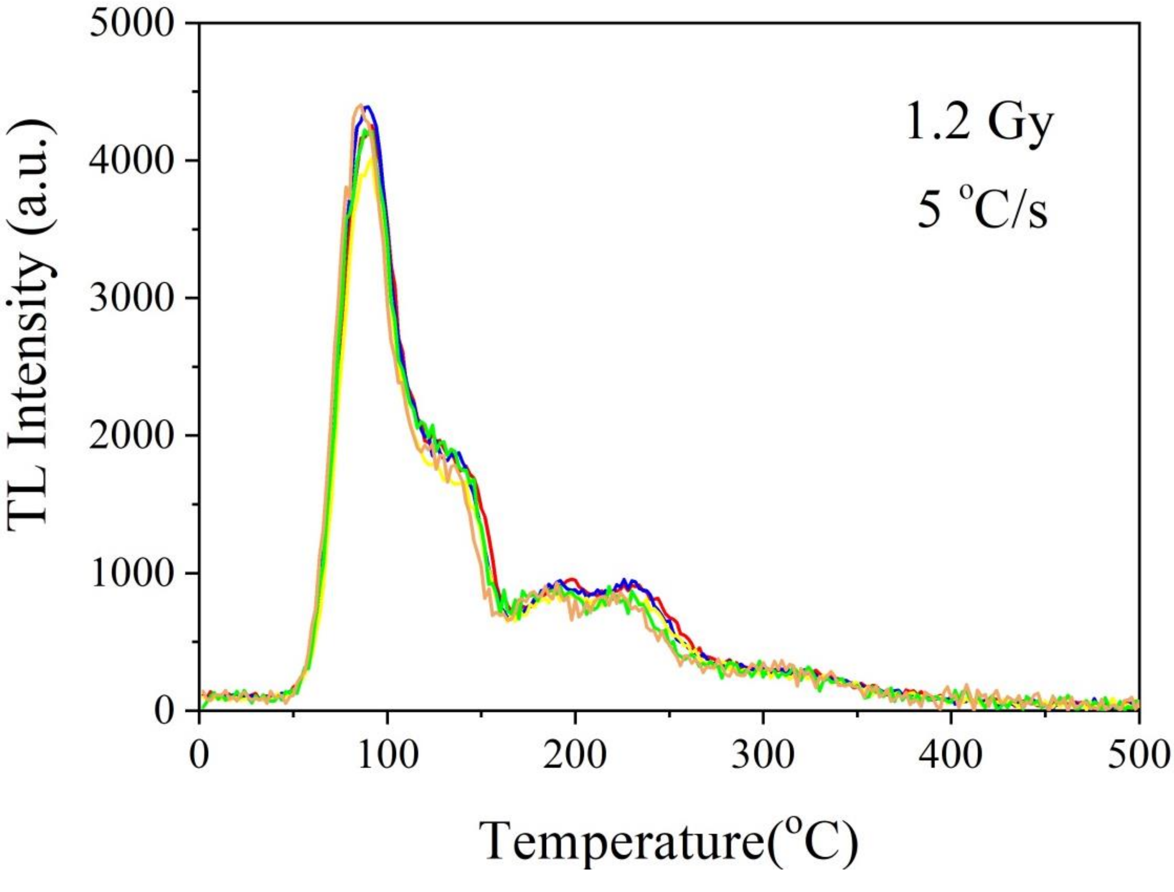

Figure 4.15. Reusability plot of tridymite irradiated by 1.2 Gy of beta with HR value of 5^{o}C/s

In order to examine the reusability results of the sample in further detail, the number of cycles was plotted against the normalized peak area (the total intensity under the plot for each TL measurement). According to Figure 4.16, based on the standard deviation of the five successive measurement, the sample could be measured repeatedly with a variation of less than 5%, with the only exception of the third measurement, which had a 9% departure because of the previously mentioned pre-dose effect.

Consequently, the reusability properties of tridymite are within acceptable limit parameters and also correlate with the results from T-XRD studies since the sample exhibits a consistent thermal response across them (Balci, et al., 2022).

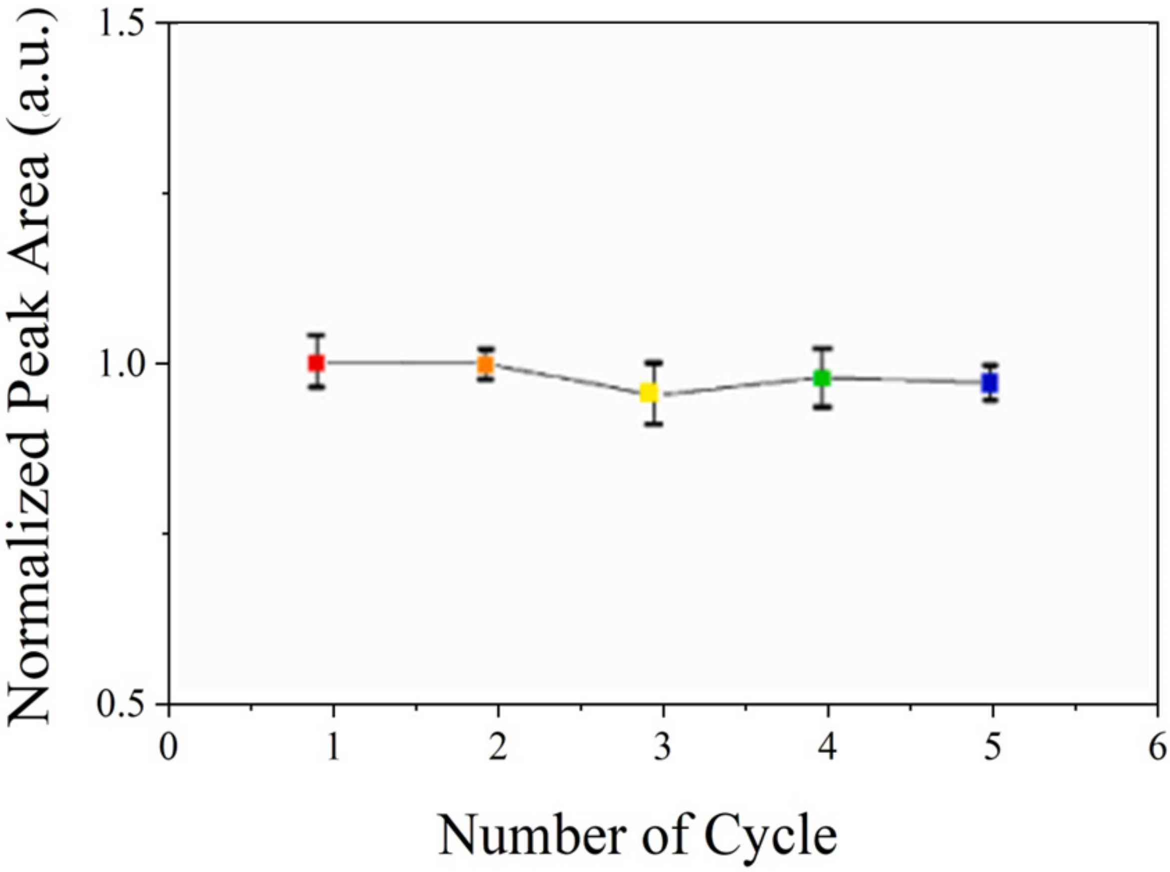

Figure 4.16. Normalized plot of reusability results.

Dose Response

The purpose of examining the effect of a progressive increase in the exposure dose on the TL emission of the studied material is to determine whether there are variations in the luminescent signal within the selected dose range.

Dose Response for beta irradiated samples:

Figure 4.17 displays the TL dose response of tridymite to beta irradiation. All responses to different doses exhibit equal structure and maxima, demonstrating linearity. All glow curves feature five maxima at temperatures of around 95, 130, 200, 230, and 320 °C, in which analyzed in detailed below:

a) The first maximum; with the strongest luminescence emission and the lowest temperature (at about 95 °C) could be attributable to oxygen vacancies such like E' centers, as others have proposed (McKeever, 1985; Correcher, et al., 2009).
b) The glow emission at approximately 130 °C might be attributed to the phase transformation between 70 and 475 °C (Dove, et al., 2000).
c) The maxima at approximately 200 and 230 °C have comparable emissions and are near together. These maxima might be associated with another phase transition in the lattice structure due to the metal's loss of valance, which can be recovered by the addition of other metal atoms to the structure (Balci-Yegen, et al., 2018). This idea was corroborated by another study that has a hypothesis that the TL sensitivity around 200-300 ^{o}C is caused by the presence of $[AlO_4]^o$ centers, which act as hole-like centers (Kitis, et al., 1990).
d) The wide maximum, which reached its highest point at around 320 ^{o}C, has the lowest intensity of all of them. This could be associated to electron traps caused by oxygen vacancy, i.e., E'_1 center, which is defined as a kind of distortion on the lattice structure that allows non-equivalent Si atoms to have an unpaired electron (McKeever, 1985; Guzzo, et al., 2017).

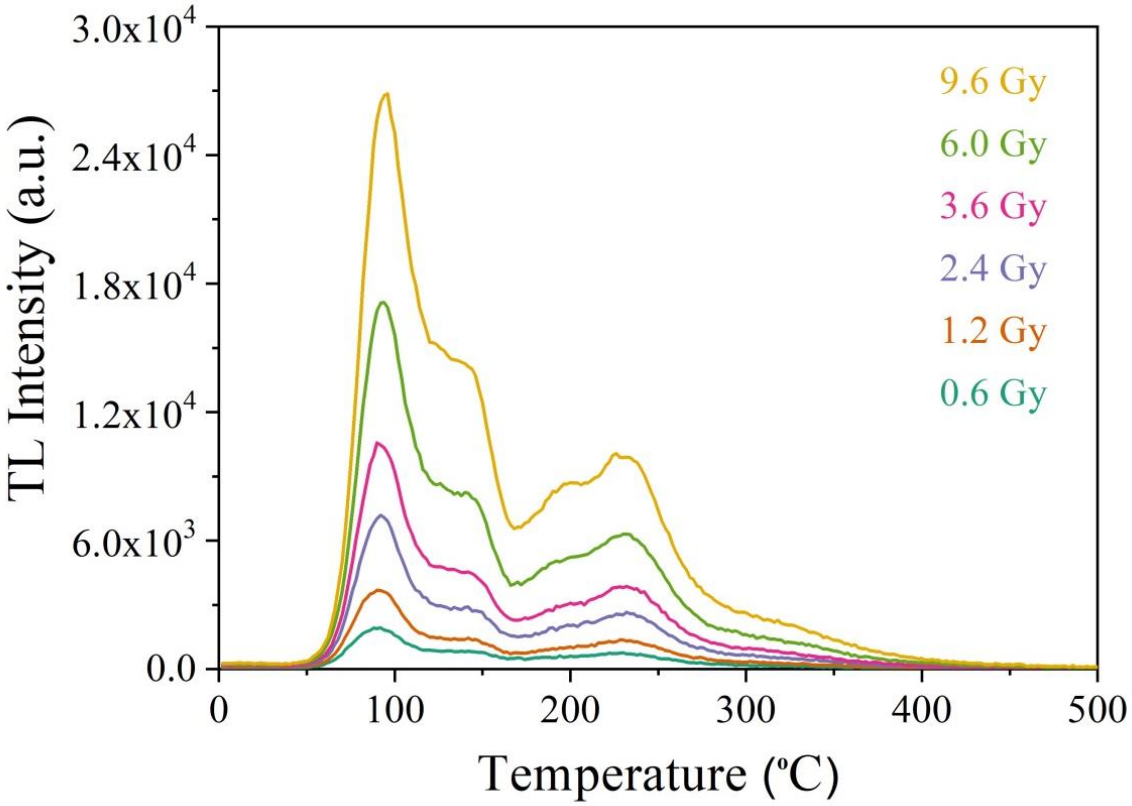

Figure 4.17. The plot for TL dose response of tridymite to beta irradiation with HR of 5 ^{o}C/s.

As observed in Figure 4.18, the plot of the total intensity of the entire glow curve versus the irradiation dose clearly confirms that the dose response is linear, with a quite reasonable regression coefficient of 0.9997 (Balci, et al., 2022).

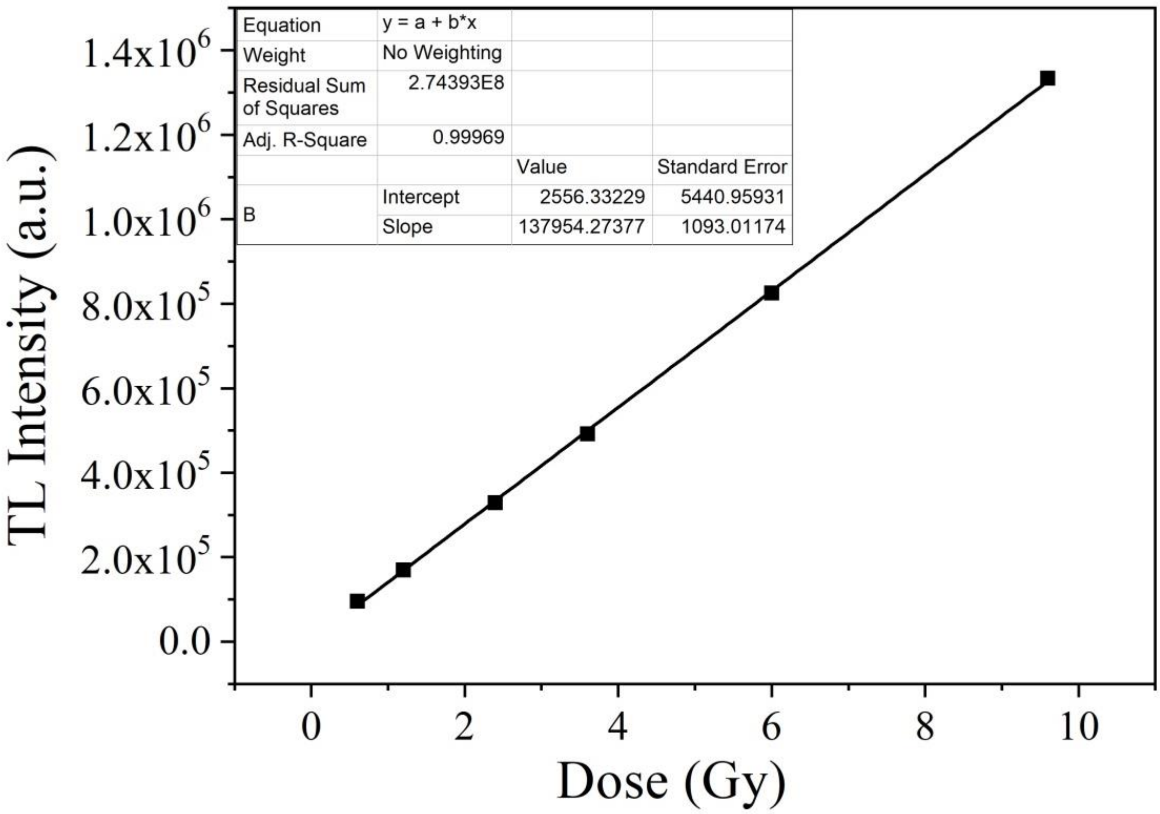

Figure 4.18. The plot for the linear relation between total intensity of all area versus given dose.

Dose Response for UVC irradiated samples:

Considering that UVC has both ionizing and non-ionizing effects, tridymite samples were repeatedly subjected to UVC for 30 min to 4 hours at RT in order to discuss the effect of non-ionizing radiation on the TL emission. As demonstrated in Figure 4.19, since the sample is sensitive to UVC exposure, the TL intensity increases with the increased irradiation time. The TL glow curve consists of two major maxima at around 120 and 230 ^{o}C, both with shoulder emissions surrounding them, which are most likely related to the previously stated complex mechanism occurring in the lattice structure of tridymite. As compared to the second group, the first group's intensity (at around 120 ^{o}C) is significantly greater. The maximum, which peaked at about 230 °C, exhibits linearity up to 4 hours of UVC exposure, after which it becomes saturated (Figure 4.19) (Balci, et al., 2022).

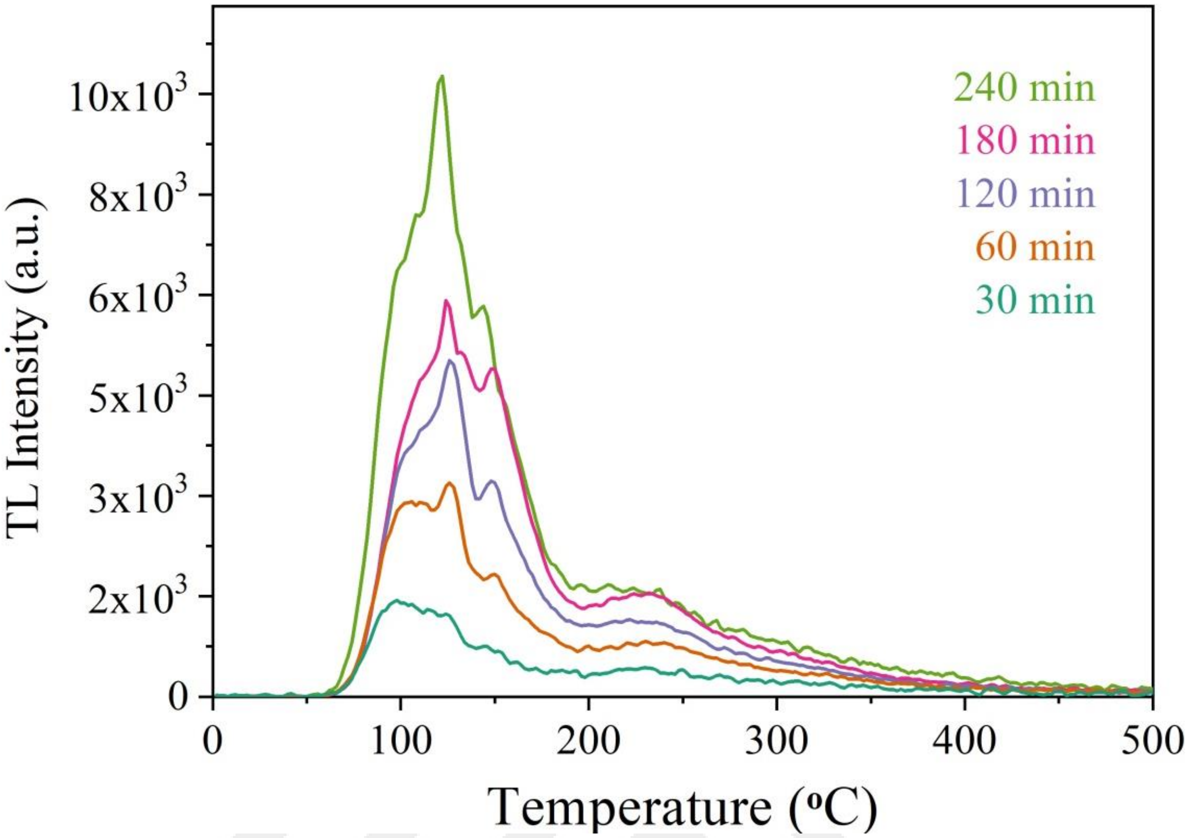

Figure 4.19. The plot for TL dose response of tridymite to UVC irradiation with HR of 5 ^{o}C/s.

As observed in Figure 4.20, the plot of the total intensity of the entire glow curve versus the irradiation time confirms that the dose response is linear, with a reasonable regression coefficient of 0.9746 (Balci, et al., 2022).

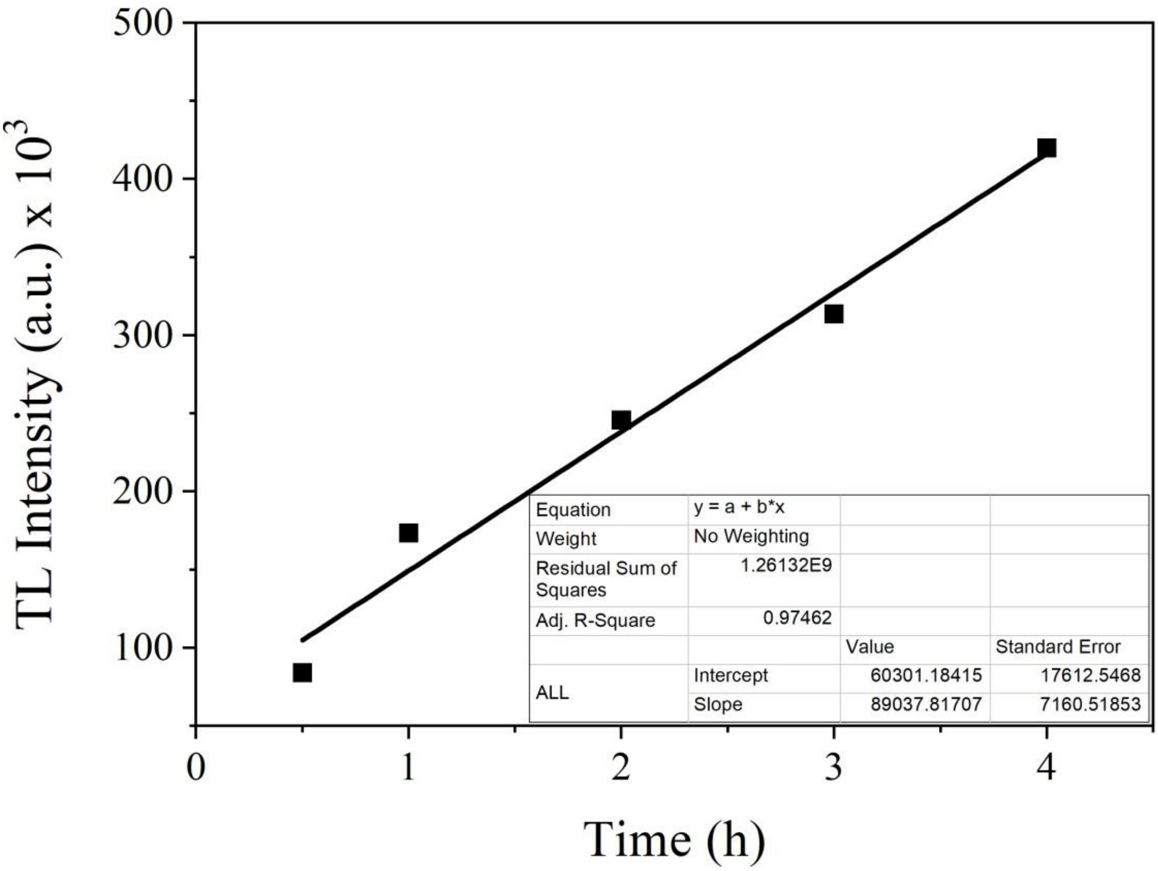

Figure 4.20. The plot for the linear relation between total intensity of all area versus irradiation time.

Consequently, this saturation phenomenon is the primary distinction between the impacts of beta and UVC radiation on the TL structure of tridymite: For the beta dose response (in the range of 0.6-9.6 Gy), there is a linear progression; however, for the UVC dose response, the maximum, which peaks at around 230 °C, demonstrates nonlinear (sublinear) behavior beginning 4 hours after UVC exposure (Balci, et al., 2022).

Kinetic Parameters (First Part – First glance)

Dose response experiment was the first step to obtain an idea about the kinetic order and other parameters for the TL emission of the sample. Maximum TL intensities (T_{max}) scarcely shift throughout the examined dose range (see Figure 4.17), indicating first order kinetics for the TL characterization, and this pattern might be described by assuming the one trap one recombination center (OTOR) model (Braunlich, 1967; Topaksu, et al., 2018). Accordingly, it could be assumed that the defects are not uniformly distributed, in which the traps are initially empty, and the glow emission is proportional to the amount of occupied traps when the irradiation process is complete. Nevertheless, the identification and characterization of the group of components included in the luminescence process using analytical models by assuming first-order kinetics were insufficient. Hence, it could be plausible that the TL emission would be connected with multiple groups of components, resulting a continuity in the trap distribution. This hypothesis can be tested using the T_{max}-T_{stop} procedure (Sarasola-Martin, et al., 2021).

T_{max}-T_{stop}

The thermal stability of tridymite using successive cycles of (i) irradiation, (ii) preheating treatment, and, (iii) TL readout, enables us to identify the distribution of the trap system and the groups of components that fit the TL glow emission. This well-known procedure, (T_{max}-T_{stop} method), is displayed in Figure 4.21 where the study is performed on 1.2 Gy beta irradiated TL emission from the sample starting with a thermal pretreatment of 150 ^{o}C and a subsequent readout up to 500^{o}C. The resultant glow emission (with preheat: 150 ^{o}C), that would correspond to the more stable signal from the dosimetric viewpoint, consists of three maxima peaked at ca. 200, 230, and 320 ^{o}C, which were defined below:

a) The maximum at lower temperature (ca. 200 ^{o}C) could be linked to the phase transition from H3-T(OS) (space group $P2_1(\alpha\beta0)$) to H2-T(OC), (space group $C222_1$) (Graetsch, 2001), (Here H2-T and H3-T correspond to high temperature tridymite and OS is the modulated form of the C-centered orthorhombic phase -OC-),
b) The maximum at ca. 230^{o}C would be linked to alkali ions moving away from Al that lead to $[AlO_4]^o$ hole-like centers or $[GeO_4/Li]^o$ centers (caused by preheat treatment) (Correcher, et al., 2009; Guzzo, et al., 2017).
c) The maximum at around 320 ^{o}C could be linked to a phase transition from H2-T(OC) to LHP(lro) with the space group P_6322 (Dove, et al., 2000), just with the electron combination with the unstable holes trapped at oxygen vacancies next to Al ions and this could be probably due to the presence of the β–tridymite phase (Here LHP was defined as lower-temperature hexagonal phase and lro was defined as long range order of the apical Si-O bonds) (Balci-Yegen, et al., 2018).

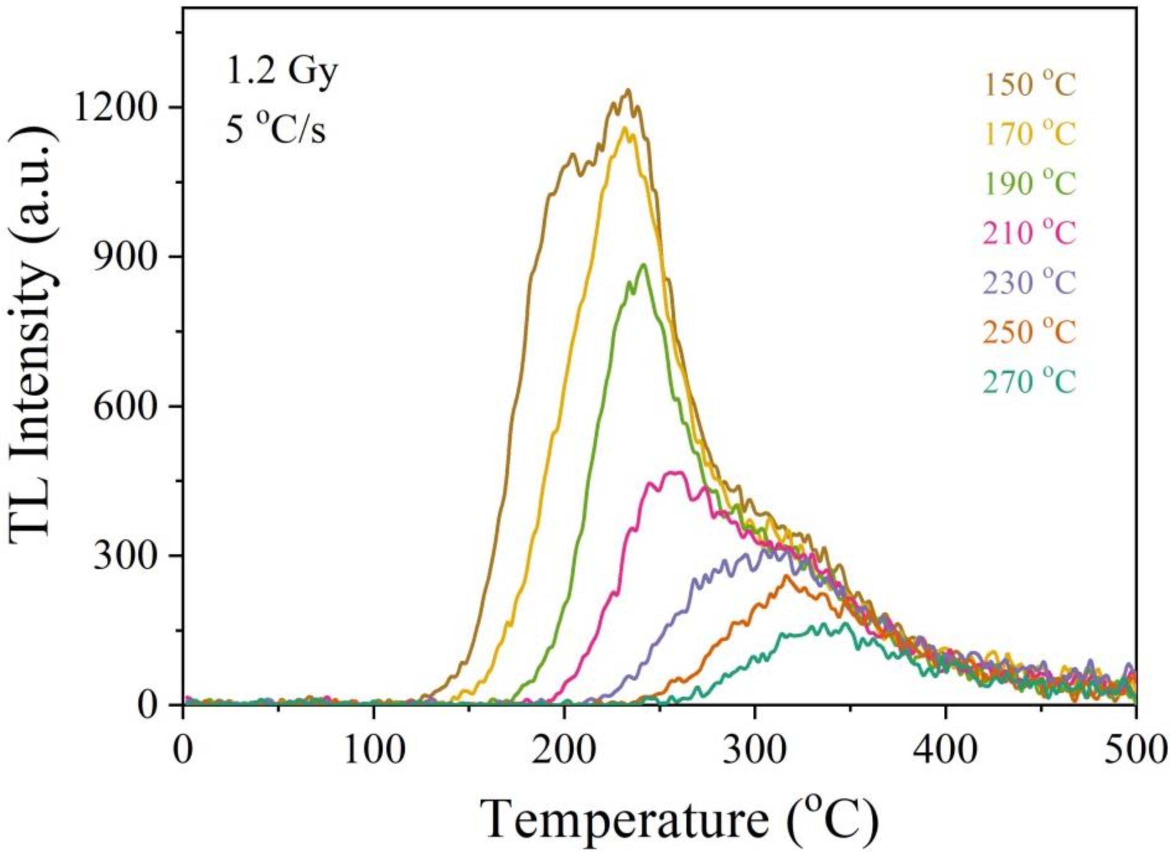

Figure 4.21. The TL glow curves of tridymite mineral samples, preheated up to various temperatures (i.e. T_{stop}) in the range of 150-270 ^{o}C.

By following the T_{max}-T_{stop} protocol and increasing the temperature of the treatments in steps of 20 ^{o}C up to 270 ^{o}C, it is appreciated how;

(i) the form of the glow curve shifts, with the TL maximum shifting to higher temperatures,
(ii) the intensity of the glow curve reduces as the temperature rises, whereas
(iii) the higher temperatures portion of the glow curves was unaffected (Correcher, et al., 2008).

This behavior would probably be linked to various processes involving redox reactions, structural changes (phase transitions as mentioned above), partial breaking and linking bonds of the O-Me (where Me would be the Cr^{3+}, Ni^{2+}, Ti^{4+}, etc. replacing the Si^{4+}), mainly with a change in the lattice modulation as a result of the thermal treatment (Balci-Yegen, et al., 2018).

Trap Distribution System

T_{max}-T_{stop} method is valid to confirm that tridymite exhibits a continuous trap distribution (CTD) system more than a discrete trap distribution (DTD) (Correcher, et al., 1999). Considering the FOM value, the evaluation of the kinetic parameters of the investigated sample based on the widely accepted first or second order kinetics was not sufficient (Balian & Eddy, 1977).

Figure 4.22 (depicted from Figure 4.21) shows the existence of 3 groups of slope-varying components, which can be clearly distinguished from each other. In this regard, the kinetic parameters will be determined using methods other than GCF (glow curve fading), such as IR and VHR (Balci-Yegen, et al., 2018).

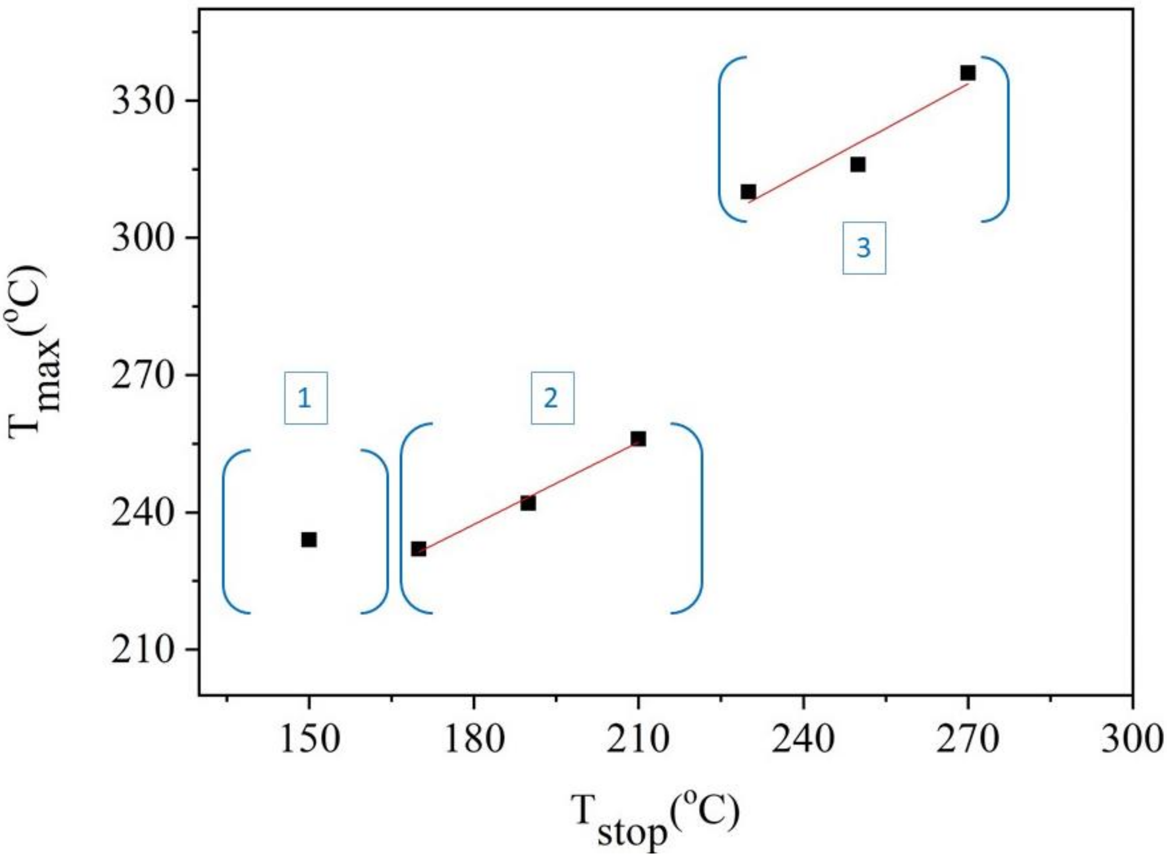

Figure 4.22. The plot for the temperature corresponding to the temperature position of the maximum TL intensity (T_{max}) versus the temperature value of preheat (T_{stop}) along with the linear fittings. Three groups of components marked as 1, 2, and 3.

Initial Rise

The Arrhenius plot in the temperature range of 132 to 164 °C for the sample preheated at 150°C is shown in Figure 4.23. As obtained, the E_a value for tridymite (1.23(4) eV) corresponds quite well with the E_a value observed for Al-Li doped quartz using a GCF method that assumes general order kinetics to identify each peak (Gomez-Ros, et al., 2002; Balci-Yegen, et al., 2018).

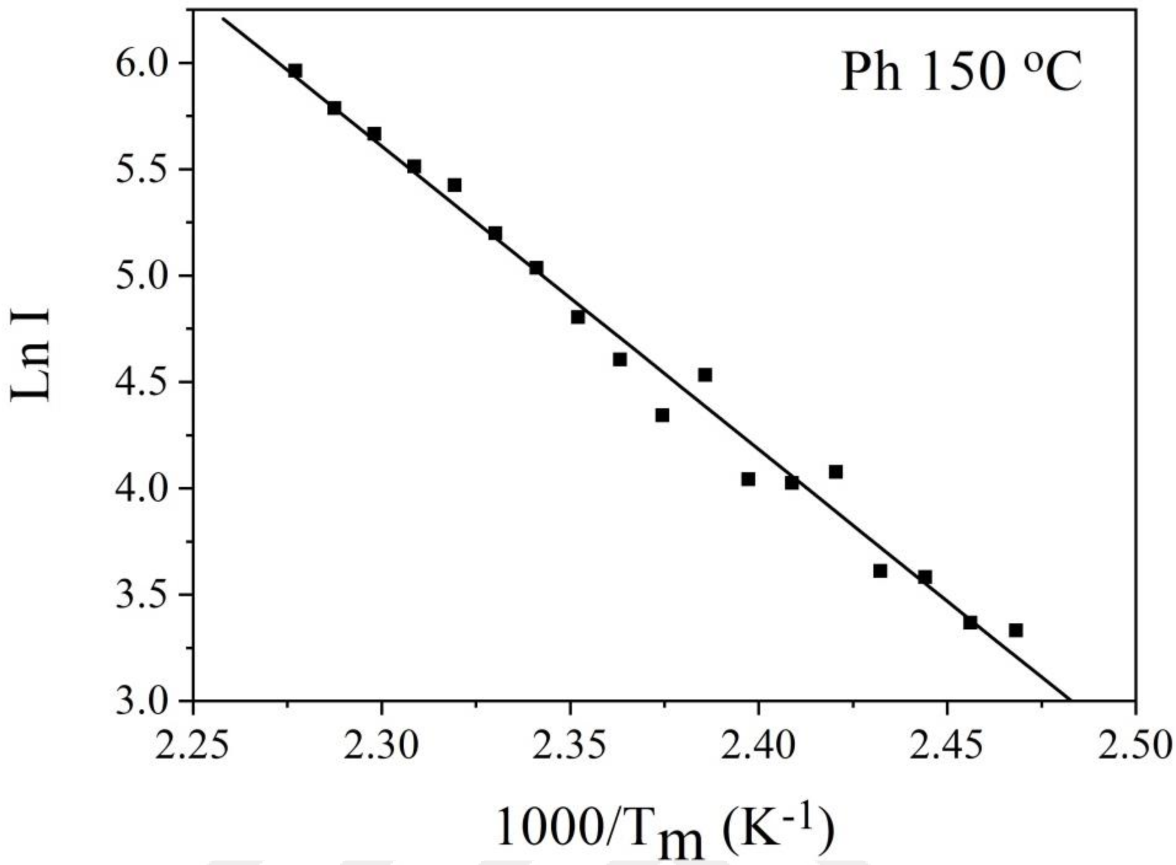

Figure 4.23. The Arrhenius plot of the low-T side of 150 ^{o}C preheated TL curve of tridymite where E_a is 1.23(4) eV.

For the other preheated samples (170-270 ^{o}C in steps of 20 ^{o}C), the Arrhenius graphs were generated and the data were arranged in a table to provide a more practical presentation. As a result, the calculated trapping parameters from the TL glow curves fitting of continuous trap distribution of tridymite by using the IR method are shown in Table 4.3 for each T_{stop} value. It can be confirmed that, as aforementioned, this sample displays three groups of components that grows the E_a value where the last one exhibits a progressive increase from 1.5(2) to 2.1(3) eV.

Table 4.3. Kinetic parameters obtained for the 1.2 Gy irradiated tridymite samples using IR.

T_{stop} (^{o}C)	range (^{o}C)	*a*	*b*	E_a (eV)	*r*	component no
150	132-166	38(1)	-14.3(4)	1.23 (4)	0,993	1
170	154-172	42(4)	-17(2)	1.4 (1)	0,961	2
190	174-192	46(3)	-19(2)	1.7 (1)	0,975	
210	200-218	39(2)	-17(1)	1.45 (8)	0,989	
230	220-230	38(4)	-17(2)	1.5 (2)	0,985	3
250	240-280	41(4)	-20(2)	1.7 (2)	0,944	
270	272-292	47(6)	-24(3)	2.1 (3)	0,931	

Both from Figure 4.23 and Table 4.3 (signed numbers 1, 2, and 3 in both represented the same components), it could be deduced:

a) The trap depth for T_{stop} at 150 (component number 1 in Table 4.3 and Figure 4.22), which corresponds the maximum at 200 ^{o}C could be due to the phase transition from H3-T(OS) (space group P21(αβ0)) to H2-T(OC), (space group C2221) (Graetsch, 2009), (where H2-T and H3-T correspond to high temperature tridymite and OS is the modulated form of the C-centered orthorhombic phase -OC-),
b) The activation energy values for T_{stop} at 170, 190 and 210 ^{o}C are seen as overlapped (except the one at 170 ^{o}C) and could be considered as in the same group of components (number 2 in Table 4.3 and Figure 4.22), which have maxima peaked at around 230, 240, and 260 ^{o}C, respectively. It was reported that the phase transition from H3-T(OS) to H2-T(OC) was suggested to be at around 246 ^{o}C and this assumption could be linked to the maxima peaked at around 240 (Dove, et al., 2000). In addition, an anomalous E_a value of 1.7(1) draws the attention away from other components of the same group, and it could probably be due to a coexistence of both the alkali ions displacement (for example presence of $[GeO4/Li]^0$ centers) (Guzzo, et al., 2017) and/or one of the eight possible phase transition that occurring between 70 and 475 ° C (Dove, et al., 2000). Nevertheless, further work is necessary to confirm such assertion.
c) The trap depths for T_{stop} 230, 250 and 270 ^{o}C are seen as overlapped so they assumed to be in the same group of components (number 3 in Table 4.3 and Figure 4.22), which have maxima peaked at around 310, 315, and 340 ^{o}C, respectively. It was reported that E`1 centers might be the active electron traps responsible for the maximum peak at around 325 ^{o}C (Guzzo, et al., 2017). Furthermore, the maximum peaked at around 340 could be link to the phase transition from H2-T(OC) to LHP(lro) with the space group P6322 (here LHP was defined as lower-temperature hexagonal phase and lro was defined as long range order of the apical Si-O bonds) (Dove, et al., 2000; Balci-Yegen, et al., 2018).

Kinetic Parameters (Second Part –IR Based)

As a result, according to the E_a values derived using IR analysis, it is possible to be differentiate at least three groups of trap components at various levels for the preheating treatments at 150 °C and above. (This TL region should correlate with a more stable area for dosimetric applications). Increasing thermal preheating results in (i) continuously higher E_a values, and (ii) progressively higher IR temperature ranges, confirming the continuum trap distribution hypothesis (except for the aforementioned anomaly). All the conditions produce regression coefficients that are satisfactory, with values never decreasing below 0.931 (Table 4.3).

Although the E_a value derived by the IR technique is regarded as an acceptable approximation, it is possible to alter it by preheat treatment and/or HR. Therefore, VHR process appears to be another acceptable method for determining the E_a value and the pre exponential factor (s).

Various Heating Rate

The TL glow curves of beta irradiated (with 1.2 Gy) tridymite phosphor at different HR values (3, 4, 5, 6 ^{o}C/s) are shown in Figure 4.24. Although the general shape and the structure of the glow curves are almost the same and exhibit five maxima, the position of the T_m value shifts to higher temperatures while the HR value increases. Lower temperature part of the TL glow emission (i.e., between 80 to 150 °C) would be related to structural defects in the lattice such as oxygen vacancies, substitution, and interstitial atoms and/or impurities that generate localized charge losses in all glow curves, HR values regardless (Correcher, et al., 2009; Lieb & Keinonen, 2006). It would be appreciated an increase in the TL intensity of the low-temperature region emission while HR value increases, contrary to the higher temperature peaks. According to a study (Zimmerman, 1971), this increase-decrease behavior in TL intensity could be associated with the pre-dose effect, which was later improved by another study (Haskell & Bailiff, 1985). Their aim was about test the sensitivity of the 110 ^{o}C TL peak of quartz, which is gradually increase by successive readouts using heating treatment to higher temperatures (500 ^{o}C) right after a pre-dose (< 5 Gy) and also followed by a decrease in sensitivity in the same conditions as above. In this thesis, we would see the same pre-dose phenomenon caused by the activated luminescence centers (i.e., transferring of holes from the valance band to inactivated luminescence centers), giving rise to an overall increase in the hole concentration of luminescence centers to recombination centers ratio and hence, an increase in the luminescence efficiency (Gonzalez & Correcher, 2014). In contrast, the glow emission over 120°C (including the 130–140°C maximum) would be caused by one of the eight possible phase transitions occurring within the temperature range of 70–475°C (ref dove). It exhibits a drop in TL intensity as HR value increases and has also been reported in the synthesis of various semiconductors (Delice, et al., 2015; Balci-Yegen, et al., 2018).

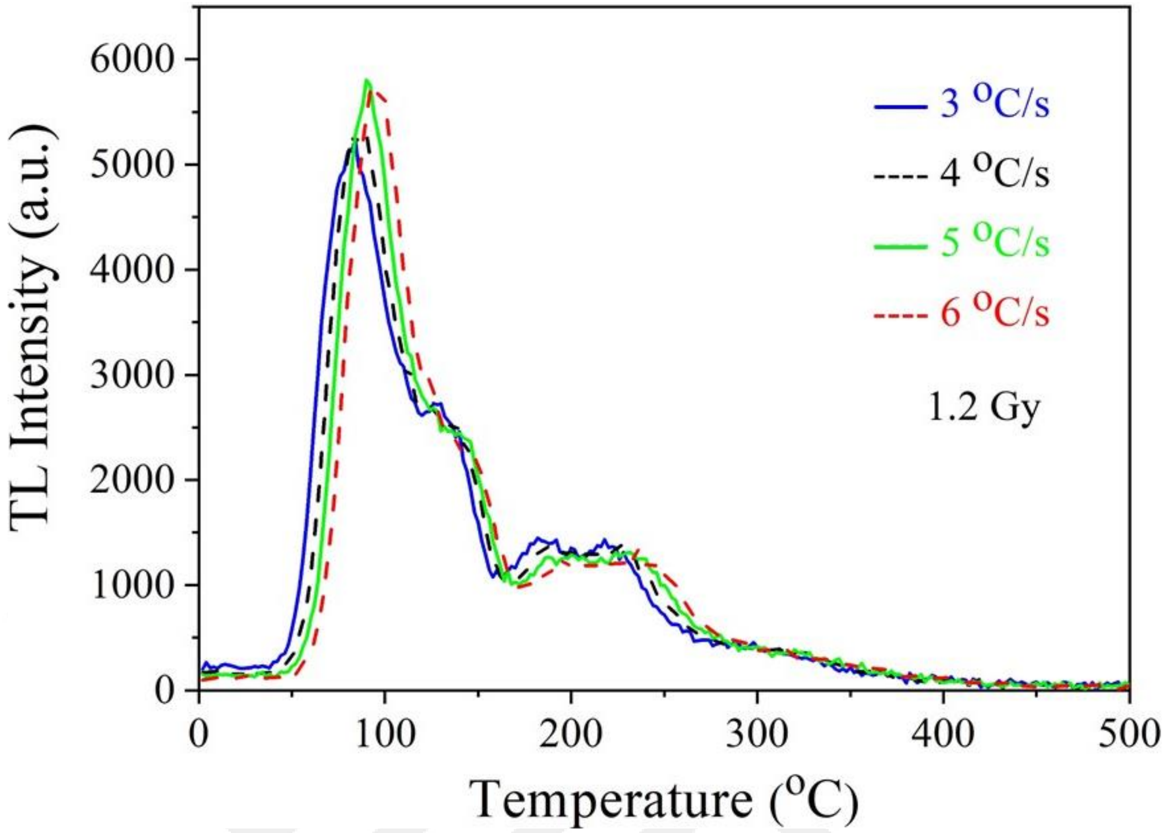

Figure 4.24. The glow curve behavior of tridymite measured at different heating rate values of 3, 4, 5, and 6 ^{o}C/s after irradiation to 1.2 Gy.

Kinetic Parameters (Third Part-VHR Based)

The Arrhenius plot derived from the glow curves with these HR values (3, 4, 5, 6 ^{o}C/s) for the maximum peaked at around 230-240 ^{o}C is shown in Figure 4.25. An acceptable linear regression (with r = 0.9698) was derived from the plot, which was evaluated by using Eq. (2). Likewise, the slope and intercept of the plot provide the trap depth E_a and the frequency factor s, which are 1.5(2) eV and 3.79×10^{12}, respectively.

Comparison of E_a values employing both results from IR and VHR methods is fairly well correlated for these maxima that would correspond with more stable blue TL emission being of interest from the dosimetric viewpoint. As observed in the Table 4.3 and Figure 4.23, the E_a values of the maxima peaked at 230 ^{o}C are 1.5(2) eV for both kinetic parameter estimation techniques (Balci-Yegen, et al., 2018).

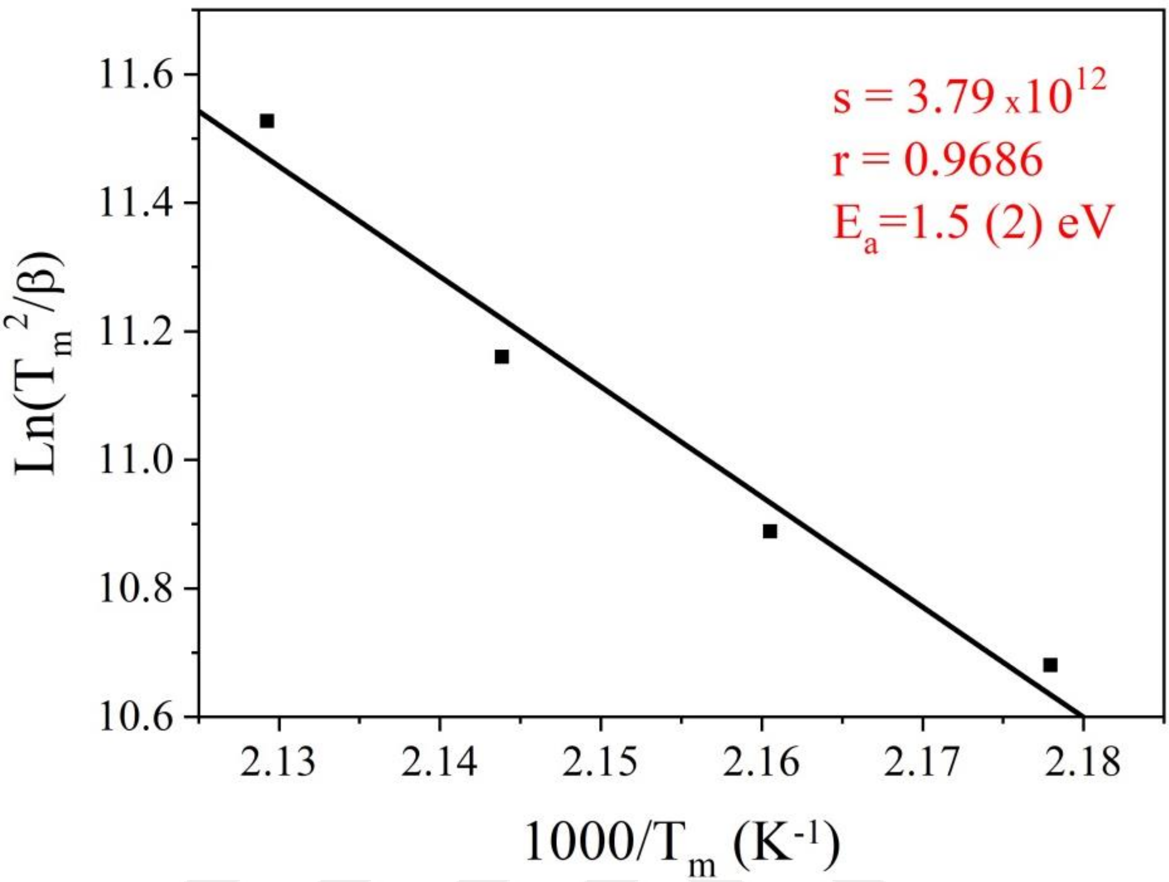

Figure 4.25. The Arrhenius plot for the maxima at around 230-240 ^{o}C.

CGCD Analysis for Beta-, UVC-, and Non-Irradiated Samples

Although the separation process with the CGCD method was applied for all doses, it was found appropriate only 3 selected TL glow curve samples to be shown in Figure 4.26. The TL glow curves for all barely shift the position of the maxima peaked at around 190, 235, and 300 ^{o}C (with disregarding the type of radiation for the luminescence process consists of natural (i.e., from α, β, γ, and cosmic rays), beta (from Sr^{90}/Y^{90} source), and UVC radiation)). In this circumstance, it would be confirmed that the specified groups of components could be linked to the same physical-chemical changes resulting from highly probable phase transitions, in which occurred during the thermal treatment up to 500^{o}C for TL readout.

Furthermore, the initial irradiation process causes major differences in the shape of the TL glow curve, which are mostly comprised of:

a) Peak I was split in two when the material was irradiated with UVC, most likely as a result of:

- dehydration mechanism (seen to be appearing at around 100 ^{o}C)
- a potential photo-oxidation process that could provide a water radiolysis wherein free radicals adsorbed on the surface of the material can cause a number of rapid reactions with a peak temperature of 125 ^{o}C, such as dehydroxylation reactions (Kitis, et al., 1990).

(This peak splitting behavior has not been recognized the for samples exposed to beta radiation).

b) Low temperature peaks that appear in the emission of beta at 100 °C and UVC at around 100 - 120 °C are highly transient, unstable and defined as non-dosimetric. Since it is clear that this component is caused by radiation, not detectable in the NTL glow curve results.

c) The phenomenon of photo-transferred thermoluminescence (PTTL) is most likely responsible for the UVC-induced shift of the glow peaks to lower temperatures (Alexander & McKeever, 1998). This effect can be explained by charge transfer from deep to shallower traps through the stimulation provided by expose to UV light. (it has been examined for various materials, and proposed for use in radiation dosimetry and ceramic sample dating (Aitken, 1990; Morris & McKeever, 1994; Murray, 1996)).

Peaks in the high temperature portions of NTL curves, i.e., at about 370 and 460 ^{o}C, are not observed in induced-TL signals. This could be due to the time between irradiation exposure and TL readout having become quite short for UVC and beta irradiation compared to natural radiation (Balci, et al., 2022).

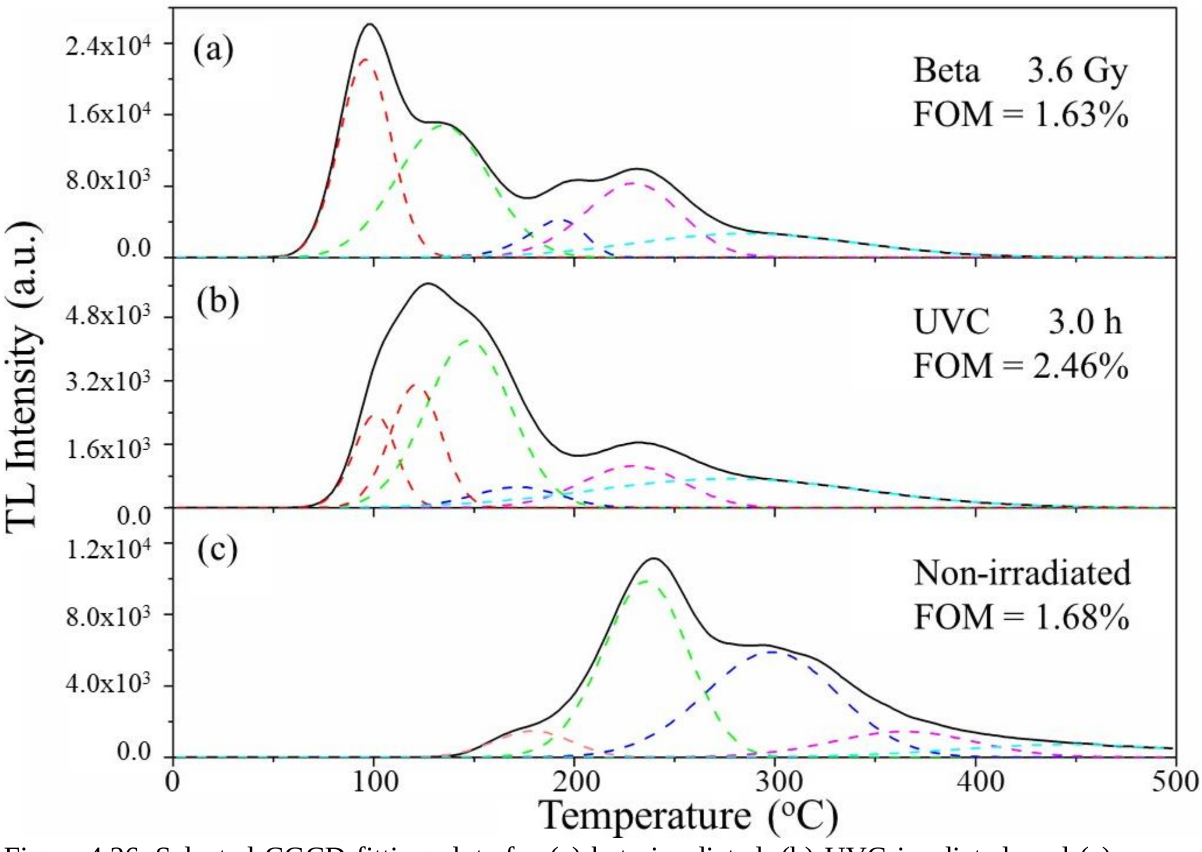

Figure 4.26. Selected CGCD fitting plots for (a) beta irradiated, (b) UVC irradiated, and (c) non-irradiated samples.

Kinetic Parameters (Forth Part - CGCD Based)

Table 4.4 shows the kinetic parameters obtained by CGCD analysis, which is more comprehensive than others such as Various Heating Rate (VHR) or Initial Rise (IR) (Balci-Yegen, et al., 2018), and matched with E_a obtained from them. According to Table 4.4, the FOM values, which represent the "quality" of the fitting for experimental results, were never larger than 2.36 % for both the NTL and beta-induced luminescent emissions. But when the results from UVC-irradiated samples are analyzed, the slightly higher noise signal creates the FOM values to increase. However, the values still remain lower than 4.2%, so it appears to be an acceptable fit (Balci, et al., 2022).

Table 4.4. Kinetic parameters (I_M, T_M, E_0 and σ) of beta-irradiated tridymite samples obtained by CGCD fitting method. The uncertainties are 1σ throughout the whole calculations.

		Peak I				Peak II				Peak III				Peak IV				Peak V			
FOM	Dose	E (eV)	σ (eV)	T_{Max} (°C)	I_{Max}	E (eV)	σ (eV)	T_{Max} (°C)	I_{Max}	E (eV)	σ (eV)	T_{Max} (°C)	I_{Max}	E (eV)	σ (eV)	T_{Max} (°C)	I_{Max}	E (eV)	σ (eV)	T_{Max} (°C)	I_{Max}
2.36%	0.6	2.336	0.083	95	1716	1.99	0.107	142	816	1.40	0.018	193	287	1.58	0.058	235	610	1.98	0.184	298	187
1.82%	1.2	2.359	0.082	96	3247	1.95	0.110	141	1345	1.40	0.017	193	334	1.51	0.062	235	1035	1.89	0.193	296	328
1.71%	2.4	2.408	0.080	97	6133	1.96	0.109	140	2785	1.36	0.016	193	757	1.54	0.060	235	2033	1.90	0.192	293	651
1.65%	3.6	2.429	0.080	97	8982	1.99	0.107	140	4613	1.46	0.017	193	1415	1.57	0.059	235	3295	2.07	0.176	301	950
1.74%	6.0	2.456	0.079	98	14054	1.94	0.110	139	8259	1.49	0.016	194	2192	1.53	0.062	235	5198	1.92	0.188	300	1514
1.63%	9.6	2.469	0.079	98	21728	1.98	0.107	139	14463	1.44	0.017	194	4198	1.57	0.059	235	8072	1.93	0.188	297	2601
		2.4(1)	0.08(2)	96.7(5)		1.96(6)	0.11(2)	140.3(5)		1.42(10)	0.02(1)	192.9(4)		1.55(7)	0.06(2)	234.8(2)		2.0(1)	0.19(4)	297.7(8)	

Table 4.5. Kinetic parameters (I_M, T_M, E_0 and σ) of UVC-irradiated tridymite samples obtained by CGCD fitting method.

		Peak I_a				Peak I_b				Peak II				Peak III				Peak IV				Peak V			
FOM	**T**	E (eV)	σ (eV)	T_{Max} (°C)	I_{Max}	E (eV)	σ (eV)	T_{Max} (°C)	I_{Max}	E (eV)	σ (eV)	T_{Max} (°C)	I_{Max}	E (eV)	σ (eV)	T_{Max} (°C)	I_{Max}	E (eV)	σ (eV)	T_{Max} (°C)	I_{Max}	E (eV)	σ (eV)	T_{Max} (°C)	I_{Max}
4.21%	0.5h	2.21	0.052	99	386	2.53	0.053	122	222	1.996	0.106	144	235	1.40	0.044	199	66	1.60	0.061	241	93	2.01	0.199	321	68
3.68%	1h	2.28	0.052	101	2201	2.45	0.049	124	1695	1.943	0.111	147	1850	1.46	0.047	195	273	1.55	0.060	238	579	1.93	0.193	303	422
3.20%	2h	2.29	0.051	102	2147	2.34	0.065	126	2829	1.942	0.110	150	2593	1.21	0.050	193	366	1.52	0.063	240	681	1.88	0.227	293	528
2.45%	3h	2.24	0.053	103	2303	2.36	0.066	124	3043	2.103	0.098	151	4118	1.24	0.047	176	507	1.54	0.064	235	1024	1.81	0.221	290	712
3.06%	4h	2.20	0.054	101	1589	2.42	0.049	125	1735	2.057	0.103	150	1559	1.39	0.041	195	190	1.60	0.062	234	371	2.01	0.204	305	264
		2.2(1)	0.05(2)	101.4(7)		2.4(2)	0.06(5)	124.1(7)		2.0(2)	0.11(4)	144(1)		1.3(2)	0.05(3)	192(2)		1.6(1)	0.06(2)	238(1)		1.9(2)	0.21(7)	302(2)	

78

Table 4.6. Kinetic parameters (I_M, T_M, E_0 and σ) non-irradiated natural tridymite samples obtained by CGCD fitting method.

		Peak I				Peak II				Peak III				Peak IV				Peak V			
FOM	**Sample**	E (eV)	σ (eV)	T_{Max} (°C)	I_{Max}	E (eV)	σ (eV)	T_{Max} (°C)	I_{Max}	E (eV)	σ (eV)	T_{Max} (°C)	I_{Max}	E (eV)	σ (eV)	T_{Max} (°C)	I_{Max}	E (eV)	σ (eV)	T_{Max} (°C)	I_{Max}
1.68%	1	2.130	0.080	183	1437	2.120	0.076	240	9586	1.826	0.093	306	5709	1.891	0.090	372	1392	1.694	0.118	459	688
2.28%	2	1.942	0.094	188	593	2.248	0.069	236	3167	1.756	0.097	297	1697	1.765	0.096	368	388	1.473	0.141	459	226
2.27%	3	2.051	0.087	191	433	2.181	0.073	242	2530	1.882	0.092	307	1474	1.926	0.089	369	468	1.558	0.127	462	335
		2.0(2)	0.09(6)	187(1)		2.2(2)	0.07(4)	239(1)		1.8(2)	0.09(4)	303(1)		1.9(2)	0.09(4)	370(1)		1.6(2)	0.13(8)	460(1)	

The peaks were best fitted by following:

- Taking into account general order kinetics (GOK)
- Making the assumption of a continuum trap Gaussian distribution.

The cycle of processes (irradiation and TL readout) could be regarded to be link with:

- Structural defects,
- Intrinsic defects,
- Extrinsic defects,
- Redox reactions,
- Dehydration reactions,
- Dihydroxylation reactions,
- Phase transitions.

These processes are responsible for the creation of the TL curve, which could be observed in the distribution of relatively near energy states, and which has the potential to be correlated with a linear mixture of five FOK functions when a Gaussian distribution is taken into account (Figure 4.27). The system depends on FOK and GOK for discrete energy distributions, but for continuous energy distributions, it employs Gaussian trap distributions rather than exponential ones (Balci, et al., 2022).

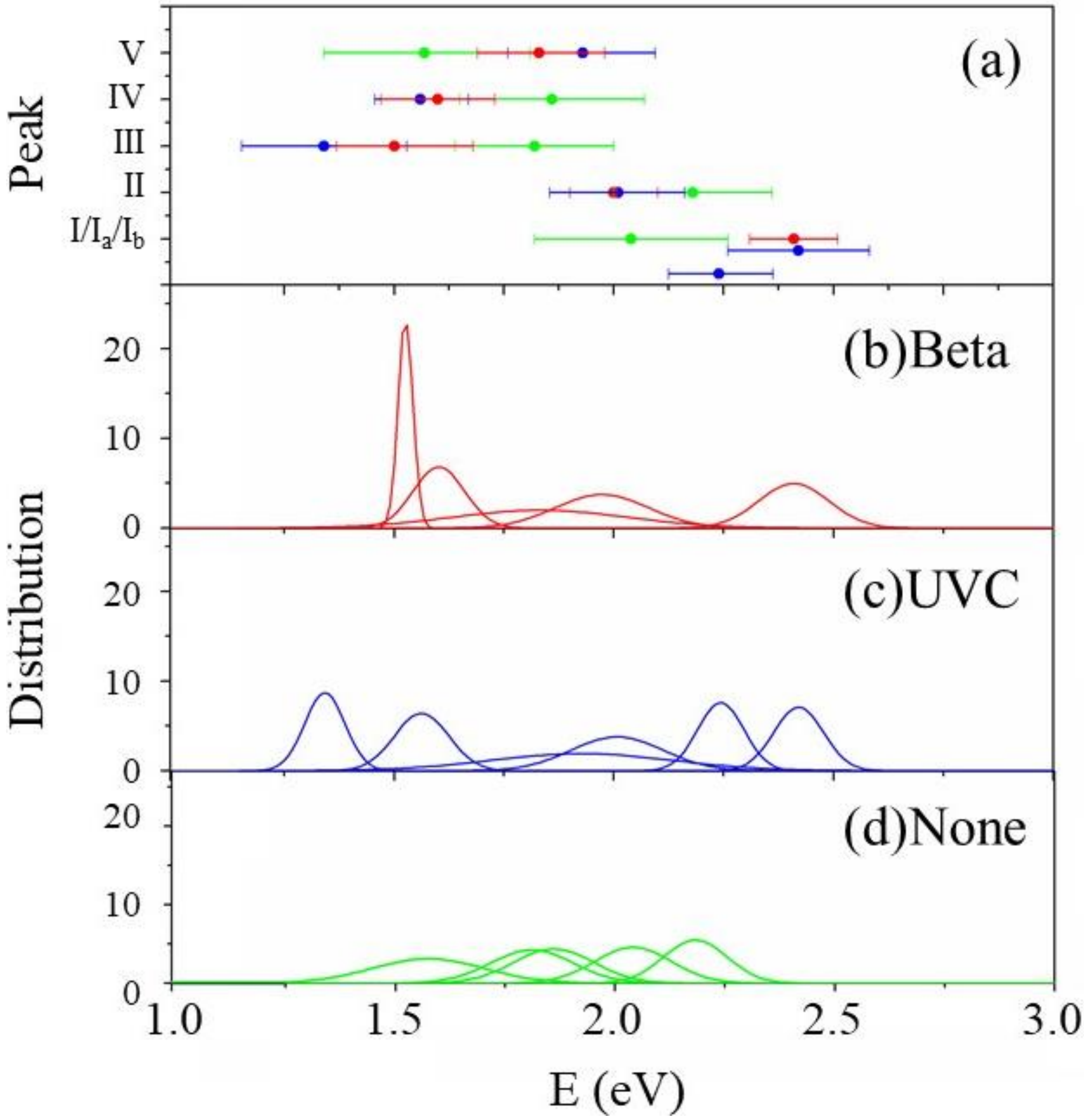

Figure 4.27. The plots for (a) energy levels analogy for each peak, and their possible correlated linear combinations of five FOK functions considering a Gaussian distribution for (b) beta irradiated (c) UVC irradiated (d) non-irradiated samples.

5. CONCLUSIONS

In this thesis, a succinct overview of the undertaken research is provided, along with potential avenues for future investigations. The primary focus of the thesis involved comprehensive inquiries into various aspects of the subject matter.

The elemental composition of tridymite was analyzed using ESEM-EDS and EPMA. The results confirmed that the crystals obtained from all the examined locations were not composed solely of SiO_2. The SiO_2 content in the crystals ranged from 68.66 to 96.12 wt. %. The decrease in SiO_2 content was primarily compensated for by the presence of calcium, which ranged from 3.25 to 28.96 wt. %. Additionally, there was a correlation observed between the abundances of Al, Na, and Fe, with their respective weight percentages ranging from 0.63 to 1.83, 0 to 0.43, and 0 to 0.33 wt. %. These findings highlight the heterogeneous nature of tridymite crystals and indicate the presence of significant amounts of calcium, along with minor amounts of aluminum, sodium, and iron in the studied samples. In accordance with EDS results, according to the EPMA performed on nine different tridymite localities, the weight fraction of SiO_2 ranges from 86.36 to 98.99%. In addition to the elements F and Cl, certain places have been shown to contain trace levels of cations including Al, Fe, Mn, Mg, Ca, Na, K, Ti, Ni, Cr, and P, although other cations are still below the lowest detectable threshold. After all, the chemical composition findings obtained from EDS and EPMA were consistent, reinforcing the validity of the results.

X-ray diffraction (XRD) analysis of tridymite samples revealed a reversible diffraction pattern (suggests monoclinic structure of the crystal), which has been observed in EPR and TL-RU experiments at elevated temperatures. The ability of tridymite to withstand high temperatures is of significant importance in its potential applications in the ceramic industry.

As a future work, the changes in grain size, which can be most rigorously determined from the peak broadening using the Debye-Scherrer equation, and the variations in lattice parameters can be comparatively analyzed based on the thermal X-ray diffraction results.

The Raman spectrum of the sample displays distinct bands at specific wavenumbers, representing the vibrational modes of the molecules present. The major peaks occur at approximately 370 cm^{-1} and 320 cm^{-1}, associated with prominent molecular vibrations. Additionally, the peaks at 410 cm^{-1} and 445 cm^{-1} indicate closely spaced molecular vibrations, while the peak at 220 cm^{-1} may have additional vibrational modes or coupling with vibrations at 155 cm^{-1}. The peaks at 800 cm^{-1} and 1100 cm^{-1}, although of small intensity, are still characteristic of tridymite. Overall, Raman Spectroscopy analysis confirmed the presence of a monoclinic crystal structure in the tridymite samples, as it was found XRD results.

Furthermore, NMR analysis revealed a broad peak, suggesting homogeneity in the local environments of silicon atoms within the tridymite crystal lattice. NMR results provided information to gain insights into the atomic-level structure and dynamics of tridymite. As a future work, by comparing the NMR spectra at different conditions or in different forms of tridymite, it could be further understanding the changes in the local environments of silicon atoms and how they relate to the mineral's properties and behavior. Additionally, the presence of specific NMR peaks allows for identification and characterization of tridymite samples, which can be valuable in various geology and materials science applications.

Risks can arise while doing a kinetic research of EPR under fluctuating temperature and power circumstances, and the knowledge gained may not be sufficient. However, analyzing the irradiation sample offers a conclusive way to judge if the Al impurity center and the Ge impurity center are present within the structure. Notably, the lack of a rise in Mn signals after radiation exposure makes it easier to observe radiation-sensitive signals. So as a future work, sample could be irradiated under different power and temperature conditions.

The observed PL peaks at 693 and 694.5 nm suggest that tridymite exhibits emission in the red region of the visible spectrum. The impurity composition, including elements such as Na, Al, Ca, Fe, and Si, can introduce energy levels or defect states within tridymite. These energy levels influence the electronic transitions and contribute to the observed PL peaks. The PL emission is influenced by various luminescence centers within tridymite. These include O-deficient centers (ODCs) associated with oxygen vacancies or other defects in the lattice. Luminescence centers, such as transition metal ions (e.g., Fe, Mn, Cr) and certain rare earth elements, can facilitate charge transfer processes and induce energy transfer, affecting the emission properties. Certain impurities, particularly transition metal ions and rare earth elements, can introduce non-radiative recombination pathways within tridymite. This reduces the radiative recombination efficiency and leads to a quenching effect on the PL intensity. The impurity content and distribution influence the crystal structure of tridymite, which in turn affects the electronic and optical properties. Grain boundaries, strain, and structural defects can alter the emission characteristics, including the emission wavelength observed in the PL spectrum.

Complementary CL spectroscopy results provide additional insights into the influence of impurity defects, such as GeO_4^{3-}+e and AlO_4^{4-}+e, on the radiative recombination processes responsible for the PL emission of tridymite. In addition, the possible existence of impurities and luminescent centers causing PL and CL sensitivities overlap with each other.

TL, when combined with techniques such as differential scanning calorimetry, other luminescence techniques, or Raman, offers an additional experimental approach for examining phase transitions in various materials, including insulators and semiconductors. Tridymite, which finds practical applications in ceramics and geology, displays a complex TL emission spectrum at 400 nm, featuring five peaks observed at temperatures of 90, 130, 200, 230, and 320°C (using a heating rate of 5°C per second). The lower temperature peaks are likely attributed to structural defects in the lattice, such as oxygen vacancies, substitution and interstitial atoms, or impurities, which result in localized charge losses. The emission above 200°C is associated with the following phenomena: (i) a phase transition from H3-T(OS) to H2-T(OC); (ii) the migration of alkali ions away from aluminum, leading to the formation of hole-like centers such as [AlO4]° or [GeO4/Li]°; and (iii) a phase transition from H2-T(OC) to LHP(lro), accompanied by electron recombination with unstable holes trapped near oxygen vacancies adjacent to aluminum sites. By subjecting the material to successive thermal pretreatments within the range of 150–270°C, it has been possible to confirm the presence of a continuum in the trap system, following the T_{max}–T_{stop} protocol. The activation energy values determined through IR and VHR techniques exhibit a notable correlation.

Furthermore, the correlation between T-XRD and TL results of tridymite, a polymorph of quartz that has played a significant role in the advancement of ceramics and glass-ceramic manufacturing, provides insights into how the material's structure can be affected by thermal treatment, radiation exposure (beta and UVC), or a combination of both. The presence of defects causing changes in the tridymite structure, primarily related to partial phase transitions, dehydration of adsorbed water molecules, hydroxylation, dehydroxylation, and redox reactions, is shown to be reversible when the material returns to RT. T-XRD results reveal a reversible process where the (204) and (321) crystallographic planes, in the range of 26-28° 2θ, modify the structure up to a temperature of 200°C while maintaining the same XRD patterns at RT. This behavior could be associated with the phase transition from H3-T (OS) to H2-T (OC).

The stability of the structure is further confirmed through TL tests. Successive cycles of experiments involving fixed ionizing exposure (1.2 Gy) and readout up to 500°C, increasing beta doses ranging from 0.6 to 9.6 Gy and readout up to 500°C, and increasing UVC exposure from 30 to 240 minutes followed by TL readout up to 500°C, indicate negligible changes in the sample structure. These findings are supported by the estimation of TL kinetic parameters analyzed using the CGCD method. The TL results demonstrate that the tridymite sample could be considered suitable for use in environmental dosimetry and UV dosimetry fields, and they contribute to a better understanding of the structure of tridymite discovered on Mars. Moreover, they hold significance in conducting research on the planet's formation processes and potential habitability.

Additionally, as another valuable future work, comparative studies can be conducted on tridymite samples obtained from different geographical locations, including those retrieved from Mars, utilizing the techniques employed in this thesis.

REFERENCES

Aitken, M. J., 1990. *TLD methods in archeaometry, geology and sediment studies.* Vienna, 9th International Conference on Solid State Dosimetry.

Alexander, C. S. & McKeever, S. W. S., 1998. Phototransferred thermoluminescence. *Journal of Physics D: Applied Physics*, 31(20), pp. 2908-2920.

Aparicio, A., Bustillo m., Garcia, R. & Arana, V., 2006. Metasedimentary xenoliths in the lavas of the Timanfaya eruption (1730–1736, Lanzarote, Canary Islands): Metamorphism and contamination processes. *Geological Magazine*, 143(2), pp. 181-193.

Bailiff, I. K., 1994. The pre-dose technique. *Radiation Measurements*, 23(2-3), pp. 471-479.

Bailiff, I. K. et al., 2005. Retrospective luminescence dosimetry: development of approaches to application in populated areas downwind of the Chernobyl NPP. *Health Physics,* 89(3), pp. 233-246.

Balci, S. ve diğerleri, 2022. Preliminary study on the thermally stimulated luminescence characterization of UVC and beta irradiated tridymite. *Applied Radiation and Isotopes*, Cilt 186, p. 110300.

Balci-Yegen, S. et al., 2018. Correlation between thermoluminescence emission and phase transition of tridymite. *Phase Transition,* Volume 91, pp. 1122-1128.

Balci-Yegen, S. et al., 2018. Thermoluminescence dose and heating rate dependence and kinetic analysis of ZnB2O4:0.05Dy3+ Phospor. *Nuclear Instruments and Methods in Physics Research B: Beam Interactions with Materials and Atoms*, Volume 416, pp. 50-54.

Balian, H. G. & Eddy, N. W., 1977. Figure-of-merit (FOM), an improved criterion over normalized chi-squared test for assessing goodnes-of-fit of gamma-ray spectral peaks. *Nuclear Instruments and Methods,* 145(2), pp. 389-395.

Benavente, J. F., Gomez-Ros, J. M. & Romero, A. M., 2019. Thermoluminescence glow curve deconvolution for discrete and continues trap distributions. *Applied Radiation and Isotopes,* Volume 153, p. 108843.

Braunlich, P., 1967. Comment on the Initial-Rise Method for Determining Trap Depths. *Journal of Applied Science*, 38(6), pp. 2516-2519.

Bustillo, M. A., Nishimura, A., Arana, V. & Hattori, I., 1994. Paleocene Radiolarians from Xenoliths Hosted in Holocene Lavas of Lanzarote (Canary Island). *Geobios*, 27(2), pp. 181-188.

Chen, R. & McKeever, S. W. S., 1997. *Theory of Thermoluminescence and Related Phenomena.* s.l.:World Scientific.

Correcher, V., Garcia-Guinea J., Bustillo, M. A. & Garcia, R., 2009. Study of the thermoluminescence emission of a natural α-cristobalite. *Radiation Effects and Defects in Solids: Incorporating Plasma Science and Plasma Technology*, 164(1), pp. 59-67.

Correcher, V. & Garcia-Guinea, J., 2020. Characterization of the cathodoluminescence emission of kamphaugite-(Y) and kristiansenite from Spain. *Physics and Chemistry of Minerals,* 47(6).

Correcher, V., Garcia-Guinea, J., Boronat, C. & Gomez-Ros, J. M., 2019. Radiation effect on the UV-green thermally stimulated luminescence emission of natural Na-rich aluminosilicates. *Radiation Physics and Chemistry,* Volume 164, p. 108383.

Correcher, V., Garcia-Guinea, J., Delgado, A. & Sanchez-Munos, L., 1999. Spectra thermoluminescence emissions and continuous trap distribution of a cross-hatch twinned low microcline. *Radiation Protection Dosimetry,* 84(1-4), pp. 503-506.

Correcher, V., Garcia-Guinea, J. & Valle-Fuentes, F. J., 2003. Recent results on the thermoluminescence properties of diaspore. *Geophysical Research Letters,* 30(18), p. 1949.

Correcher, V. et al., 2008. Calculation of the activation energy in a continuous trap distribution system of a charoite silicate using initial rise and TL glow curve fitting methods. *Radiation Measurements,* 43(2-6), pp. 267-272.

Correcher, V., Rodriguez-Lazcano, Y., Gomesdarocha, R. & Garcia-Guinea, J., 2016. Effect of the irradiation dose on the luminescence emission of a Mg-rich phyllosilicate. *Journal of Radioanalytical and Nuclear Chemistry,* Volume 307, pp. 1287-1293.

Costa , M. C. F. et al., 2022. Two-Dimensional Quantum Dots: From Photoluminescence to Biomedical Applications. *Solids,* 3(4), pp. 578-602.

Dadsetan, S., Siad, H., Lachemi, M. & Sahmaran, M., 2021. Evaluation of the tridymite formation as a technique for enhancing geopolymer binders based on glass waste. *Journal of Cleaner Production*, 278(123983).

Danilatos, G., 1988. Foundations of Environmental Scanning Electron Microscopy. *Advances in Electronics and Electron Physics,* Volume 71, pp. 109-250.

Danilatos, G. D., 1990. Mechanisms of detection and imaging in the ESEM. *Journal of Microscopy,* 160(1), pp. 9-19.

Delgado, A. et al., 1996. A simple UV irradiator for low dose Reassesment with LiF TLD_100. *Radiation Protection Dosimetry*, 67(4), pp. 303-306.

Delice, S., Bulur, E. & Gasanly, N. M., 2015. Thermoluminescence in gallium sulfide crystals: an unusual heating rate dependence. *Philosophical Magazine*, 95(9), pp. 998-1006.

Dollase, W. A., 1967. The crystal structure at 220°C of orthorhombic high tridymite from the Steinbach meteorite. *Acta Crystallographica,* 23(4), pp. 617-623.

Dove, M. T., Pyrde, A. K. A. & Keen D. A., 2000. Phase transitions in tridymite studied using ‘Rigid Unit Mode’ theory, Reverse Monte Carlo methods and molecular dynamics simulations. *Mineralogical Magazine,* 64(2), pp. 267-283.

Feher, G., 1959. Electron Spin Resonance Experiments on Donors in Silicon. I. Electronic Structure of Donors by Electron Nuclear Double REsonance Technique. *Physical Review,* 114(5), pp. 1219-1244.

Forbes, T. Z., 2018. Luminescence. In: W. White, ed. *Encyclopedia of geochemistry: a comprehensive reference source on the Chemistry of the Earth.* Iowa city: Encyclopedia of Earth Sciences Series, pp. 835-838.

Furetta, C., 2003. *Handbook of termoluminescence.* Singapore: 1world Scientific Publishing Co. Pte. Ltd.

Garcia-Guinea, J. ve diğerleri, 2007. On the luminescence emission band at 340 nm of stressed tectosilicate lattices. *Nuclear Instruments and Methods in Physics Reseach A,* Cilt 580, pp. 648-651.

Garcia-Guinea, J. et al., 2017. Spectral green cathodoluminescence emission from surfaces of insulators with metal-hydroxyl bonds. *Journal of Luminescence,* Volume 190, pp. 128-135.

Garcia-Guinea, J. et al., 2011. Strong Calcite-Like Spectra Cathodoluminescence Emission from Allende Meteorite Cai Phases. *Spectroscopy Letters,* 44(7-8), pp. 516-520.

Garlick, G. F. J. & Gibson, A. F., 1948. The electron trap mechanism of luminescence in sulphide and silicate phorspors. *Proceeding of the Physical Society,* Volume 60, pp. 574-589.

Gilliland, G. D., 1997. Photoluminescence spectroscopy of crystalline semiconductors. *Materials Science and Engineering R-Rports,* 18(3-6), pp. 99-399.

Gomez-Ros, J. M., Correcher, V., Garcia-Guinea, J. & Delgado, A., 2002. . Kinetic parameters of lithium and aluminium doped quartz from thermoluminescence glow curves. *Radiation Protection Dosimetry,* 100(1-4), pp. 399-402.

Gomez-Ros, J. M. & Kitis, G., 2002. Computerized glow curve deconvolution using general and mixed order kinetics. *Radiation Protection Dosimetry,* 101(1-4), pp. 47-52.

Gonzalez, M. & Correcher, V., 2014. On the cathodoluminescence and thermoluminescence emission of lithium titanate ceramics. *Joural of Nuclear Materials,* 445(1-3), pp. 149-153.

Görelik, V. S. & Pyatyshev, Y., 2019. Raman opalescence of a destabilizing soft mode near the phase transition in quartz monocrystals. *Journal of Raman Spectroscopy,* 50(10), pp. 1584-1593.

Gorobets , B. & Rogojine, A., 2002. *Luminescence spectra of minerals handbook.* Moscow: RPC VIMS.

Götze, J., 2009. Chemistry, textures and physical propertie of quartz - geological interpretation and thecnical application. *Mineralogical Magazine,* 73(4), pp. 645-671.

Götze, J. & Plötze, M., 1997. Investigation of trace-element distribution in detrital quartz by Electron Paramagnetic Resonance (EPR). *European Journal of Mineralogy,* 9(3), pp. 529-538.

Götze, J., Plötze, M. & Habermann, D., 2001. Origin, spectral characteristics and practical applications of the cathodoluminescence (CL) of quartz – a review. *Mineralogy and Petrology,* Volume 71, pp. 225-250.

Graetsch, H., 2001. X-ray powder diffraction study on the modulated high temprature forms of SiO2 tridymite between 110 and 220oC. *Physics Chemistry Minerals,* Volume 28, pp. 313-321.

Graetsch, H. A., 2009. Modulated crystal structure of incommensurate low tridymite. *Acta Crystallography B,* 65(5), pp. 543-550.

Graetsch, H. & Topalovic-Dierdorf, I., 1996. 29Si MAS NMR spectrum and superstructure of modulated tridymite L3-To(MX-1). *European Journal of Mineralogy,* 8(1), pp. 103-114.

Guzzo, P. L., Ferreria de souza, L. B., Barros, V. S. M. & Khoury, H. J., 2017. Spectroscopic account of the point defects related to the sensitization of TL peaks beyond 220oC in natural quartz. *Journal of Luminescence,* Volume 188, pp. 118-128.

Haskell, E. H. & Bailiff, I. K., 1985. Diagnostic and corrective procedures for TL analysis using the pre-dose technique. *Nuclear Tracks and Radiation Measurements,* 10(4-6), pp. 503-508.

He, Q. & Shi, C., 2014. Application of Electron Probe Microanalyzer (EPMA) to Depositional Environment Identification of Sedimentary Rock. *Advanced Materials Research,* Volume 881-883, pp. 1795-1798.

Hirose, T. et al., 2005. X-ray, DTA and Raman studies of monoclinic tridymite and its higher temperature orthorombic modification with varying temperature. *Journal of Mineralogical and Petrological Sciences,* Volume 100, pp. 55-69.

Horowitz, Y. S. & Yossian, D., 1995. Computerised Glow Curve Deconvolution: Application to Thermoluminescence Dosimetry. *Radiation Protection Dosimetry,* 60(1), p. 3.

Ikeya, M., 1993. *New applications of electron spin resonance dating, dosimetrry and microscopy.* s.l.:World Scientific Pub. Co. Pte. Ltd..

Joseph Daniel, D., Kim, H. J., Kim, S. & Khan, S., 2017. Thermoluminescence kinetic features of Lithium Iodide (LiI) single crystal grown by vertical Bridgman technique. *Optical Materials,* Volume 70, pp. 120-126.

Kahraman, S., Önal, M., Sarıkaya, Y. & Bozdoğan, İ., 2005. Characterization of silica polymorphs in kaolins by X-ray diffraction before and after phosphoric acid digestion and thermal treatment. *Analytica Chimica Acta,* Volume 552, pp. 201-206.

Kanzaki, M., 2019. Raman spectra of tridymite modifications: MC, MX–1, and PO–10. *Journal of Mineralogical and Petrological Sciences,* 114(4), pp. 214-218.

Kanzaki, M., 2020. Phase transitions of tridymite MC: A low frequency Raman spectroscopic study. *Journal of Mineralogical and Petrological Sciences,* 115(3), pp. 296-301.

Kanzaki, M., 2021. Raman spectroscopic study of pressure–induced phase transitions in tridymite modifications. *Journal of Mineralogical and Petrological Sciences,* 116(5), pp. 245-250.

Kayama, M., Nagaoka, H. & Niihara, T., 2018. Lunar and Martian Silica. *Minerals,* 8(7), p. 267.

Kayama, M., Nishido, H. & Ninagawa, K., 2009. Effect of impurities on cathodoluminescence of tridymite and cristobalite. *Journal of Mineralogical and Petrological Sciences,* 104(6), pp. 401-406.

Keating, K., Knight, R. & Tufano, K. J., 2008. Nuclear magnetic resonance relaxation measurements as a means of monitoring iron mineralization processes. *Geophysical Research Letters,* 35(19).

Kibar, R. ve diğerleri, 2007. Luminescent, optical and color properties of natural rose quartz. *Radiation Measurements,* 42(10), pp. 1610-1617.

Kihara, K., Matsumoto, T. & Imam, M., 1986. High-order thermal-motion tensor analyses of tridymite. *Zeitschrift Für Kristallographie,* 177(1-2), pp. 39-52.

Kitchin, S. J. ve diğerleri, 1996. In situ 29Si MAS NMR studies of structural phase transitions of tridymite. *American Mineralogist,* 81(5-6), pp. 550-560.

Kitis, G., Gomez-Ros, J. & Tyun, J. W. N., 1998. Thermoluminescence glow curve deconvolution functions for first, second and general order of kinetics. *Journal of Physics D: Applied Physics,* Volume 31, pp. 2636-2641.

Kitis, G., Kaldoudi, S. & Charalambous, S., 1990. Thermoluminescence dose response of quartz as a function of irradiation temperature. *Journal of Physics D: Applied Physics,* 23(7), pp. 945-949.

Lee, K. W. & Kim, Y. Y., 2004. Electronic band structure in porous silicon studied by photoluminescence and photoluminescence excitation spectroscopy. *Journal of the Korean Physical Society,* 45(4), pp. 1127-1130.

Lee, S. K. et al., 2017. Quasi-equilibrium melting of quartzite upon extreme friction. *Nature Geoscience,* Volume 10, pp. 436-441.

Lee, S. & Xu, H., 2019. Using powder XRD and pair distribution function to determine anisotropic atomic displacement parameters of orthorhombic tridymite and tetragonal cristobalite. *Acta Crystallographica Section B-Structural Science Crystal Engineering And Materials,* Volume 75, pp. 160-167.

Letertre, M., Giraudeau, P. & Tullio, P., 2021. Nuclear Magnetic Resonance Spectroscopy in Clinical Metabolomics and Personalized Medicine: Current Challenges and Perspectives. *Frontiers in Molecular Biosciences,* Cilt 8.

Lieb, K.-P. & Keinonen, J., 2006. Luminescence of ion-irradiated α-quartz. *Contemporary Physics,* 47(5), pp. 305-331.

Marshall, D. J., 1988. *Cathodoluminescence of geological materials.* Boston: Unwin Hyman Press.

May, C. E. & Partridge, J. A., 1964. Termoluminescent Kinetics of Alpha-Irradiated Alkali Halides. *the Journal of Chemical Physics,* Volume 40, pp. 1401-1409.

McKeever, S. W. S., 1985. *Thermoluminescence of solids.* England: Cambridge University Press.

McKeever, S. W. S., Moscovitch, M. & Townsend, P. D., 1995. *Thermoluminescence dosimetry materials: Properties and USES.* England: Nuclear Technology Publishing.

McQueen, K. G., Pwa, A. & Moort, J. v., 2001. Geochemical and electron paramagnetic characteristics of quartz from a multi-stage vein environment, Cowarra gold deposit, New South Wales. *Journal of Geochemical Exploratşon,* Volume 72, pp. 211-222.

Meier, C. et al., 2007. Silicon nanoparticles: Absorption, emission, and the nature of the electronic bandgap. *Journal of Applied Physics,* Volume 101, p. 103112.

Miller, T. G. & Spoolman, S. E., 2012. *Living in the environmenr.* 17 ed. Brooks/Cole: Cengage Learning.

Monroe, J. & Wicander, R., 2001. *Physical Geology: Exploring the Earth.* 4 ed. Brooks/Cole: Thomson Learning.

Morris, M. F. & McKeever, S. W. S., 1994. Optical bleaching studies of quartz. *Radiation Measurements,* 23(2-3), pp. 323-327.

Morris, R. V. et al., 2016. Silicic volcanism on Mars evidenced by tridymite in high-SiO2 sedimentary rock at Gale crater. *Proseedings of the national academy of sciences of the united states of america,* 113(26), pp. 7071-7076.

Murray, A. S., 1996. Developments in optically stimulated luminescence and photo-transferred thermoluminescence dating of young sediments: Application to a 2000-year sequence of flood deposits. *Geochimica et Cosmochimica Acta,* 60(4), pp. 565-567.

Nedela, V., Tihlaríková, E., Runštuk, J. & Hudec, J., 2018. High-efficiency detector of secondary and backscattered electrons for low-dose imaging in the ESEM. *Ultramicroscopy,* Volume 184, pp. 1-11.

Nie, H. & Byrn, S. R., 2018. Polymorphism and Phase Transition. In: T. Li & A. Mattei, eds. *Pharmaceutical Crystals: Science and Engineering.* s.l.:Wiley, pp. 169-221.

Nilges, M. J., Pan, Y. & Mashkovtsev, R. I., 2009. Radiation-induced defects in quartz. III. Single-crystal EPR, ENDOR and ESEEM study of a peroxy radical. *Physics and Chemistry of Minerals,* Volume 36, pp. 61-73.

O'Hara, P. B., Engelson, C. & Peter, W. S., 2005. Turning on the Light: Lessons from Luminescence. *Journal of Chemical Education,* 82(1), pp. 49-52.

Oniya, E. et al., 2015. Contributions of pre-exposure dose and thermal activation in pre-dose sensitizations of unfired and annealed quartz. *Radiation Physics and Chemistry,* Volume 110, pp. 105-113.

Ostrooumov, M., 2007. A Raman, infrared and XRD analysis of the instability in volcanic opals from Mexico. *Spectrochimica Acta,* Volume 68, pp. 1070-1076.

Pagel, M., Barbin, V., Blance, V. & Ohnensstetter, D., 2000. *Cathodoluminescence in geoscience.* Berlin: Springer-Verlag.

Pandey, A. & Chithambo, M. L., 2018. Thermoluminescence of the persistent-luminescence phosphor, BaAl2O4; A stuffed tridymite. *Radiation Measurements,* Cilt 120, pp. 73-77.

Paralı, L. ve diğerleri, 2011. Luminescence behaviour and Raman characterization of dendritic agate in Dereyalak village (Eskişehir), Turkey. *Journal of Luminescence,* Cilt 131, pp. 2317-2324.

Payre, V. et al., 2022. Tridymite in a lacustrine mudstone in Gale Crater, Mars: Evidence for an explosive silicic eruption during the Hesperian. *Earth and Planetary Science Letters,* Volume 594, p. 117694.

Payré, V. et al., 2022. Tridymite in a lacustrine mudstone in Gale Crater, Mars: Evidence for an explosive silicic eruption during the Hesperian. *Earth and Planetary Science Letters,* Volume 594, p. 117694.

Piao, Y. et al., 2013. Brightening of carbon nanotube photoluminescence through the incorporation of sp3 defects. *Nature Chemistry,* Volume 5, pp. 840-845.

Randall, J. T. & Wilkins, M. H. F., 1945. Phosphorescence and Electron Traps. *Proccedings of the Royal Society,* Volume A184, p. 366.

Roman-Lopez, J. ve diğerleri, 2014. Thermal and electron stimulated luminescence of natural bones, commercial hydroxyapatite and collagen. *Spectrochimica Acta Part A: Molecular and Biomolecular Spectroscopy,* Cilt 120, pp. 610-615.

Sanchez-Munoz, L. et al., 2006. Ultraviolet Luminescence from Defect Complexes in the Twin Boundaries of K-Feldspar. *Chemistry of Materials,* Volume 18, pp. 3336-3342.

Sarasola-Martin, I., Correcher, V. & Garcia-Guinea, J., 2021. Characterization of the red thermoluminescence emission of doped alumina: A case study for Al2O3:C and Al2O3:Cr,Ni. *Journal of Alloys and Compounds,* Volume 886, p. 161262.

Sarasola-Martin, I., Correcher, V. & Garcia-Guinea, J., 2021. Characterization of the red thermoluminescence emission of doped alumina: A case study for Al2O3:C and Al2O3:Cr,Ni. *journal of Alloys and Compounds,* Volume 886, p. 161262.

Shkrob, I., Tadjikov, B. & Trifunac, A., 2000. Magnetic resonance studies on radiation-induced point defect sin mixed oxide glasses. II. Spin centers in alkali silicate glasses. *Journal of Non-Crystalline Solids,* Volume 262, pp. 35-65.

Si, G. et al., 2022. Quartz Tube Enhanced Raman Scattering Spectroscopy. *Frontiers in Physics,* 10(93007).

Smaha, R. ve diğerleri, 2022. Synthesis and Calculations of Wurtzite Al1–xGdxN Heterostructural Alloys. *Chemistry of Materials,* 34(23), pp. 10639-10650.

Swamy, V., Saxena, S. K., Sundman, B. & Zhang, J., 1994. A thermodynamic assessment of silica phase diagram. *Journal of Geophysical Research: Solid Earth,* 99(B6), pp. 11787-11794.

Takada, A., Glaser, K. J., Bell, R. G. & Catlow, R. A., 2018. Molecular dynamics study of tridymite. *IUCrJ.*

Topaksu, M. et al., 2018. UV effect on the cathodo- and thermoluminescence properties of a gem-quality Cr-rich diaspore (α-AlOOH). *Applied Radiation and Isotopes*, Volume 141, pp. 101-106.

Topaksu, M. & Yazıcı, A. N., 2007. The thermoluminescence properties of natural CaF2 after β-irradiation. *Nuclear Instruments and Methods in Physics Research Section B: Beam Interactions with Materials and Atoms,* 264(2), pp. 293-301.

Van Sickle, A. et al., 2013. Temperature Dependent Photoluminescence of Size-Purified Silicon Nanocrystals. *ACS Applied Materials and Interfaces,* 5(10), pp. 4233-4238.

Wasson, J. & Salinas, J., 1980. Nuclear Magnetic Resonance Spectrometry. *Analytical Chemistry,* 52(2), pp. 90-95.

Wenk, H.-R. & Bulakh, A., 2004. *Minerals: their constitution and origin.* Cambridge: Cambridge University Press.

Xiao, Y., Kirkpatrick, R. J. & Kim, Y. J., 1993. Structural phase transitions of tridymite: A 29Si MAS NMR investigation. *American Mineralogist,* Cilt 78, pp. 241-244.

Xiao, Y., Kirkpatrick, R. J. & Kim, Y. J., 1995. Investigations of MX-1 Tridymite by 29Si MAS NMRModulated Structures and Structural Phase Transitions. *Physics and Chemistry of Minerals,* Cilt 22, pp. 30-40.

Yen, A. S. et al., 2020. Formation of Tridymite and Evidence for a Hydrothermal History at Gale Crater, Mars. *Journal of Geophysical Research: Planets,* 126(3).

Yen, A. S. et al., 2021. Formation of Tridymite and Evidence for a Hydrothermal History at Gale Crater, Mars. *Journal of Geophysical Research-Planets,* 126(3), pp. 65-69.

Yuan, D. ve diğerleri, 2023. Synthesis and luminescence properties of Er3+-Yb3+ doped glass ceramics with tridymite structure. *Optical Materials,* Cilt 136, p. 113434.

Zamiatina, D. A., Zamyatin, D. A., Mikhalevskii, G. B. & Chebikin, N. S., 2023. Silica Polymorphs Formation in the Jänisjärvi Impact Structure: Tridymite, Cristobalite, Quartz, Trace Stishovite and Coesite. *Minerals,* 13(5), p. 686.

Zimmerman, J., 1971. The radiation-induced increase of the 100 C thermoluminescence sensitivity of fired quartz. *Journal of Physics C: Solid State Physics,* 4(18), pp. 3265-3276.

CURRICULUM VITAE

Sümeyra BALCI graduated with honors degree of Bachelor of Arts and Sciences in Physics from Fatih University, İstanbul in 2009. She obtained her MSc in the Physics Department from North Carolina State University in the USA in 2013. After completing her MSc, she pursued a PhD in the Physics Department at Cukurova University in 2014. During her PhD, she worked on several research projects supported by the Scientific Research Project Unit of Cukurova University. Additionally, she gained experience as a visiting researcher at CIEMAT in Madrid. Her research areas include radiation energy storage, radiation dosimetry, natural materials, spectroscopy, luminescence, and nanotechnology.